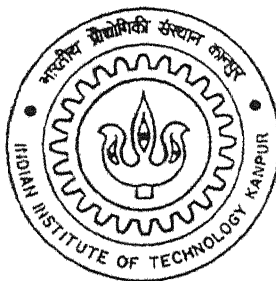


REG NO. - 7210116

# MODELING OF SMART ACTUATORS AND THEIR APPLICATION IN ACTIVE VIBRATION CONTROL

By

Rupal Singhvi



DEPARTMENT OF AEROSPACE ENGINEERING

2004/m  
4 m

Indian Institute of Technology Kanpur

MAY. 2004

MODELING OF SMART ACTUATORS AND THEIR  
APPLICATION IN ACTIVE VIBRATION CONTROL

*A Thesis Submitted*

in Partial Fulfillment of the Requirements

for the Degree of

MASTER OF TECHNOLOGY

by

RUPAL SINGHVI



to the

DEPARTMENT OF AEROSPACE ENGINEERING  
INDIAN INSTITUTE OF TECHNOLOGY KANPUR

May, 2004

28 JUL 2004/AE

गुरुचोत्तम ल. गीनाथ केलकर पुस्तकालय  
भारतीय प्रौद्योगिकी संस्थान कानपुर  
प्राप्ति क्र. A. 148452

TH

AE/2004/M

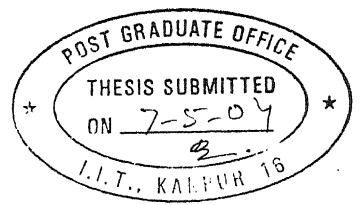
Sig 64 m



A148452

Dedicated to my Parents  
and  
Guide





## CERTIFICATE

It is certified that the work contained in the thesis entitled " Modeling of Smart Actuators and their Application in Active Vibration Control " by Rupal Singhvi has been carried out under my supervision and that this work has not been submitted elsewhere for a degree.

Signature of Supervisor

A handwritten signature in black ink, appearing to read "Venkatesan", written over a horizontal line.

Prof. C. Venkatesan

Department of Aerospace Engineering

IITK

## **ABSTRACT/SYNOPSIS**

**Name of the Student:** Rupal Singhvi

**Roll No:** Y 210116

**Degree for which Submitted:** M.Tech

**Department:** AE

**Thesis Title:** Modeling of Smart Actuators and their Application in  
Active Vibration Control

**Name of Thesis Supervisor:** Dr. C. Venkatesan

**Month and Year of Thesis Submission:** May, 2004

## ABSTRACT

This thesis aims at modeling of the smart actuators and dicusses their application in reduction of vibrations in a highly simplified helicopter model. A smart actuator is a stack of alternate layers of metal and piezoelectric material subjected to externally applied force and/or electric potential. The deflection of such an actuator is dependent on these externally applied forces and voltages. A finite element modeling is carried out in the present study to formulate relation between deflection and the externally applied forces and voltages. When there is a cyclic variation of electric field, piezoelectric materials exhibit polarization-electric field (P-E) and strain-electric field ( $\epsilon$ -E) hysteresis effects. These curves are commonly termed as “ hysteresis loop” (for (P-E) variation) and “ butterfly loop” (for  $\epsilon$ -E variation). The present formulation tries to capture both these effects by following two different approaches, namely the complex stiffness model and the domain switching model. The domain switching model has proved to be a much preferred model as compared to the other. Hysteresis loop is a representation of the energy loss in the system. This energy loss heats up the piezoelectric material. A heat transfer analysis has been carried out to find the variation in temperature distribution within the actuator with change in excitation frequency of the system. The effect of including convection mode of heat dissipation is emphasized through this analysis. A highly simplified helicopter model is considered as a two degree of freedom system representing hub and fuselage connected by a spring-damper-piezo-actuator-sensor system, and a closed loop active vibration control is carried out on this model. In this study, the model consisting of alternate layers of metal and piezoelectric material is used as a sensor as well as an actuator. A comparison between the passive and active vibration isolation is highlighted. It was shown that the model developed minimizes the vibratory loads of both the rotor and fuselage significantly.

## ACKNOWLEDGEMENTS

I express my deep gratitude and indebttness to Dr. C. Venkatesan for his guidance and suggestions throughout my thesis work.

I am surely indebted to Prof. D. Yadav and Asst. Prof. C. S. Upadhyay for making my strong foundation in the areas of vibrations and finite element analysis through course work.

I would like to thank all the persons who helped me directly or indirectly during my thesis work.

# Contents

<b>1</b>	<b>INTRODUCTION</b>	<b>11</b>
1.1	Overview . . . . .	11
1.2	Piezoelectric Materials: History and Processing . . . . .	12
1.2.1	History . . . . .	12
1.2.2	Piezoelectric Ceramic Processing . . . . .	14
1.2.3	Definition . . . . .	16
1.3	Literature survey . . . . .	17
1.3.1	Modeling of Smart Actuator . . . . .	18
1.3.2	Modeling of <i>Hysteresis</i> and <i>Butterfly Loops</i> . . . . .	19
1.3.3	Vibration Control using Smart Actuators . . . . .	20
1.4	Objectives . . . . .	21
1.5	Organization of the Thesis . . . . .	21
<b>2</b>	<b>MODELING OF HYSTERESIS AND BUTTERFLY LOOPS</b>	<b>28</b>
2.1	Constitutive Relations and Material Property . . . . .	29
2.1.1	<i>Constitutive Relations</i> . . . . .	30
2.2	Property Matrix for a poled Piezoelectric Ceramic . . . . .	33
2.3	Assumptions . . . . .	34
2.4	Models for <i>hysteresis</i> and <i>butterfly</i> loops . . . . .	35
2.4.1	Complex Stiffness Model . . . . .	35
2.4.2	Improved Domain Switching Model . . . . .	36
2.5	Results and Discussions . . . . .	39
2.6	Summary . . . . .	40

<b>3</b>	<b>HEAT TRANSFER ANALYSIS OF SMART ACTUATOR</b>	<b>53</b>
3.1	Modes of Heat Transfer . . . . .	53
3.2	Analysis of Heat Transfer within the Actuator . . . . .	55
3.2.1	Mode of Heat dissipation : Conduction and Convection from end faces . . . . .	55
3.2.2	Mode of Heat Dissipation : Conduction and Convection from all faces . . . . .	57
3.3	Results and Discussion . . . . .	60
3.4	Summary . . . . .	61
<b>4</b>	<b>MODELING OF SMART ACTUATOR</b>	<b>68</b>
4.1	Results and Discussion . . . . .	72
4.1.1	<i>Sensing mode</i> . . . . .	72
4.1.2	<i>Actuation mode</i> . . . . .	72
4.2	Summary . . . . .	74
<b>5</b>	<b>VIBRATION CONTROL IN HELICOPTERS USING ACTIVE VI- BRATION CONTROL (CLOSED LOOP POSITION FEEDBACK)</b>	<b>81</b>
5.1	Formulation of relation between horizontal and vertical deflection . . . . .	83
5.2	Formulation of relation between force at sensor/actuator and the force at hub/fuselage . . . . .	84
5.3	Analysis of Vibration Problem . . . . .	85
5.3.1	Sensing Mode . . . . .	85
5.3.2	Actuation mode . . . . .	87
5.4	Results and Discussions . . . . .	89
5.5	Summary . . . . .	90
<b>6</b>	<b>CONCLUDING REMARKS</b>	<b>102</b>
<b>7</b>	<b>SCOPE FOR FUTURE WORK</b>	<b>104</b>

# List of Figures

1.1	Perovskite Structure for PZT . . . . .	23
1.2	Mixed-Oxide-Route of preparing PZT . . . . .	24
1.3	Electro-thermo-elastic interaction (taken from Ref. [4]) . . . . .	25
1.4	Hysteresis loop . . . . .	26
1.5	Butterfly loop . . . . .	27
2.1	Hysteresis curve . . . . .	42
2.2	Change in hysteresis curve with respect to parallel compressive stress . .	42
2.3	Effect of temperature on hysteresis loop . . . . .	43
2.4	Butterfly Loop . . . . .	43
2.5	Dimensional changes of a poled wafer with an applied voltage. The dimensional changes are greatly exaggerated for clarity. . . . .	44
2.6	Switching . . . . .	45
2.7	Poling in a piezo layer . . . . .	46
2.8	Variation of strain, polarization, and electric field ( $E=10^3$ V/m) with frequency (complex stiffness model) . . . . .	47
2.9	Variation of strain, polarization, and electric field with change in magnitude of electric field ( $f=0.01$ Hz) (Complex stiffness model) . . . . .	48
2.10	Variation in strain, polarization, and electric field ( $E=10^3$ V/m) with frequency (domain switching model) . . . . .	49
2.11	Variation in strain, polarization and electric field ( $E=10^6$ V/m) with frequency (domain switching model) . . . . .	50
2.12	Variation in hysteresis and butterfly loops with change in parameter b ( $E=10^6$ V/m; frequency=0.01 Hz ; $a=1$ ) (domain switching model) . . .	51
2.13	Variation in hysteresis and butterfly loops with change in parameter a ( $E=10^6$ V/m; frequency=0.01 Hz ; $b=0.1$ ) (domain switching model) . .	52

3.1	Piezo stack actuator . . . . .	63
3.2	First metallic layer . . . . .	63
3.3	n th metallic layer . . . . .	63
3.4	Metallic layer (between 2 piezo layers) . . . . .	64
3.5	Piezo layer . . . . .	64
3.6	MPM block . . . . .	64
3.7	Energy balance for the metallic layer . . . . .	65
3.8	Energy balance for the piezo layer . . . . .	65
3.9	Plots of temperature profiles across the bar (when Al is the metallic layer)	66
3.10	Plots of temperature profiles across the bar (when Steel is the metallic layer)	67
4.1	Piezo Stack Sensor and Actuator . . . . .	76
4.2	Bar model . . . . .	76
4.3	Finite element model of smart actuator . . . . .	76
4.4	Variation of deflection and induced potential for different external mechanical load (Sensing case metallic layer-aluminium) . . . . .	77
4.5	Variation of deflection along the span for different applied potentials (Actuation case) . . . . .	78
4.6	Plot of potential Vs block force . . . . .	79
4.7	Plot of deflection along the bar when block force is applied . . . . .	79
4.8	Sensing mode (metallic layer-steel) . . . . .	79
4.9	Plot for actuation case (metallic layer-steel) . . . . .	80
4.10	Plot of potential Vs block force . . . . .	80
5.1	Process under Control . . . . .	92
5.2	Open Loop Control System (No Feedback) . . . . .	92
5.3	Closed-Loop Feedback System . . . . .	92
5.4	A Schematic Diagram of Position Feedback Control System . . . . .	93
5.5	Schematic of gear box support structure . . . . .	93
5.6	Piezo stack sensor and actuator . . . . .	94
5.7	Actuator model before and after deformation . . . . .	94
5.8	Rotor hub/isolator/fuselage dynamical model (Ref. [22]) . . . . .	95
5.9	Variation of displacement and acceleration of different systems with frequency (metallic layer-Aluminium) . . . . .	96



5.10	Variation of phase and potential induced with frequency (sensing mode; metallic layer- Aluminium) . . . . .	97
5.11	Variation of displacement with gain (actuation mode; metallic layer-Aluminium)	98
5.12	Frequency response of the actuator at various values of gain (metalli layer- Aluminium) . . . . .	99
5.13	Response of the system (Ref. [22]) . . . . .	100
5.14	Response of the system (Fig. 5.8) when $M_I = 1.3$ kg . . . . .	100
5.15	Variation of phase and potential induced with frequency (sensing mode; metallic layer-steel) . . . . .	100
5.16	Variation of displacement with gain (actuation mode; metallic layer-steel)	101

## NOMENCLATURE

$a, b, a_1, \bar{a}_1, b_1, c_1, c_2$	Constants
$\tilde{a}, \tilde{b}$	Vibration absorber dimensions
$A$	Area
$c$	Stiffness coefficients
$C$	Damping
$C_{ref}$	Critical damping coefficient
$d, e, q, g$	Piezoelectric coupling coefficient
$D$	Electric displacement
$dV$	Elemental volume
$dS$	Elemental surface
$e'$	Piezoelectric stress coefficient
$E$	Electric field
$\tilde{E}$	Young's modulus for metal layer
$f$	Frequency in Hertz
$F$	Force
$F_S, F_A$	Forces at the attachment points (i.e., at hub-gearbox and fuselage-gear box attachment)

$F_{PS}, F_{PA}$	Forces applied on the sensor/actuator
$h$	Heat transfer coefficient
$k$	Thermal conductivity
$k_M, k_P$	Thermal conductivity of metal and piezo material respectively
$K$	Stiffness
$L_M, L_P$	Length of metal and piezo layer respectively
$M_H, M_F$	Mass of gear box/hub and fuselage respectively
$N$	Effective number of aligned dipoles
$P$	Electric polarization
$\bar{P}$	Perimeter
$\tilde{q}$	Heat flux
$\bar{q}$	Heat generated/unit cycle/unit volume
$Q_g$	Heat generated
$Q$	Heat flow
$\delta Q$	Variation in quantity of heat
$s$	Compliance
$T_C$	Curie Temperature
$T_w$	Temperature of the bar
$T_a$	Ambient temperature
$T_1, T_2, \dots$	Temperatures at different layers
$T_P$	Time period
$\Delta T$	Change in temperature

$\bar{T}$	Traction
$u$	Axial deflection
$u_{tip}$	Tip deflection
$V_{\Lambda}$	Actuation voltage
$X_1, X_2$	Deflection of hub and fuselage respectively

### *Greek Symbols*

$\alpha$	Coefficient of expansion
$\epsilon$	Strain
$\eta$	Dielectric susceptibility
$\omega$	Frequency in rad/s
$\omega_{ref}$	Reference frequency
$\phi$	Phase angle
$\psi$	Angle in actuator/sensor mechanism
$\Phi$	Electric potential
$\Phi_{induced}$	Induced potential
$\sigma$	Stress
$\theta$	Temperature difference
$\epsilon_0$	Permittivity of free space
$\epsilon$	Electric permittivity
$\xi$	Damping ratio

# Chapter 1

## INTRODUCTION

### 1.1 Overview

The technological developments in aerospace engineering have created new avenues of research particularly in the areas of structural health monitoring, vibration control, shape and noise control using the concept of smart or intelligent structures. Under external loading conventional structures deform in a passive manner with no control over the final deformed configuration. Whereas in smart structures, the structural deformation is continuously monitored and controlled (using the distributed sensors and actuators) to achieve the desired configuration of the deformed state of the structure. The concept of a smart structure can be well described as *"a system which has intrinsic sensor, actuator and control mechanisms whereby it is capable of sensing a stimulus, responding to it, and reverting to its original state after the stimulus is removed"*. The stimulus may correspond to a stress, strain, light, electric field etc., whereas the response represents the motion or change in optical properties, modulus, surface tension etc. Smart structures can be basically classified as:

1. Passively smart

Structures which have the ability to respond to a stimulus in a useful manner, without assistance of electronic controls or feedback systems

2. Actively smart

Structures which utilize a feedback loop to accelerate the recognition and response process

### 3. Very smart or intelligent

Structures which utilize the nonlinear properties of the sensor, actuator, memory and/or feedback systems to tune the response behavior.

A smart structure comprises of three main components and they are:-

#### 1. Sensor

To monitor environmental changes and generate signals proportional to the changing measurand. Sensor applications are based on the *direct piezoelectric effect* (strain-induced electric field).

#### 2. Actuator

The actuators are used to change the properties of smart structure in order to achieve the desired response. The actuator applications are based on the *indirect piezoelectric effect* (applied external voltage-induced strain).

#### 3. Control systems

The control system continually monitors the sensors signal, processes the information in order to determine the required action .

The distributed sensing and actuation can be implemented by embedding piezoelectric material in the structure.

## 1.2 Piezoelectric Materials: History and Processing

Piezoelectricity stems from the Greek word *piezo* for pressure. It follows that a piezoelectric material develops a potential across its boundaries when subjected to a mechanical stress (or pressure), and vice versa, when an electric field is applied to the material, a mechanical deformation ensues. Piezoelectric materials therefore fall in the class of smart materials. Ferro-electricity is a subgroup of piezoelectricity, where a spontaneous polarization exists that can be reoriented by application of an alternating electric field.

### 1.2.1 History

Piezoelectricity is a property possessed by a group of materials, discovered in 1880 by Pierre and Jacques Curie during their study of the effects of pressure on the generation

of electrical charge by crystals such as Quartz, Tourmaline, and Rochelle salt. In 1881, the term "piezoelectricity" was first suggested by W.Hankel, and the converse effect was deduced by Lipmann from thermodynamics principles. In the next three decades, collaborations within the European scientific community established the field of piezoelectricity; and by 1910, Voigt's "Lerbuch der Kristallphysic" was published and became a standard reference work detailing the complex electro-thermo-elastic relationship in piezoelectric crystals. However, the complexity of the science of piezoelectricity made it difficult for it to mature to an application until a few years later. Langevin et al. developed a piezoelectric ultrasonic transducer during World War I. Their success opened up opportunities for piezoelectric materials in underwater applications such as ultrasonic transducers, microphones, accelerometers, etc.. In 1935, Busch and Scherrer discovered piezoelectricity in potassium dihydrogen phosphate (KDP). The KDP family was the first major family of piezoelectrics and ferro-electrics to be discovered.

During World War II, research in piezoelectric materials expanded to the U.S., the Soviet Union and Japan. Up until then, limited performance by these materials inhibited commercialization but that changed when a major breakthrough came with the discovery of barium titanate and lead zirconate titanate (PZT) in the 1940s and 1950s respectively. These families of materials exhibited very high dielectric and piezoelectric properties. Furthermore, they offered the possibility of tailoring their behavior to specific responses and applications by the use of dopant's. To date, PZT is one of the most widely used piezoelectric materials. It is noted that most commercially available ceramics (such as barium titanate and PZT) are based on the perovskite structure (Fig. 1.1). The perovskite structure ( $ABO_3$ ) is the simplest arrangement where the corner-sharing oxygen octahedra are linked together in a regular cubic array with smaller cations (Ti, Zr, Sn, Nb etc.) occupying the central octahedral B-site, and larger cations (Pb, Ba, Sr, Ca, Na etc.) filling the interstices between octahedra in the larger A-site. Compounds such as  $BaTiO_3$ ,  $PbTiO_3$ ,  $PbZrO_3$ ,  $NaNbO_3$  and  $KNbO_3$  have been studied at length and their high temperature ferroelectric and anti ferroelectric phases have been extensively exploited. This structure also allows for multiple substitutions on the A-site and B-site resulting in a number of useful though more complex compounds such as  $(Ba,Sr)TiO_3$ ,  $(Pb,Sr)(Zr,Ti)O_3$ ,  $Pb(Fe,Ta)O_3$ ,  $(KBi)TiO_3$  etc.

Starting around 1965, several Japanese companies focused on developing new processes and applications, and opening new commercial markets for piezoelectric devices.

The success of the Japanese effort attracted other nations, and today the needs and uses extend from medical applications to the communications field to military applications and the automotive field.

A review of the early history of piezoelectricity is found in the work of W.G.Cady (Ref. [1]).

### 1.2.2 Piezoelectric Ceramic Processing

The fabrication of most bulk piezoelectric ceramic starts with powder preparation. The powder is then pressed to the required shapes and sizes, and the grain shapes are in turn processed to mechanically strong and dense ceramics. The more important processes that influence the product characteristics and properties are powder preparation, powder calcining and sintering. The next steps are machining, electroding and poling: application of a DC field to orient the dipoles and induce piezoelectricity.

The most common powder preparation is the mixed oxide route. In this process, powder is prepared from the appropriate stoichiometric mixture of the constituents oxides. In the case of lead zirconate titanate (PZT): lead oxide, titanium oxide, and zirconium oxide are the main compounds. Depending on application, various dopant's are used to tailor the properties of interest. PZT ceramics are rarely utilized without the addition of dopant's to modify some of their properties. A-site additives tend to lower the dissipation factor, which affects heat generation, but also lowers the piezoelectric coefficients; for this reason they are mostly used in ultrasonics and other high frequency applications. B-site dopants increase the piezoelectric coefficients but also increase the dielectric constant and loss. They are utilized as actuators in vibration and noise control, benders, optical positioning application etc. Figure 1.2 shows a flowchart of the mixed oxide route for making PZT ceramics. Mixing of the powders can be done by dry-ball or wet-ball milling, both methods having advantages and disadvantages: wet ball-milling is faster than dry-ball milling; however, the disadvantage is the added step of liquid removal. The most common method for making PZT ceramics is through wet-ball milling; ethanol and stabilized zirconia media are added for a wet milling process. A vibratory mill may be used rather than a conventional ball mill; it was shown by Herner (Ref. [2]) that this process reduces the risk of contamination by the balls and the jar. Zirconia media are used to further reduce the contamination risks. The calcination step is a very crucial step in the processing of PZT ceramics; it is important that the crystallization be complete



and that the perovskite phase forms during this step. The goals are to remove any organics, water or other volatiles left after mixing; to react the oxides to form the desired phase composition before the ceramic is processed to useful devices; and to reduce volume shrinkage and allow for better homogeneity during and after sintering.

After calcining, a binder is added to the powder, then the mixture is shaped usually by dry-pressing in a die for simple shapes, or extrusion, or casting for more complicated bodies. Next, the shapes are sintered: placed in an oven for binder burn-out and densification.

The major problem in the sintering of the PZT ceramic is the volatility of PbO at about 800° C. To minimize this problem, the PZT samples are sintered in the presence of a lead source, such as  $\text{PbZrO}_3$ , and placed in closed crucibles. The saturation of the sintering atmosphere with PbO minimizes lead loss from the PZT bodies. Sintering can now be carried out at temperatures varying between 1200-1300° C. Despite precautions, there is usually a resulting loss of 2%-3% of the initial lead content.

After cutting and machining into desired shapes, electrodes are applied and a strong DC field is used to orient the domains in the polycrystalline ceramic. DC poling can be done at room temperature or at higher temperatures depending on the material and the composition. The poling process only partially aligns the dipoles in a polycrystalline ceramic, and the resulting polarization is lower than that for single crystals.

This processing technique present many uncertainties and the presence of a wide number of other fabrication techniques is an indication that there is a great need for the production of reliable PZT ceramics with optimum properties and micro structure. One problem often encountered is the deviation from stoichiometry. This problem is often due to impurities present in the raw materials as well as the lead loss during the sintering process, which invariably results in substantial alterations of the PZT properties. As a result, the elastic properties can vary as much as 5%, the piezoelectric properties 10% and the dielectric properties 20% within the same batch (Ref. [2]). Also, the piezoelectric and dielectric properties generally suffer if there is any lack of homogeneity due to poor mixing. It is important then that the constituent oxides be intimately mixed. In the method described above, however, the constituents are solid solutions and it has been shown that an intimate mixing of solid solutions is difficult if not impossible. More information on the preparation of piezoelectric ceramics can be found in Jaffe, Cook and Jaffe (Ref. [3]).

### 1.2.3 Definition

Piezoelectricity is a physical phenomenon which is related to the microscopic structure of the solid. Some ceramic materials become electrically polarized when they are strained; this phenomenon is referred to as *direct piezoelectric effect*. The direct piezoelectric effect is always accompanied by the *converse piezoelectric effect* where a solid becomes strained when placed in an electric field. The microscopic origin of the piezoelectric effect is the displacement of ionic charges within a crystal structure. In the absence of external strain, the charge distribution within the crystal is symmetric and the net electric dipole moment is zero. However when an external stress is applied, the charges are displaced and the charge distribution is no longer symmetric. A net polarization develops and results in an internal electric field. A material can only be piezoelectric if the unit cell has no center of inversion.

The interaction among the three fundamental constituents namely mechanical, electrical and thermal loading on piezoelectric materials is shown in Fig. 1.3. The various interactions that basically exist can be classified as thermo-elasticity, piezoelectricity and pyroelectricity (Ref. [1] and [4]). An electric field  $E$  causes piezoelectric stress  $\sigma = e'E$ , where  $e'$  is the appropriate piezoelectric stress coefficient. Similarly a strain  $\epsilon$  causes the electric polarization  $P = e\epsilon$ . In a similar manner, the pyroelectric constant  $p$  relates a change in temperature  $\Delta T$  with polarization  $P$ ; the arrow from  $E$  to  $\delta Q$  indicates the electro-caloric effect (i.e., the variation in the quantity of heat  $Q$  on application of an electric field  $E$ ), which is usually expressed as a relation between the change in temperature  $\Delta T$  and  $E$ . The thermal coefficient of expansion  $\alpha$  relates  $\Delta T$  with  $\epsilon$ ; the arrow from  $\sigma$  to  $\delta Q$  with a coefficient  $b$  relating them indicates the thermoclastic effect. Stress  $\sigma$  and strain  $\epsilon$  are related by the equation of the form  $\epsilon = s\sigma$ . In an analogous manner, polarization  $P$  and electric field  $E$  are related by dielectric susceptibility  $\eta$ ; and quantity of heat  $\delta Q$  is related to change in temperature  $\Delta T$  through specific heat  $c$ . The arrows indicate the directions in which the various effects usually take place. The additional arrow between  $P$  and  $E$  indicates that an electric field may exist by virtue of polarization in the material.

Each of the nine straight lines in Fig. 1.3 usually represent the primary or "*true effect*". However, in every case there is at least one other path over which the process can take place, unless the coefficient are zero for that particular process for the material (or crystal) under consideration. The roundabout effects are usually denoted as "*false or secondary*".

*effects*". An example is the false pyroelectric effect due to piezoelectric action, which may be several times greater than the direct effect itself. The primary pyroelectric effect is indicated by the path  $\Delta T \rightarrow P$ , while the secondary effect follows the path  $\Delta T \rightarrow \epsilon \rightarrow P$ . The reason for this complication is due to the fact that every pyroelectric crystal is also piezoelectric. Therefore a change in temperature of an unconstrained crystal causes a deformation and this in turn produces the secondary polarization of piezoelectric origin superposed on the primary pyroelectric polarization. Therefore it is evident that primary pyroelectricity would be observed only in a completely clamped crystal.

In a similar manner when an elastic compliance coefficient  $s$  is measured by observations of  $\sigma$  and  $\epsilon$  a piezoelectric polarization  $P$  is produced, which if the crystal is not short circuited gives rise to an electric field  $E$ , which in turn modifies the value of stress  $\sigma$ . In addition, through thermoelastic effect there is a change in the temperature which affects the value of strain  $\epsilon$ . Hence it becomes important to specify the conditions under which the material coefficients are measured and they must be properly incorporated in the analysis of smart structures, having a base structure with embedded piezo layers. Under cyclic variation of electric field, piezoelectric material exhibits a hysteretic (polarization-electric field (P-E)) effect leading to energy loss. This energy goes in for developing heat i.e., hysteresis loss corresponds to heat developed/dissipated. As a result, the actuator heats up tremendously and this sometimes becomes the cause for the damage of the actuator. In addition to the P-E hysteresis the polarization switching leads to a strain-electric field hysteresis termed as "butterfly loop". Both these loops are shown in Figs. 1.4, and 1.5.

It is due to the direct and converse effects that the piezoelectric material embedded smart structures find great use as both sensors and actuators. Smart actuators having piezo stack have been developed for generating active control forces in active vibration isolation systems.

### 1.3 Literature survey

The literature survey has been carried out in three distinct directions of research, namely:

- One dealing with the modeling of the smart actuator.
- Formulation of a model which would generate *hysteresis and butterfly loops*.

- Vibration control in helicopters using smart actuator.

### 1.3.1 Modeling of Smart Actuator

The authors of Ref. [2] have provided a detailed review of piezoelectric ceramics analysis and characterization. The focus is on polycrystalline ceramics. To thoroughly grasp the behavior of a piezoelectric polycrystalline ceramic, a basic understanding of the ceramic itself should not be overlooked. This review presents a brief introduction of the history of piezoelectricity and a discussion on processing of the ceramic and development of the constitutive relations that define the behavior of a piezoelectric material. It also covers the most common methods of measuring the parameters of interest in piezoelectricity.

In Ref. [5] Venkatesan and Upadhyay presented a comprehensive description of the physical interactions in a piezoelectric material used in development of smart structures. The governing electro-thermo-elastic equations for the analysis of smart structures have been developed from the fundamental laws of conservation and thermodynamic principles. Further in Refs. [4], [6] and [7], using a finite element model, the deformation of a smart beam has been analyzed for actuation and sensing cases, by solving the coupled electro-elastic problem. The key difference between sensing and actuation has been brought out by solving for the electric potential and the displacement variables in the piezo materials. It is also brought out that the interaction between polarization and electric field in the piezo continuum leads to non-linear distributed body force and non-symmetric stress tensor. These non-linear effects are found to have significant influence on the deformation of a smart beam under actuation.

Sirohi and Chopra (Ref. [8]) investigated the behavior of piezoceramic actuators under different types of excitations and mechanical loading. The research focuses on the application of these actuators to the development of smart rotor systems. The free strain response of the actuators under DC excitation is investigated experimentally along with the associated drift of the strain over time. Effect of tensile stresses on the DC response is investigated. Strain response to an AC excitation is also investigated for a free actuator and for a pair of actuators surface bonded to a host structure. The phase lag of the strain response and non-linear hysteretic effects have been observed and the power consumption has been validated by the impedance method. Additionally, depoling of the actuators is discussed, along with the feasibility of recovering performance by repoling in the event of accidental depoling.

### 1.3.2 Modeling of *Hysteresis* and *Butterfly* Loops

A phenomenological constitutive law for ferroelectric switching due to multi-axial mechanical and electrical loading of a polycrystalline material was developed by Robert and Chad (Ref. [9]). The constitutive law successfully reproduces hysteresis and butterfly loops for ferroelectric ceramics. The paper provides a relatively simple law that can simulate the nonlinear switching behavior of polycrystalline ferroelectrics subject to multi-axial stress and an arbitrary electric field.

In Refs. [10] and [11] an attempt is made to develop a mathematical model for the hysteresis curve by employing a hysteretic restoring force model (Refs. [12] and [13]) to capture the effects due to change in temperature, pressure and electric field. The parameters representing the model have been identified and their influences on the nature of hysteresis curve have been analyzed. It has been seen that there are strong interactions among temperature, pressure and amplitude of electric field. A small change in one factor can alter the behavior due to other effects.

Chen and Montgomery (Ref. [14]) present a macroscopic theory leading to the hysteresis and butterfly loop in ferroelectricity. This theory is based on the notion that as domains switch under the action of an external electric field the number of dipoles aligned in the direction of the field also alters and it obeys a rate law which depends non-linearly on the field. In addition, the paper specifies the simplest constitutive relations of the stress and electric displacement which together with the rate law are sufficient to yield the hysteresis loop and the butterfly loop.

A phenomenological formulation of polarization reversal of piezoelectric materials is proposed based on the dynamics of domain switching in Ref. [15]. This formulation provides a method to describe the hysteresis in piezoelectricity as well as in electro-magnetics. It is shown that a good approach to describe the nonlinear induced strain field behavior and electromechanical hysteresis in piezoelectricity is by combining the macroscopic phenomenological aspects with the microscopic material properties. A one dimensional thermo-electro-mechanical constitutive model for piezo ceramics which undergo polarization reversal is presented using a continuum mechanics approach. This model is based on thermodynamic principles and reflects the essence of the electromechanical behavior of piezoceramics simply and reasonably well.

A model that bridges micro- and macroscopic concepts was developed by Narayan, Lu and Hanagud (Ref. [16]) to describe the nonlinear material and thermodynamic behav-

iors of piezoelectric ceramics. The domain evolutions was described by the evolution of the associated internal variables, which are the parameters of the assumed domain orientation distribution. The bulk material behavior was obtained by simply using the domain distribution to collect all the domain behaviors. Using this model, the thermodynamic parameters were evaluated.

### 1.3.3 Vibration Control using Smart Actuators

The problem of the formulation and solution of an active vibration control scheme for helicopters, based on the concept of active control of structural response is addressed in Ref. [17]. First, using a mathematical procedure employing the Fischer information matrix, optimum sensor locations have been identified in a three-dimensional model of a flexible fuselage structure. Then, using the measurements from these optimal sensor locations, a multi-input/multi-output control problem has been formulated and solved to obtain the active control forces required for vibration minimization in the helicopter fuselage. It is observed that sensor locations have a significant influence on the level of vibration reduction in a fuselage structure. A review on the sensor placement in distributed parameter systems and their influence on vibration reduction can be found in Refs. [18]-[21] .

The equations of motion for the coupled rotor/isolator/fuselage dynamical system are formulated in Ref. [22] for the prediction of vibration in helicopters during forward flight. Using a combined Floquet theory/frequency-response technique, the equations were solved to predict the vibratory loads at the various locations of the helicopter. In addition, the influence of the isolator on the hub and blade loads was established. It was shown that the inclusion of an isolator between the hub and the fuselage reduces the fuselage vibratory loads and increases the hub loads significantly.

The problem of vibration reduction in helicopter fuselages using the active control of structural response (ACSR) is addressed in Ref. [23]. First a balance-realization-based order reduction is employed to reduce the size of the problem. It was observed that contrary to open-loop control, the technique of closed-loop control reduces the vibratory levels both in the fuselage and the gearbox.

## 1.4 Objectives

The main objectives of the present study are :

1. *Modeling of hysteresis and butterfly loops* : To formulate a model that would generate polarization-electric field (*hysteresis*) and strain-electric field (*butterfly*) loops
2. *Modeling of smart actuator* : To analyze the deformation and induced potential developed in a smart actuator using a finite element model, by solving the coupled electro-elastic problem of a stack actuator.
3. *Heat transfer analysis of a smart bar* : To study the heat transfer in a smart actuator taking into consideration that heat dissipation to the surroundings happens through the phenomena of conduction and convection. The importance of including convection is highlighted.
4. *Vibration control using a active vibration isolation concept employing position feedback control.*

## 1.5 Organization of the Thesis

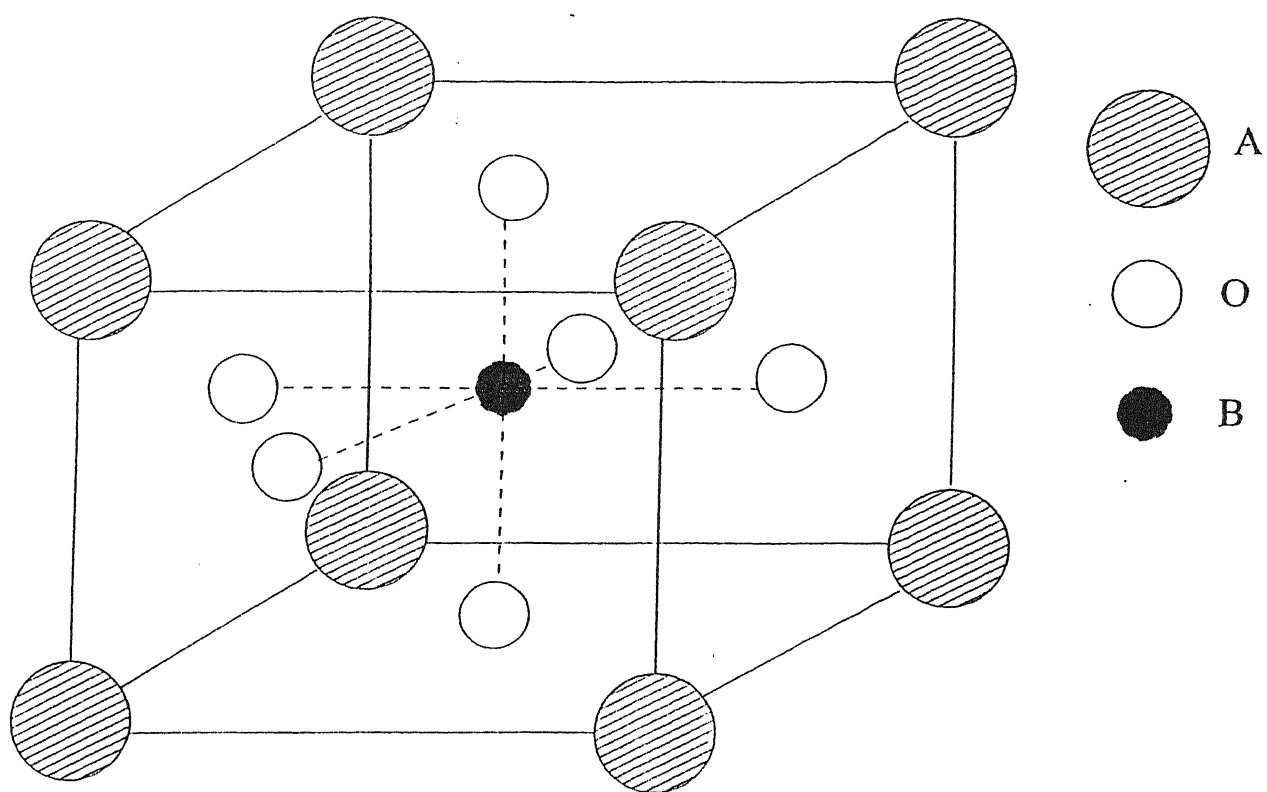
In Chapter 2, the constitutive equations required to generate the hysteresis and butterfly loops are generated. Two approaches are used namely: linear complex stiffness approach and the other is the improved model which incorporates the concept of *domain switching*. The relative difference in the two models at various operating frequencies and electric fields is analyzed.

Chapter 3 introduces the study of heat transfer in the smart actuator. The basic heat transfer phenomena i.e., conduction and convection are considered while formulating the equations. The importance of convection heat transfer in the formulation is brought out. The study is carried out at various frequencies and electric fields to find the temperature distribution in smart actuators, which is useful for practical real-life applications.

Chapter 4 deals with the description and formulation of a layer-by-layer finite element analysis for smart stack actuators. The problems of sensing and actuation have been addressed here. The distribution of induced potential in the piezo material due to externally applied potential and due to mechanical straining has been studied.

In Chapter 5 the problem of vibration control is addressed. A highly simplified model of a helicopter is considered as a two degree of freedom system representing hub and fuselage connected by a spring-damper-piezo-actuator-sensor system. It is shown that the inclusion of active vibration isolator between the hub and the fuselage reduces not only the fuselage vibratory loads as well as the the hub loads significantly, contrary to the passive isolation system.





A - Lead ; O - Oxygen ; B - Titanium  
Zirconium

Figure 1.1: Perovskite Structure for PZT

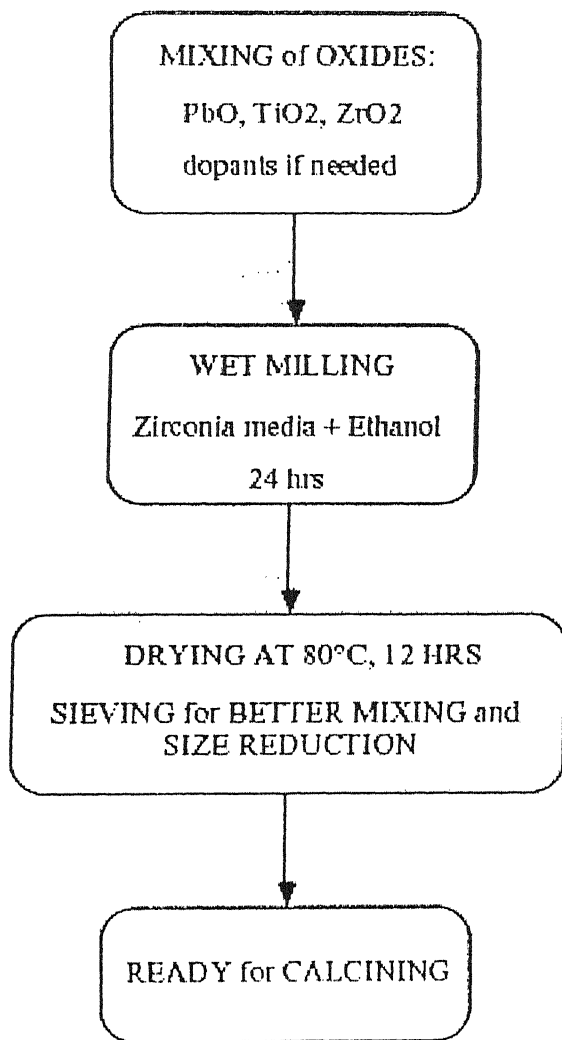


Figure 1.2: Mixed-Oxide-Route of preparing PZT

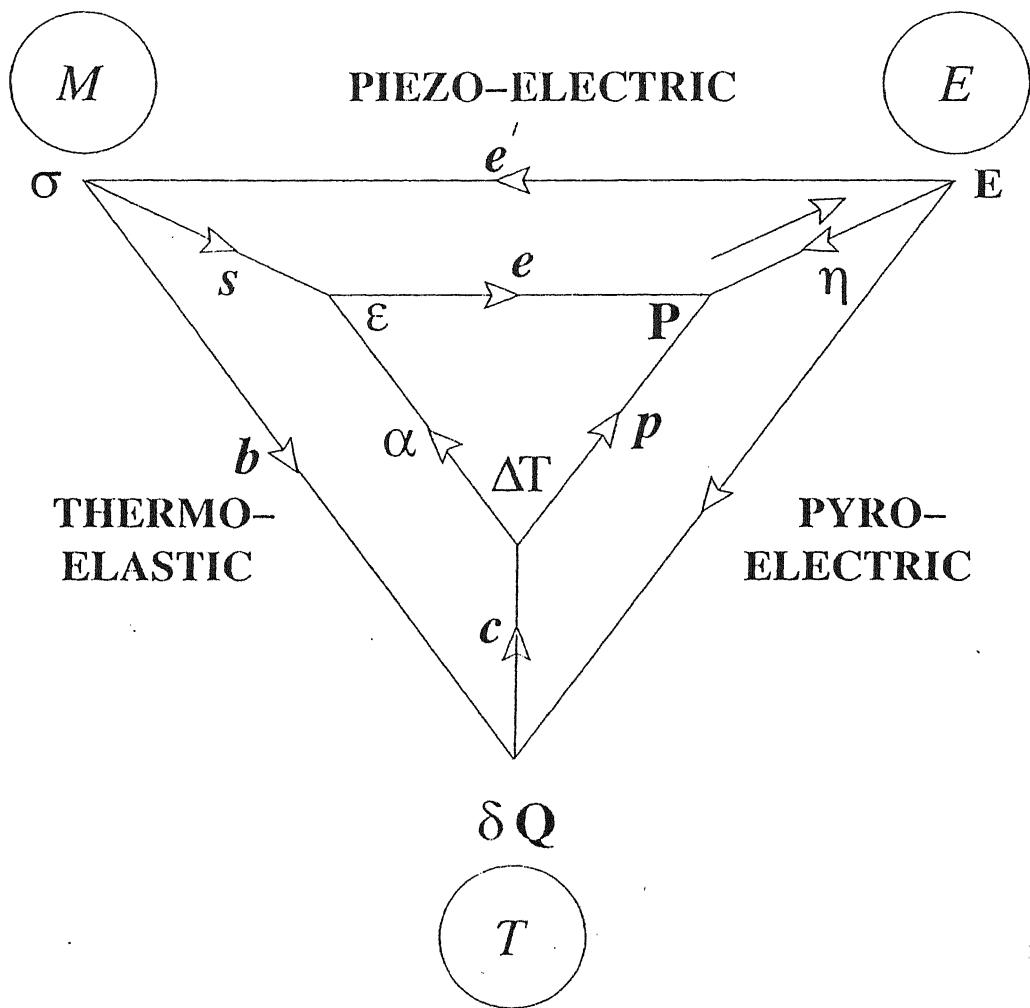
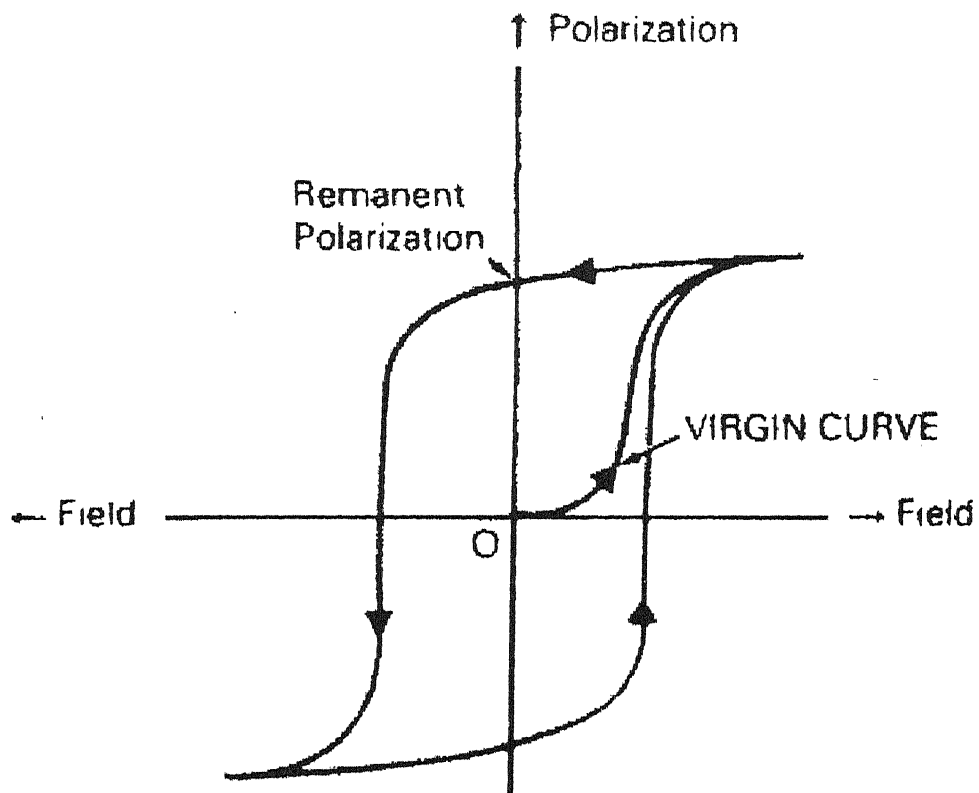


Figure 1.3: Electro-thermo-elastic interaction (taken from Ref. [4])



Typical  $P$ - $E$  hysteresis loop for a normal ferroelectric

Figure 1.4: Hysteresis loop

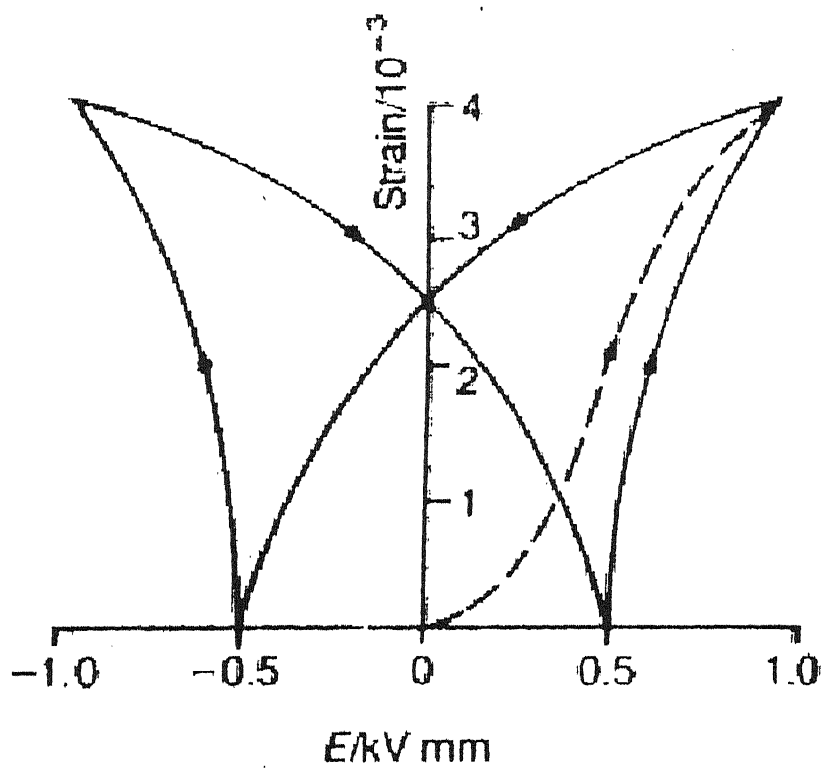


Figure 1.5: Butterfly loop

## Chapter 2

# MODELING OF HYSTERESIS AND BUTTERFLY LOOPS

A ferroelectric material possesses spontaneous polarization that can be reversed in direction by application of a realizable electric field. This phenomenon is observed over some temperature range. Most ferroelectric materials have a *Curie temperature*,  $T_C$  below which they are polar and above which they are not. Applying a large alternating electric field causes the polarization to reverse, and this gives rise to the ferroelectric *hysteresis loop*, relating the polarization  $P$  to the electric field  $E$ . The relation between the electric displacement  $D$ , polarization  $P$  and electric field is given by the linear equation

$$D_i = P_i + \epsilon_0 \cdot E_i \quad (2.1)$$

where  $\epsilon_0$  is the permittivity of free space ( $=8.85 \cdot 10^{-12}$  C/V-m). A typical hysteresis loop is illustrated in Fig. 2.1. Let us begin with a crystal with randomly oriented dipoles so that there is no net polarization (i.e., average polarization is zero). When an electric field is applied, the dipoles begin to line up with the field points 1-2. As the field is increased, eventually all the dipoles are aligned in the direction of the field and maximum polarization (also denoted as saturation polarization)  $P_{\text{sat}}$  is obtained (point 2). When the electric field is removed, a remanent polarization denoted by point 3 remains due to interaction between dipoles and therefore the material is permanently polarized. When the direction of electric field is changed, the dipoles also change their direction. The coercive field  $E_c$  (point 4) removes the polarization and randomizes the dipole directions. If the field is increased further, saturation occurs with opposite polarization. As the field

continues to alternate, a hysteresis loop is formed and the area of the loop is related to the energy required to switch the polarization from one direction to the other.

The hysteretic behavior of the piezoceramics is a complex issue, sensitive to applied stresses and temperature. Fig. 2.2 exhibits the influence of an applied stress field on the hysteresis loop (Refs. [10] and [11]). It is shown that a parallel compressive stress decreases the spontaneous and remanent polarization as well as the coercive field, but a compressive stress perpendicular to the field only slightly increases the coercive field. The temperature is also an important factor which influences the hysteresis loop. Figure 2.3 shows that the remanent polarization  $P_r$  and coercive field  $E_c$  are functions of temperature. It is shown that the whole hysteresis loop shrinks with increasing temperature. It is thus revealed that the hysteresis loop is a manifestation of the coupled electro-mechanical behavior of piezoceramics.

In addition to the P-E loop, polarization switching leads to strain-electric field hysteresis. A typical strain-field response curve is shown in Fig. 2.4. The shape resembles that of a butterfly, and it is often referred to as the “*butterfly loop*”. As the field is increased, the strain is no longer linear with the field as domains start switching (Ref. [14]).

The maximum positive field is limited by the breakdown of the dielectric, which in this case is the ceramic itself, and the value of this *limiting field* is  $10 \text{ kV/cm}$ , whereas the maximum negative field is limited by the piezoceramic *depoling*. When exposed to a high electric field opposite to the poling direction, the piezoceramic loses most of its piezoelectric capability, accompanied by large dielectric losses and poor efficiency. This is known as *depoling* of the piezoceramic and is accompanied by a permanent change in dimensions of the specimen. This is probably due to large scale domain switching in the material. The DC *depoling field* of PZT-5H is approximately  $5.5 \text{ kV/cm}$  (Ref. [8]).

## 2.1 Constitutive Relations and Material Property

An understanding of piezoelectricity begins with the structure of the material. To better explain it, let us consider a single crystallite from a polycrystalline ceramic. This crystal is made up of negatively and positively charged atoms occupying specific positions in a repeating unit or cell. The specific symmetry of the unit cell determines the possibility of piezoelectricity in the crystal. All crystals can be divided into 32 classes or point

groups (from 7 basic crystal systems: triclinic, monoclinic, orthorhombic, tetragonal, rhombohedral, hexagonal and cubic). Of the 32 classes, 21 do not possess a center of symmetry, and 20 are piezoelectric (one class, although lacking a center of symmetry, is not piezoelectric because of the combination of other symmetry elements). The lack of center of symmetry means that a net movement of the positive and negative ions with respect to each other as a result of stress produces an electric dipole. The ceramic, being composed of the random orientation of these piezoelectric crystallites, is inactive, i.e., the effects from the individual crystals cancel each other and no discernible piezoelectricity is present. A volume of the material in which the polar moments of the unit cell are all oriented in the same direction is called a domain. The unpoled ceramic consists of many randomly oriented domains and thus has no net polarization. Application of a high electric field has the effect of aligning most of the domains in such a way that the polar axes of the unit cells are oriented as closely parallel to the applied field as allowed by the crystal structure. This process is called *poling* and it imparts a permanent net polarization to the ceramic. Since the polar axis of the unit cell is longer than the other two axes, the reorientation of the domains also creates a permanent mechanical distortion Fig. 2.5 . The polar axes can be reoriented in certain specific directions governed by the crystal symmetry in the presence of a high electric field or mechanical stress. This process is called *switching*. In the case of tetragonal PZTs , either 90 degree or 180 degree switching can occur (Fig. 2.6). The 90 degree switching is always accompanied by mechanical distortion due to the longer length of the unit cell along the polar axes, while the 180 degree switching can occur without any distortion. It is also known that an electric field can cause both 90 degree and 180 degree domain switching but a mechanical stress can only cause 90 degree switching. Consequently, a mechanical stress can depole a piezoelectric ceramic but cannot repole it. The poled ceramics exhibits the *direct and converse piezoelectric effects*.

### 2.1.1 Constitutive Relations

For mechanical problems a constitutive equation describes how a material strains when it is stressed, or vice-versa. Constitutive equations exist also for electrical problems; they describe how charge moves in a (dielectric) material when it is subjected to a voltage, or vice-versa. Engineers are generally familiar with the most common mechanical constitutive equations that applies for everyday metals and plastics. This equation is known as



Hooke's law and is written as

$$\epsilon = s \cdot \sigma$$

In words, this equation states: Strain = Compliance \* Stress.

However, since piezoelectric materials are concerned with electrical properties too, we must also consider the constitutive equation for common dielectrics:

$$D = \epsilon \cdot E$$

In words, this equation states: Charge density = Permittivity \* Electric field.

### *Coupled equation:*

Piezoelectric materials combine these two seemingly dissimilar constitutive equations into one coupled equation, written as

$$\epsilon = s_E \cdot \sigma + d^t \cdot E$$

$$D = d \cdot \sigma + \epsilon_\sigma \cdot E$$

The matrix  $d$  contains the piezoelectric coefficients for the material, and it appears twice in the constitutive equation (the superscript t stands for matrix transpose).

In order to describe or model piezoelectric materials, one must have knowledge about the materials mechanical properties (compliance or stiffness), its electrical properties (permittivity), and its piezoelectric coupling properties. The four state variables ( $\epsilon$ ,  $\sigma$ ,  $D$ , and  $E$ ) can be rearranged to give an additional three forms for a piezoelectric constitutive equation. Instead of the coupling matrix  $d$ , they contain the coupling matrices  $e$ ,  $g$ , or  $q$ . It is possible to transform piezo constitutive data in one form to another form. The four possible forms for piezoelectric constitutive equations are shown below. The names of each of the form is arbitrary; they were taken from the two dependent variables on the left-hand-side of each equation. Note that the voltage and electric field are related as,

$$E_i = -\frac{\partial \Phi}{\partial x_i}$$

Strain-Charge form:

$$\epsilon = s_E \cdot \sigma + d^t \cdot E$$

$$D = d \cdot \sigma + \epsilon_\sigma \cdot E$$

Stress-Charge form:

$$\sigma = c_E \cdot \epsilon - e^t \cdot E$$

$$D = e \cdot \epsilon + \epsilon_\epsilon \cdot E$$

Strain-Voltage form:

$$\epsilon = s_D \cdot \sigma + g^t \cdot D$$

$$E = -g \cdot \sigma + \epsilon_\sigma^{-1} \cdot D$$

Stress-Voltage form:

$$\sigma = c_D \cdot \epsilon - q^t \cdot D$$

$$E = -q \cdot \epsilon + \epsilon_\epsilon^{-1} \cdot D$$

Matrix transformations for converting piezoelectric constitutive data from one form into another are shown below.

Strain charge to Stress charge

$$c_E = s_E^{-1}$$

$$e = d \cdot s_E^{-1}$$

$$\epsilon_\epsilon = \epsilon_\sigma - d \cdot s_E^{-1} \cdot d^t$$

Strain charge to Strain Voltage

$$s_D = s_E - d^t \cdot \epsilon_\sigma^{-1} \cdot d$$

$$g = \epsilon_\sigma^{-1} \cdot d$$

Stress charge to Stress Voltage

$$c_D = c_E + e^t \cdot \epsilon_\epsilon^{-1} \cdot e$$

$$q = \epsilon_\epsilon^{-1} \cdot e$$

Strain Voltage to Stress Voltage

$$c_D = s_D^{-1}$$

$$q = g \cdot s_D^{-1}$$

$$\epsilon_\epsilon^{-1} = \epsilon_\sigma^{-1} + g \cdot s_D^{-1} \cdot g^t$$

The subscripts in piezoelectric constitutive equations have very important meanings. They describe the conditions under which the material property data was measured. For e.g., the subscript E on the compliance matrix  $s_E$  means that the compliance data was measured under at least a constant, and preferably a zero, electric field. Likewise, the subscript  $\sigma$  on the permittivity matrix  $\epsilon_\sigma$  means that the permittivity data was measured under at least a constant, and preferably a zero, stress field.

A description of all matrix variables used in the piezoelectric constitutive equations is given as follows:

Symbol	Object type	Size	Units	Meaning
$\sigma$	vector	6*1	N/m <sup>2</sup>	Stress components (e.g. $\sigma_1$ )
$\epsilon$	vector	6*1	m/m	Strain components (e.g. $\epsilon_1$ )
$E$	vector	3*1	N/C	Electric field components
$D$	vector	3*1	C/m <sup>2</sup>	Electric charge density displacement components
$s$	matrix	6*6	m <sup>2</sup> /N	Compliance coefficients
$c$	matrix	6*6	N/m <sup>2</sup>	Stiffness coefficients
$\epsilon$	matrix	3*3	F/m	Electric permittivity
$d$	matrix	3*6	C/N	Piezoelectric coupling coefficient for strain charge form
$e$	matrix	3*6	C/m <sup>2</sup>	Piezoelectric coupling coefficient for stress charge form
$g$	matrix	3*6	m <sup>2</sup> /N	Piezoelectric coupling coefficient for strain voltage form
$q$	matrix	3*6	N/C	Piezoelectric coupling coefficient for stress voltage form

The modified electro-thermo-elastic constitutive equation including the nonlinearity due to polarization-electric field (P-E) interaction is given as (Ref. [7]).

$$\sigma_{ij} = c_{ijkl}\epsilon_{kl} - e_{ijk}E_k - P_iE_j - k_{ij}\theta \quad (2.2)$$

$$D_i = e_{ijk}\epsilon_{jk} + \epsilon_{ij}E_j + d_i\theta \quad (2.3)$$

$$\vec{D} = \epsilon_0 \vec{E} + \vec{P} \quad (2.4)$$

where,

P→Polarization

The linear part of the stress is given as  $\sigma_{ij}^L = c_{ijkl}\epsilon_{kl} - e_{ijk}E_k - k_{ij}\theta$ , and the nonlinear part is  $\sigma_{ij}^{NL} = -P_iE_j$

## 2.2 Property Matrix for a poled Piezoelectric Ceramic

A piezoelectric ceramic has only one type of piezoelectric matrix regardless of the symmetry of the constituent crystals. The ceramic is initially isotropic. This isotropy is

destroyed in the poling direction. In the direction perpendicular to the poling direction, the material is transversely isotropic. The elastic, dielectric and piezoelectric matrices for the cylindrical symmetry of poled PZT are shown below

$$c = \begin{bmatrix} c_{11} & c_{12} & c_{13} & 0 & 0 & 0 \\ c_{12} & c_{11} & c_{13} & 0 & 0 & 0 \\ c_{13} & c_{13} & c_{33} & 0 & 0 & 0 \\ 0 & 0 & 0 & c_{44} & 0 & 0 \\ 0 & 0 & 0 & 0 & c_{44} & 0 \\ 0 & 0 & 0 & 0 & 0 & c_{66} \end{bmatrix} \quad e = \begin{bmatrix} 0 & 0 & -e_{31} \\ 0 & 0 & -e_{31} \\ 0 & 0 & -e_{33} \\ 0 & -e_{15} & 0 \\ -e_{15} & 0 & 0 \\ 0 & 0 & 0 \end{bmatrix}$$

$$\varepsilon = \begin{bmatrix} \varepsilon_1 & 0 & 0 \\ 0 & \varepsilon_1 & 0 \\ 0 & 0 & \varepsilon_3 \end{bmatrix}$$

The subscripts 1, 2, 3, 4, 5, and 6 refer to x, y, z, yz, xz, and xy respectively.

## 2.3 Assumptions

Before deriving the equations necessary to generate the hysteresis and butterfly loops, let us consider the assumptions made in the formulation. The assumptions made are as follows (Fig. 2.7):

1. The planar surfaces of the disk are stress free and in view of the thinness of this disk we may assume that the stress  $\sigma_x$  and  $\sigma_y$  are zero throughout the specimen for all times.
2. We further restrict our considerations to isothermal conditions so that the absolute temperature is constant and need not be included.
3. Shear strains ( $\gamma_{yz} = \gamma_{xy} = \gamma_{zx} = 0$ ) and shear stresses are assumed to be zero.
4. Normal stress in z direction is assumed to be zero i.e.,  $\sigma_z = 0$ .
5. Piezoelectric material is transversely isotropic.

6. Electric field acts only in z-direction i.e.  $E_x=E_y = 0$ .
7. The poling direction of the piezo patches is along z-direction (see Fig. 2.7).

## 2.4 Models for *hysteresis* and *butterfly* loops

In the present study two models have been analysed. These are:

1. Complex Stiffness Model.
2. Improved Domain Switching Model.

### 2.4.1 Complex Stiffness Model

Imposing the necessary conditions (mentioned in the assumptions) in the constitutive Eqs. 2.2-2.3 , we obtain a set of reduced constitutive equations given by

$$\sigma_z = -c^*E_z + c^*\epsilon_z - P_zE_z \quad (2.5)$$

$$D_z = \epsilon^*E_z + e^*\epsilon_z \quad (2.6)$$

Where,

$$c^* = c_{33} - \frac{2e_{13}^2}{c_{11}+c_{12}}$$

$$e^* = \frac{2e_{13}e_{31}}{c_{11}+c_{12}} - c_{33}$$

$$\epsilon^* = \epsilon_3 + \frac{2e_{31}^2}{c_{11}+c_{12}}$$

But we know from Eq. 2.1 that,

$$D_z = P_z + \epsilon_0 \cdot E_z \quad (2.7)$$

$$\Rightarrow P_z = D_z - \epsilon_0 \cdot E_z \quad (2.8)$$

Substituting  $D_z$  from Eq. 2.6 into Eq. 2.8,

$$\Rightarrow P_z = (\varepsilon^* - \varepsilon_0)E_z + c^*\epsilon_z \quad (2.9)$$

Therefore, substituting  $P_z$  from Eq. 2.9 into Eq. 2.5 and putting  $\sigma_z = 0$  we get the following relation for strain

$$\epsilon_z = \frac{\varepsilon_1^* E_z^2 + e^* E_z}{c^* - e^* E_z} \quad (2.10)$$

and Eq. 2.9 can be written as,

$$P_z = \varepsilon_1^* E_z + e^* \epsilon_z \quad (2.11)$$

where,  $\varepsilon_1^* = \varepsilon^* - \varepsilon_0$ .

If we assume  $E_z = E_0 e^{i\omega t}$ , where  $\omega$  corresponds to the excitation frequency, the strain variation exhibits a  $2\omega$  variation due to the  $E_z^2$  term.

Strain in the above equation is a double harmonic function of electric field and this nonlinearity is responsible for the generation of butterfly loop. The material properties of PZT-5H are given in Table No. 2.1. Using these values, the Eqs. 2.10 and 2.11 can be written as

$$\epsilon_z = \frac{15168 * 10^{-12} E_0^2 * e^{i(2\omega t - 0.0336)} + 19.9 E_0 * e^{i(\omega t - 0.0325)}}{5.319 * 10^{10} - 19.9 E_0 * e^{i(\omega t - 0.0325)}}$$

$$P_z = 15168 * 10^{-12} * E_0 * e^{i(\omega t - 0.0336)} + 19.9 E_0 * e^{i(\omega t - 0.0325)} \epsilon_z \quad (2.12)$$

The factor  $\varepsilon_1^* \simeq 15168 * 10^{-12}$  is found to be negligible compared to  $e^* \simeq 19.9$  (multiplying factor of the linear term) and hence the butterfly loop can only be generated at higher electric fields. It was found in the literature survey that butterfly loop occurs at even low electric fields. So, we develop a model which would generate both the hysteresis and butterfly loops at even low electric fields.

## 2.4.2 Improved Domain Switching Model

This model incorporates the concept of *domain switching* in the complex stiffness model. It is a simplified version of the model developed in Ref. [14]. It is generally agreed that the hysteresis loop is a consequence of the delay in response of domain switching. From

a microscopic viewpoint, the mechanism of domain switching are not well understood. Hence it is difficult to formulate explicit theories based on the present knowledge of these mechanisms. On the other hand, polynomial relations which partially match the graphical representation of the loop have not proven to be completely satisfactory for one reason or the another. For instance, they yield multi-valued relations and inadmissible states between the electric displacement and the electric field, and they do not explicitly account for the time dependent effects of domain switching.

It is our intent to offer a macroscopic theoretical basis for the existence of the hysteresis loop. This theory is motivated by the fact that the effective number of dipoles aligned in the direction of the applied field is altered as domains switch, and this number obeys a rate law which depends linearly on the electric field. It was observed that the specific nature of the loop depends not only on the amplitude and the period of the cyclic field, but also on its entire temporal history. These considerations point to the fact that time must be an important factor in any theoretical consideration of the loop and this explains the inclusion of the rate law (in combination with the constitutive equations) in the modeling.

Therefore the modified electro-elastic constitutive equations after having included the important parameters i.e. the rate law and number of dipoles is given by

$$\sigma_{ij} = c_{ijkl}\epsilon_{kl} - e_{ijk}NE_k - P_iNE_j \quad (2.13)$$

$$D_i = e_{ijk}N\epsilon_{jk} + \epsilon_{ij}E_j \quad (2.14)$$

$$\vec{D} = \epsilon_0 \vec{E} + \vec{P} \quad (2.15)$$

Where,  $N$  is the effective number of aligned dipoles and it obeys a rate law given by

$$\dot{N} + aN = \bar{b}E \quad (2.16)$$

Where,  $a$  and  $\bar{b}$  are constants.

Let,  $E = E_0 e^{i\omega t}$

and  $N = \bar{N} e^{i\omega t}$

substituting the above two forms in rate law i.e. Eq. 2.16 we get

$$N = -\frac{b}{\sqrt{a^2 + \omega^2}} e^{i(\omega t - \phi)} \quad (2.17)$$

Where,  $b = \bar{b}E_0$

$$\phi = \tan^{-1}\left(\frac{\omega}{a}\right) \quad (2.18)$$

Substituting  $a=1$  and  $b=0.1$  in Eq. 2.17 the expression for  $N$  can be written as

$$N = -\frac{0.1}{\sqrt{1 + \omega^2}} e^{i(\omega t - \phi)}$$

Let  $A = -\frac{0.1}{\sqrt{1 + \omega^2}}$  then,

$$N = Ae^{i(\omega t - \phi)} \quad (2.19)$$

The reduced set of constitutive equations after imposing the necessary conditions is given as

$$\sigma_z = -e^* E_z N + c^* \epsilon_z - P_z E_z N \quad (2.20)$$

$$D_z = \epsilon^* E_z + c^* \epsilon_z N \quad (2.21)$$

From Eqs. 2.7 and 2.21 polarization can be written as,

$$P_z = (\epsilon^* - \epsilon_0) E_z + c^* \epsilon_z N$$

$$P_z = \epsilon_1^* E_z + c^* \epsilon_z N \quad (2.22)$$

Substituting  $P_z$  from Eq. 2.22 and imposing  $\sigma_z = 0$  (*stress free condition*) we obtain strain in terms of  $N$  and electric field. The relation is given as

$$\epsilon_z = \frac{\epsilon_1^* E_z^2 N + e^* E_z N}{c^* - e^* E_z N^2} \quad (2.23)$$

Substituting the values of  $\epsilon_1^*$ ,  $c^*$ ,  $e^*$ , and expression for  $N$  (Eq. 2.19) the Eqs. 2.23



and 2.22 can be written as

$$\epsilon_z = \frac{AE_0^2 * 15168 * 10^{-12} * e^{i(3\omega t - 0.0336 - \phi)} + AE_0 * 19.9 * e^{i(2\omega t - 0.0325 - \phi)}}{5.319 * 10^{10} - E_0 A^2 * 19.9 * e^{i(3 + \omega t - 0.0325 - 2 * \phi)}} \quad (2.24)$$

$$P_z = 15168 * 10^{-12} * e^{i(\omega t - 0.0336)} E_z + 19.9 * A * e^{i(\omega t - 0.0325 - \phi)} \epsilon_z$$

Strain is nonlinear in terms of electric field (Eq. 2.24) and this nonlinearity is responsible for the presence of butterfly loop even at low electric fields.

## 2.5 Results and Discussions

Hysteresis (polarization-electric field) and butterfly (strain-electric field) loops are plotted for the two different models discussed. The variation in nature or shape of these curves with change in different parameters is studied through these plots. Figures 2.8 and 2.9 represent the plots for complex stiffness model. Plots 2.8 (a), (b), and (c) show the variation of P-E and  $\epsilon - E$  loops with change in frequency. Electric field is fixed to a value of  $E_0 = 10^3 \text{ V/m}$  in these three plots. It is observed that there is no variation in these loops with variation in frequency. In Figs. 2.9 (a), (b), and (c), frequency of the system is kept constant (i.e.,  $f = 0.01 \text{ Hz}$ ) and the effect of electric field on the loops is studied. Drastic changes are observed in the loops with variation in the magnitude of electric field. The strain-electric field plot transforms into a double loop termed as “*butterfly loop*” at higher electric fields (of order of  $10^8 \text{ V/m}$ ). Even the hysteresis (P-E) loop transforms in a similar manner.

Figures 2.10-2.13 represent the behavior of hysteresis and butterfly loops with change in parameters defining the domain switching model. They clearly depict the effect of frequency, magnitude of electric field, parameters  $a$  and  $b$  defining the rate law, on the P-E and  $\epsilon - E$  loops. From Figs. 2.10 and 2.11 it is observed that the shapes of butterfly and hysteresis loops change drastically with change in frequency but there is no change observed with variation in electric field (from  $10^3 \text{ V/m}$  to  $10^6 \text{ V/m}$ ). From Figs. 2.10 (c) and 2.11 (c) it is observed that higher frequencies the butterfly loop transforms to a loop similar to that obtained for electrostrictive materials (Ref. [3]). In developing these

developing these figures (Figs. 2.10-2.11), the values of  $a=1$  and  $b=0.1$  are used. The effect of parameter " $b$ " on the loops can be clearly studied from Figs. 2.12 (a), (b), and (c). The butterfly loop expands with increase in  $b$  and the hysteresis loop transforms into a triple loop at higher value of  $b$  (for  $b=0.5$ ). From Figs. 2.13 (a), (b), and (c) it is observed that the butterfly loop shrinks gradually with increase in " $a$ " and not much change is observed in the hysteresis loop.

## 2.6 Summary

A mathematical model has been developed to represent the interaction of P-E (polarization and electric field) and domain switching has been developed to obtain the hysteresis and butterfly loops for a piezoelectric (PZT-5H) material. Basically two models are studied, one with domain switching and the other without it. The effect of inclusion of domain switching is shown to represent the physical phenomenon observed for PZT-materials. The effect of varying the parameters in the rate law (frequency, electric field,  $a$  and  $b$ ) on the P-E and  $\epsilon - E$  loops is analysed.

Table 2.1: Material Properties for PZT-5H

GPa					
$c_{11}$	$c_{12}$	$c_{13}$	$c_{33}$	$c_{44}$	$c_{66}$
138.33	93.16	95.06	131.26	21.05	21.05

$C/m^2$		
$e_{31}$	$e_{33}$	$e_{15}$
-4.0329+0.1313i	16.5815-0.539i	12.29-0.4i

$F/m$	
$\epsilon_1$	$\epsilon_3$
(15293-510i)* $10^{-12}$	(15028-501i)* $10^{-12}$

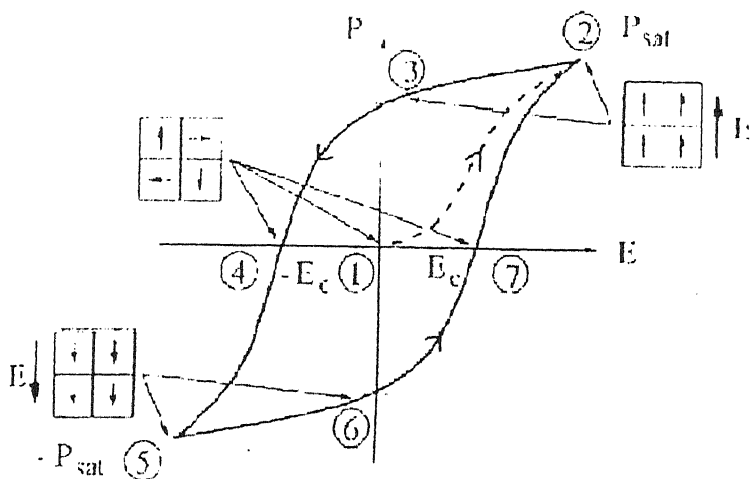


Figure 2.1: Hysteresis curve

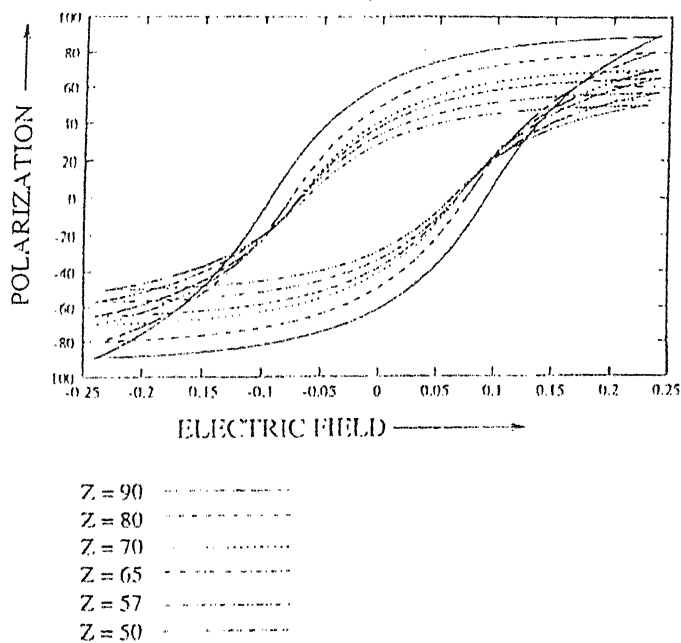


Figure 2.2: Change in hysteresis curve with respect to parallel compressive stress

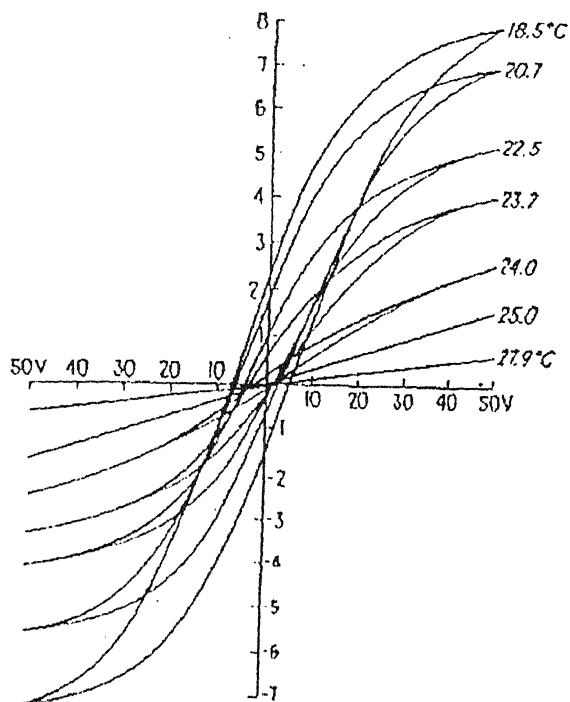


Figure 2.3: Effect of temperature on hysteresis loop

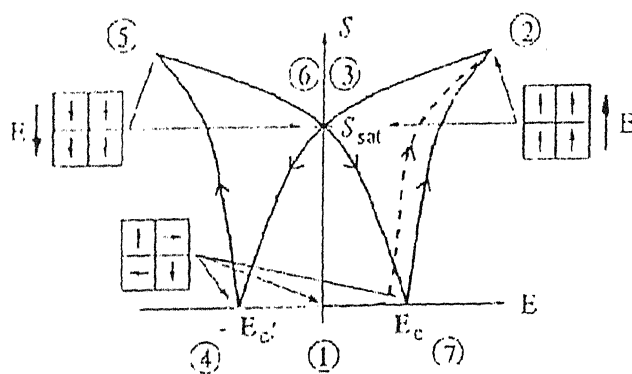


Figure 2.4: Butterfly Loop

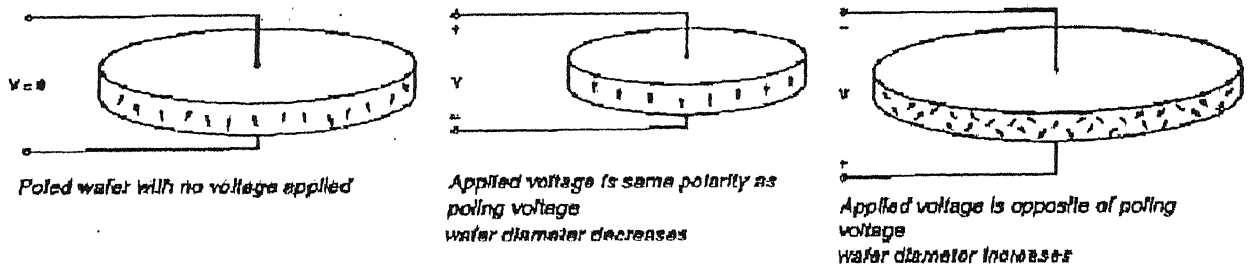
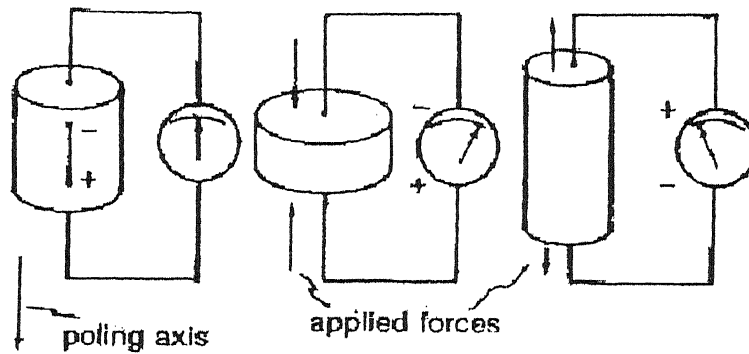
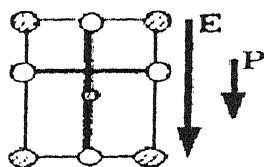
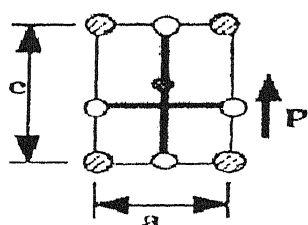
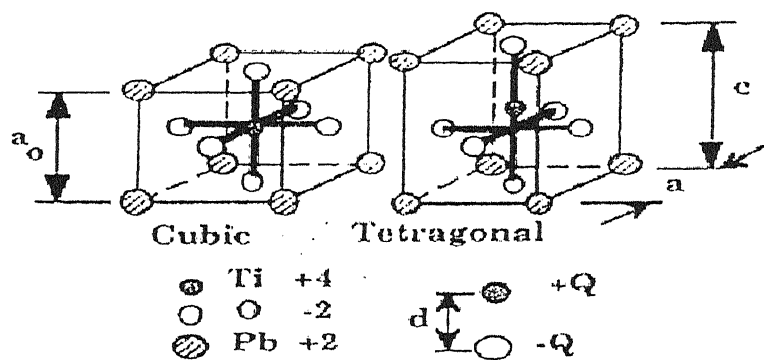
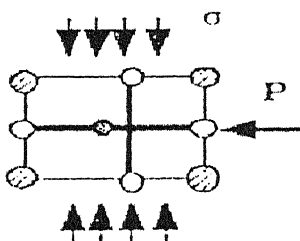
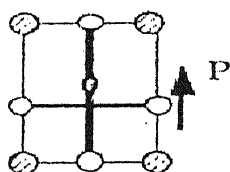


Figure 2.5: Dimensional changes of a poled wafer with an applied voltage. The dimensional changes are greatly exaggerated for clarity.

# Switching



← 180 degree switching



← 90 degree switching

Figure 2.6: Switching

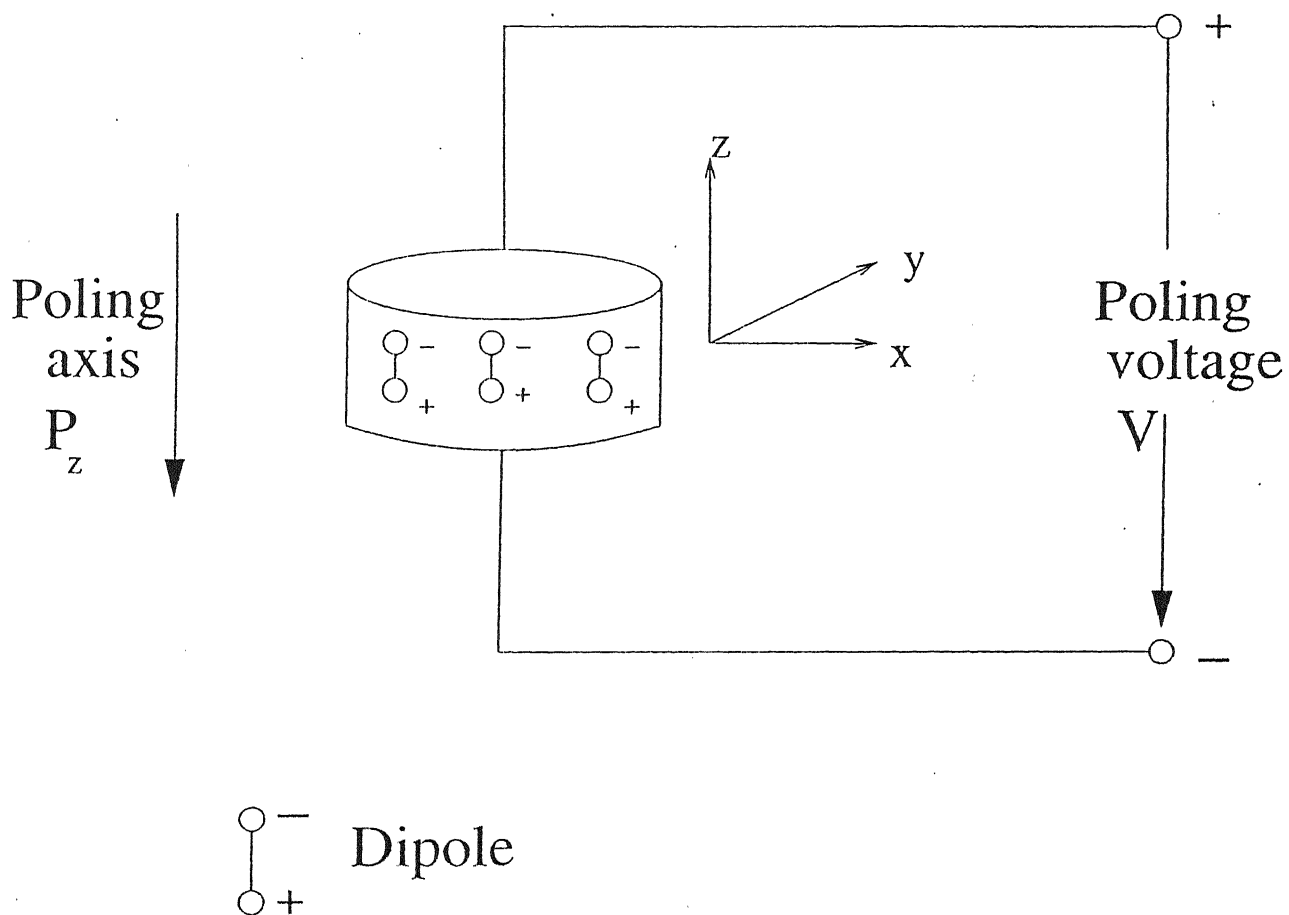
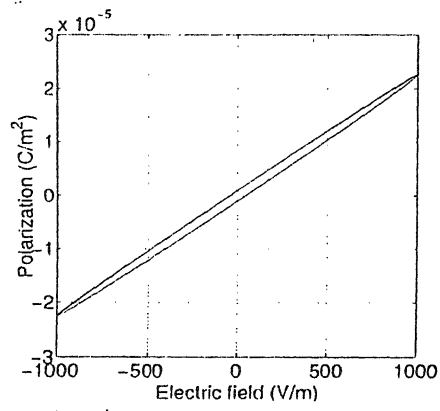
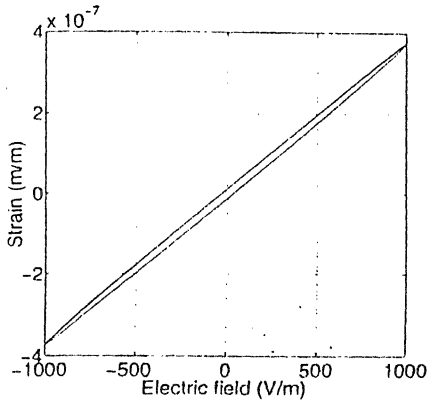
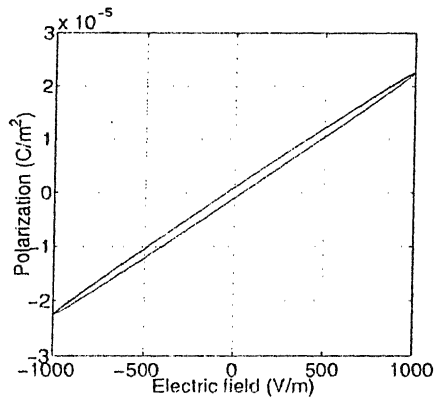
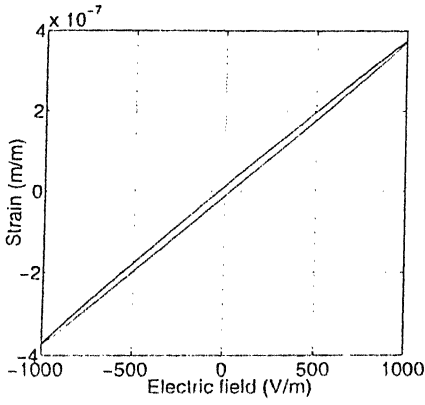


Figure 2.7: Poling in a piezo layer

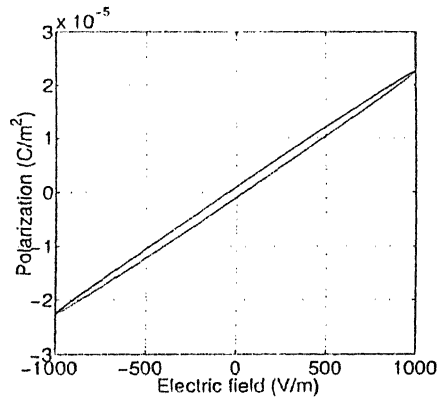
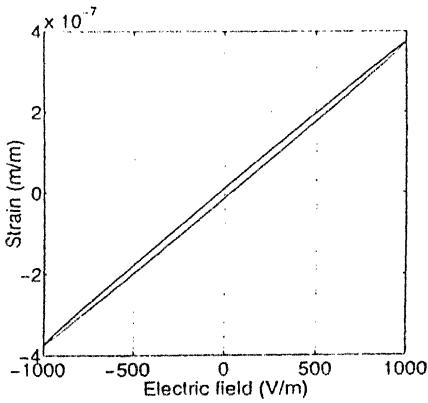




(a)  $f = 0.01 \text{ Hz}$

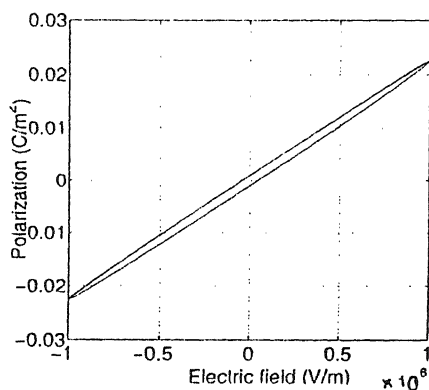
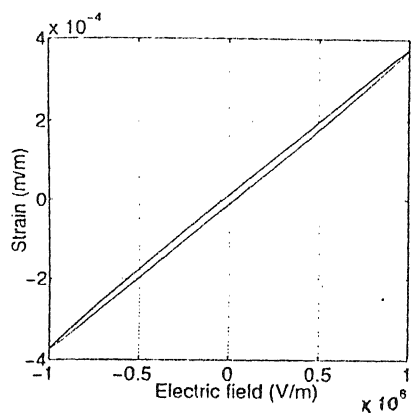


(b)  $f = 10 \text{ Hz}$

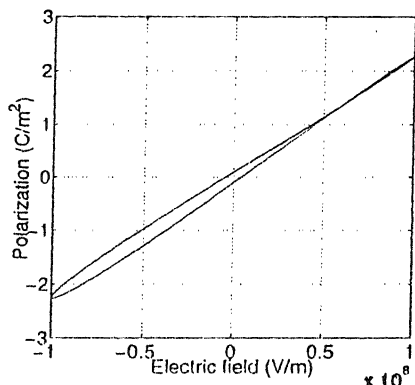
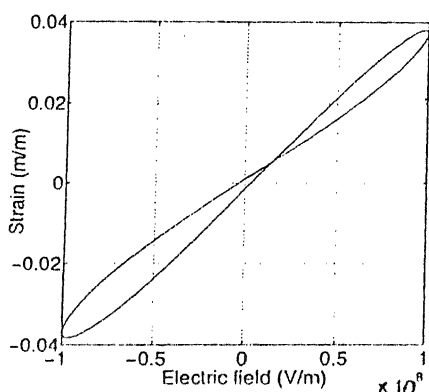


(c)  $f = 20 \text{ Hz}$

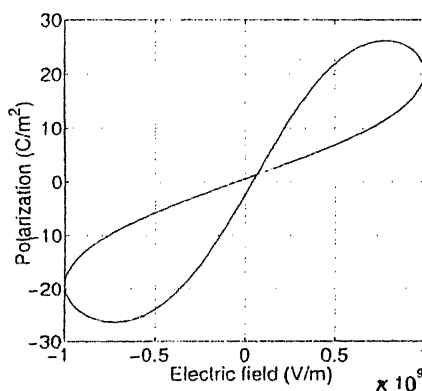
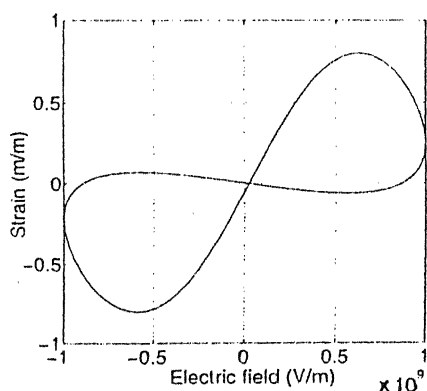
Figure 2.8: Variation of strain, polarization, and electric field ( $E=10^3 \text{ V/m}$ ) with frequency (complex stiffness model)



(a)  $E = 10^6 \text{ V/m}$

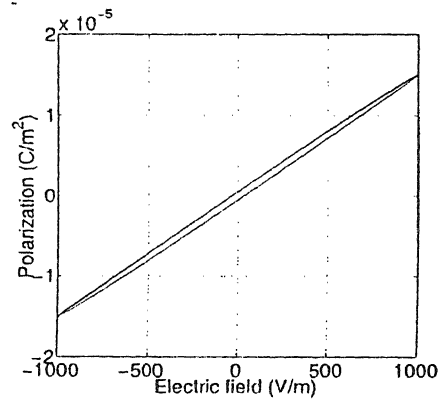
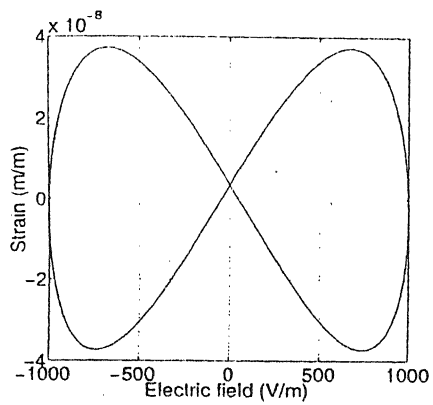


(b)  $E = 10^8 \text{ V/m}$

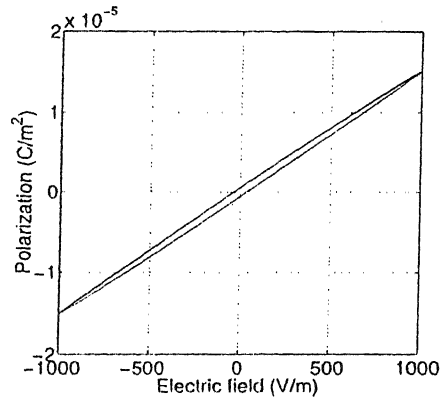
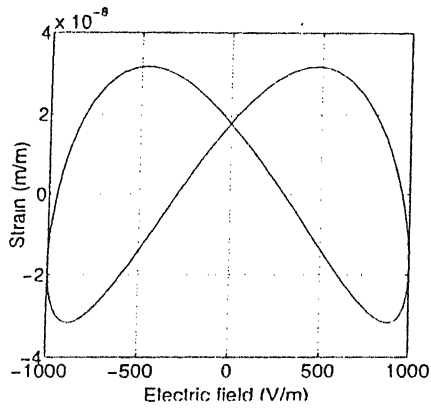


(c)  $E = 10^9 \text{ V/m}$

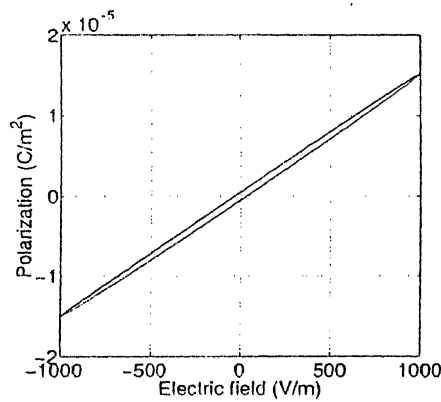
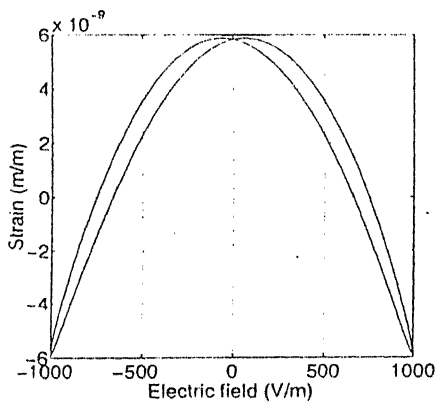
Figure 2.9: Variation of strain, polarization, and electric field with change in magnitude of electric field ( $f=0.01 \text{ Hz}$ ) (Complex stiffness model)



(a)  $f = 0.01 \text{ Hz}$

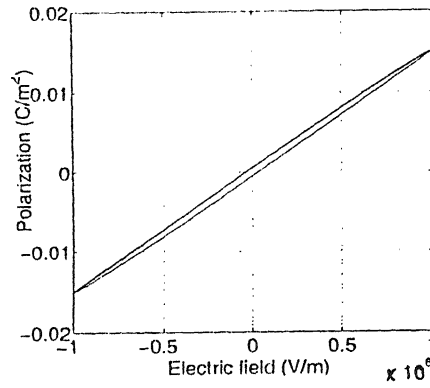
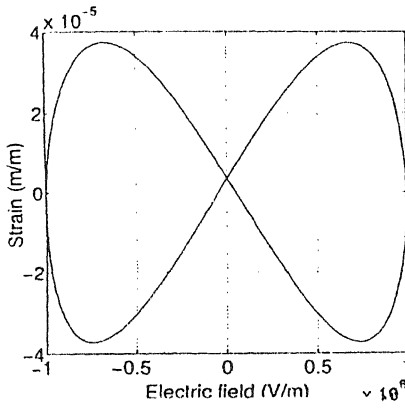


(b)  $f = 0.1 \text{ Hz}$

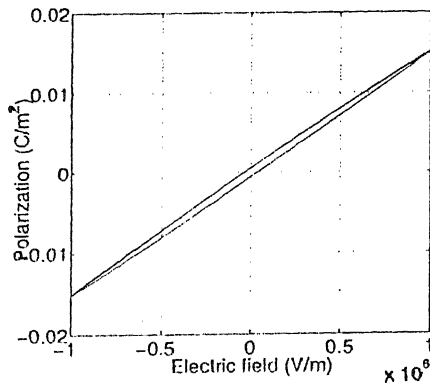
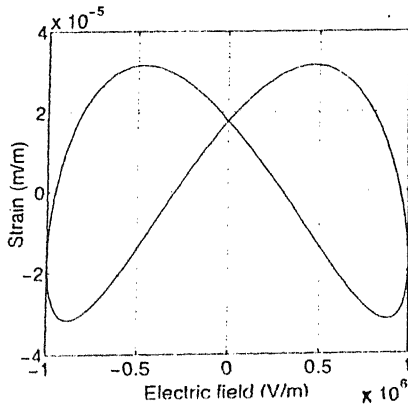


(c)  $f = 1 \text{ Hz}$

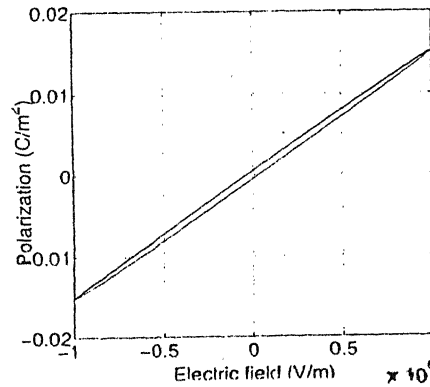
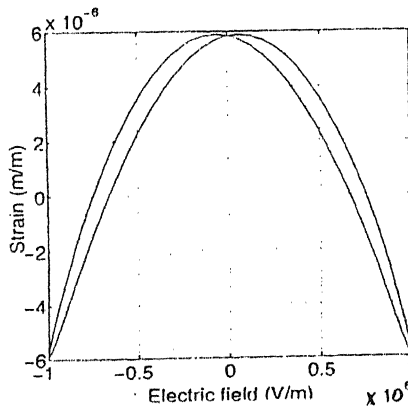
Figure 2.10: Variation in strain, polarization, and electric field ( $E=10^3 \text{ V/m}$ ) with frequency (domain switching model)



(a)  $f = 0.01 \text{ Hz}$

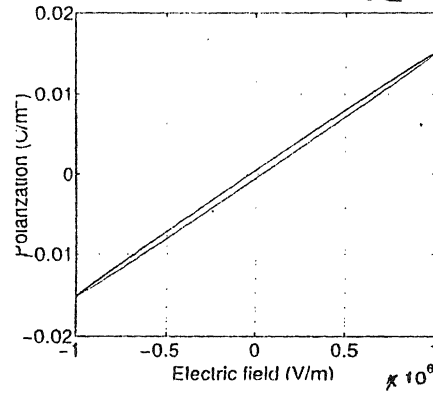
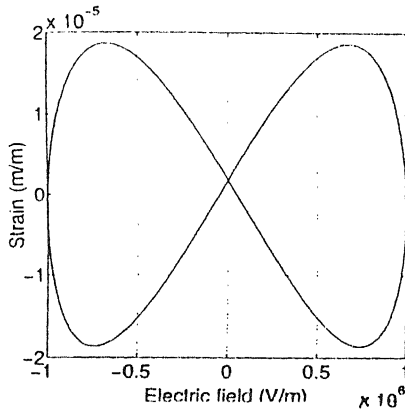


(b)  $f = 0.1 \text{ Hz}$

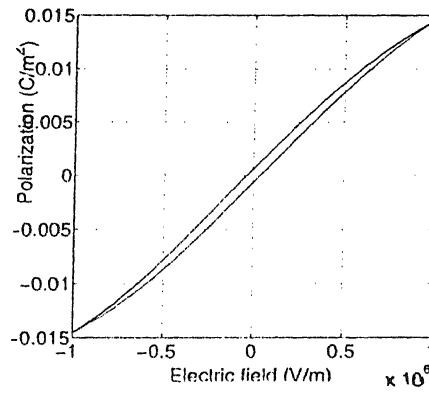
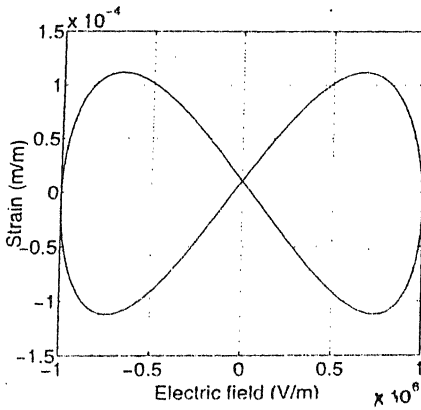


(c)  $f = 1 \text{ Hz}$

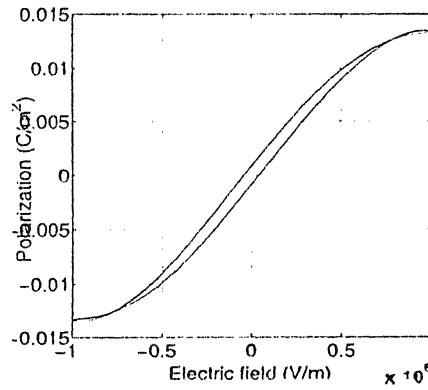
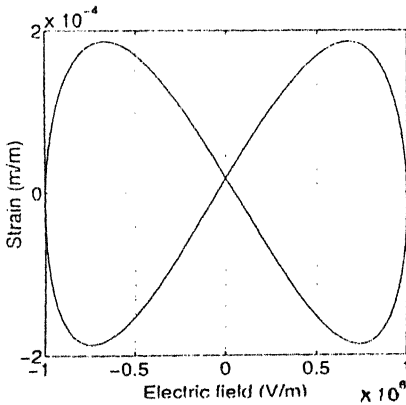
Figure 2.11: Variation in strain, polarization and electric field ( $E=10^6 \text{ V/m}$ ) with frequency (domain switching model)



(a)  $b=0.05$

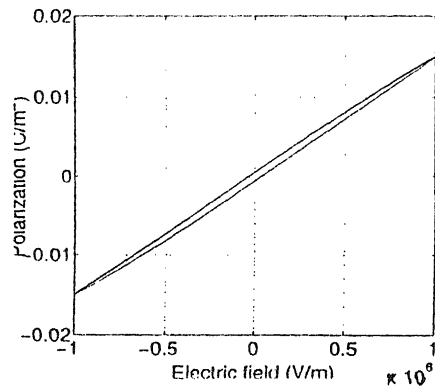
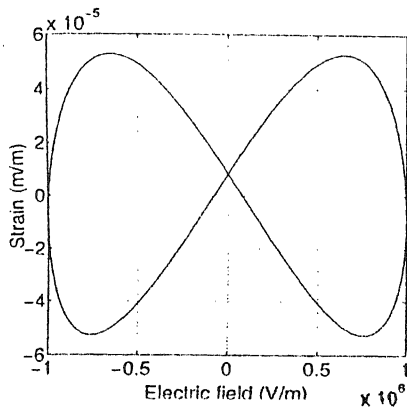


(b)  $b = 0.3$

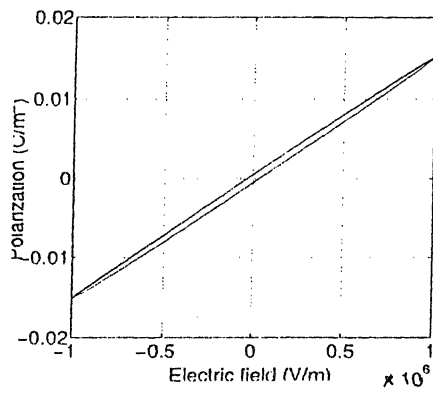
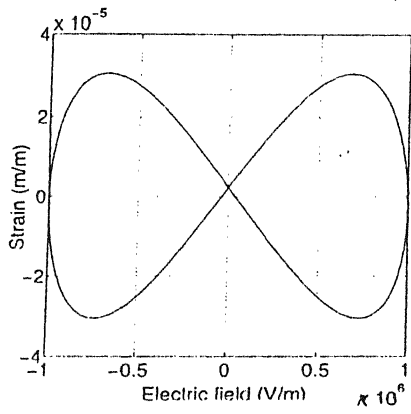


(c)  $b = 0.5$

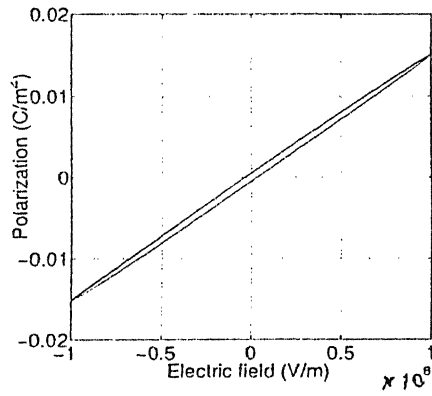
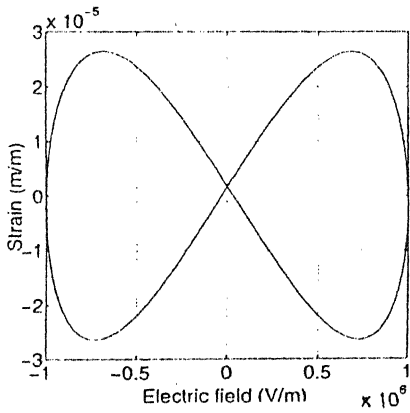
Figure 2.12: Variation in hysteresis and butterfly loops with change in parameter  $b$  ( $E=10^6$  V/m; frequency=0.01 Hz ;  $a=1$  ) (domain switching model)



(a)  $a = 0.5$



(b)  $a = 1.5$



(c)  $a = 2$

Figure 2.13: Variation in hysteresis and butterfly loops with change in parameter  $a$  ( $E=10^6$  V/m; frequency=0.01 Hz ;  $b=0.1$  ) (domain switching model)

## Chapter 3

# HEAT TRANSFER ANALYSIS OF SMART ACTUATOR

Heating of smart actuators is a major problem in the industry. We, in this study have tried to analyze the heat transfer that happens within the actuator i.e., as to what is the heat generated within the actuator and how it gets dissipated and what is the maximum temperature reached when conduction and convection from end faces; conduction and convection from all faces are considered? These are some very important questions that have been addressed in this study.

The hysteresis effect represents the energy loss. This energy loss is responsible for heat generation within the piezo material. The heat so generated, leads to heating up of the piezo layer tremendously, sometimes causing serious damages to the actuator. So, measures have to be taken to restrict this energy loss to a minimum. In this formulation, the temperature profile within the actuator is found out. For this the basic laws of heat transfer are considered (Refs. [25]-[27]).

### 3.1 Modes of Heat Transfer

The basic heat transfer (or heat dissipation) phenomena considered here are namely:

1. *Conduction* : When there exists a temperature gradient within a body, heat energy will flow from the region of high temperature to the region of low temperature. This phenomenon is known as conduction heat transfer, and is described by Fourier's Law

(named after the French physicist Joseph Fourier),

$$\vec{q} = -k\vec{\nabla}T$$

This equation determines the heat flux vector  $\vec{q}$  (quantity of heat/unit area) for a given temperature profile  $T$  and thermal conductivity  $k$ . The minus sign ensures that heat flows down the temperature gradient. For problems where the temperature variation is only 1-dimensional (say, along the  $z$ -coordinate direction), Fourier's Law of heat conduction simplifies to the scalar equations,

$$\vec{q} = -k\frac{\partial T}{\partial z} \quad Q = -kA\frac{\partial T}{\partial z} \quad (3.1)$$

In the above equation on the right,  $Q$  represents the heat flow through a defined cross-sectional area  $A$ , and it is measured in Watts,

$$Q = \int_A \vec{q} \cdot d\vec{A}$$

The 1D heat flow equation through a material thickness  $L$  is given as,

$$Q = \frac{kA}{L}(T_1 - T_2) \quad (3.2)$$

where  $T_1$  and  $T_2$  are the temperatures at the two boundaries (i.e., at  $z=0$  and  $z=L$ ).

2. *Convection* : Heat energy transfers between a solid and a fluid when there is a temperature difference between the fluid and the solid. This is known as "convection heat transfer". Generally, convection heat transfer can not be ignored when there is a significant fluid motion around the solid. The temperature of the solid, due to an external field such as fluid buoyancy, can induce a fluid motion. This is known as "natural convection" and it is a strong function of the temperature difference between the solid and the fluid. Blowing air over the solid by using external devices such as fans and pumps can also generate a fluid motion. This is known as "forced convection". Heat transfer due to free convection is described by Newton's Law of Cooling,

$$Q = hA(T_w - T_a) = hA \cdot \Delta T \quad (3.3)$$



The rate of heat transferred  $Q$  to the surrounding fluid is proportional to the object's exposed area  $A$ , and the difference between the object temperature  $T_w$  and the fluid free-stream temperature  $T_a$ . The constant of proportionality " $h$ " is termed the convection heat-transfer coefficient.

## 3.2 Analysis of Heat Transfer within the Actuator

The smart actuator is considered in actuation mode i.e., only external voltage is applied on the actuator (Fig. 3.1). The actuator consists of alternate layers of metal-piezo arrangement. The amount of heat generated is calculated from the area of *hysteresis* loop.

The heat generated/unit cycle/unit volume,  $\bar{q}$  is given as

$$\bar{q} = \frac{1}{T_P} \int_0^{T_P} P \frac{dE}{dt} dt \quad (3.4)$$

where  $P$  is the polarization which is given by Eq. 2.12,  $T_P$  is the time period, and  $E$  ( $=E_0 \sin \omega t$ ) is the electric field. Here  $E_0$  is taken to be  $10^6$  V/m.

Two distinct formulations are described in the following section.

### 3.2.1 Mode of Heat dissipation : Conduction and Convection from end faces

A layer-by-layer formulation is presented over here.

The general 3-D steady state heat conduction equation (obtained from the conservation of energy principle) is

$$\frac{\partial^2 T}{\partial x^2} + \frac{\partial^2 T}{\partial y^2} + \frac{\partial^2 T}{\partial z^2} + \frac{\bar{q}}{k} = 0 \quad (3.5)$$

Therefore, the 1-D steady state heat conduction equation is given as

$$\frac{\partial^2 T}{\partial z^2} + \frac{\bar{q}}{k} = 0 \quad (3.6)$$

where  $\bar{q}$  = energy generated per unit volume, W/m<sup>3</sup>

$k$  = Thermal conductivity

The smart actuator is a stack of alternate layers of metal and piezo material. Here, we consider the smart actuator to be a stack of “ $n$ ” layers.

1. First Metallic layer (Fig. 3.2)

Since there is no heat generation in this layer, the governing differential equation is

$$\frac{\partial^2 T}{\partial z^2} = 0 \quad (3.7)$$

subjected to boundary conditions that on face  $z=L_M$  the metallic layer is subjected to temperature  $T_2$  and on face  $z=0$  it is open to the atmosphere for convection (Fig. 3.2),

i.e., at  $z=0$ ,  $k_M \frac{dT}{dz} = h(T - T_a)$  and at  $z=L_M$ ,  $T = T_2$

where  $k_M$  and  $L_M$  are the thermal conductivity and length of the metallic layer

Solving Eq. 3.7 and using the boundary conditions, we get the following relation for temperature profile

$$T(z) = c_1 z + c_2$$

where,  $c_1 = \frac{T_2 - T_a}{L_M + (k_M/h)}$  and  $c_2 = \frac{T_2(k_M/h) - T_a L_M}{L_M + (k_M/h)}$

2. Last metallic layer ( $n$  th layer)

For this element, the boundary conditions are:

at  $z=L_M$ ,  $-k_M \frac{dT}{dz} = h(T - T_a)$  and at  $z=0$ ,  $T = T_1$  (Fig. 3.3)

where  $k_M$  and  $L_M$  are the thermal conductivity and length of the metallic layer.

The temperature profile in this case is given as

$$T(z) = c_1 z + c_2$$

where,  $c_1 = \frac{T_a - T_1}{L_M + (k_M/h)}$  and  $c_2 = T_1$

3. Metallic layer (between two piezo layers)

The boundary conditions in this case are

at  $z=0$ ,  $T = T_1$  and at  $z=L_M$ ,  $T = T_2$  (Fig. 3.4)

Then the temperature profile is

$$T(z) = c_1 z + c_2$$

where,  $c_1 = \frac{T_2 - T_1}{L_M}$  and  $c_2 = T_1$

#### 4. Piezo layer

The differential equation in this case is slightly modified (as compared to the other two) to include the internal heat generation term and is given as

$$\frac{\partial^2 T}{\partial z^2} + \frac{\bar{q}}{k_P} = 0$$

The boundary conditions in this case are at  $z=0$ ,  $T = T_1$  and at  $z=L_P$ ,  $T = T_2$  (Fig. 3.5)

where  $k_P$  and  $L_P$  are the thermal conductivity and length of the piezo layer. The temperature profile is obtained as

$$T(z) = T_1 + (T_2 - T_1) \frac{z}{L_P} + \frac{\bar{q} L_P^2}{2k_P} \left[ \frac{z}{L_P} - \left( \frac{z}{L_P} \right)^2 \right]$$

When a combination of Metal-Piezo-Metal layers is taken for example, (MPM block as shown in Fig. 3.6) then the temperature profile of the entire bar is given as a function of temperatures  $T_2$  and  $T_3$  (i.e., temperatures at second and third junctions as shown in Fig. 3.6). The heat continuity conditions at the interfaces are respectively

$$-k_M \frac{dT}{dz} (at\ z = L_M)_{i-1} = -k_P \frac{dT}{dz} (at\ z = 0)_i \quad (Metal - Piezo\ interface)$$

$$-k_P \frac{dT}{dz} (at\ z = L_P)_i = -k_M \frac{dT}{dz} (at\ z = 0)_{i+1} \quad (Piezo - Metal\ interface)$$

The subscript denotes the layer number.

Similarly any number of alternate layers of metal and piezo can be taken for analysis. In the present formulation a bar of 25 layers (made up of alternate layers of metal and piezo i.e., MPM....PM) is analyzed.

### 3.2.2 Mode of Heat Dissipation : Conduction and Convection from all faces

In the earlier formulation convection from the cylindrical surface has been neglected. The procedure for inclusion of convection from all the faces is described in this section.

We approach the problem by making an energy balance on an element of thickness  $dz$ . Thus

Energy flow through left face  $-$  energy flow through right face  $+$  energy lost by convection (energy balance for a metallic layer Fig. 3.7)

$$Q_z = Q_{z+dz} + h\bar{P}_M dz(T - T_a)$$

where,  $\bar{P}_M$  is the perimeter,  $Q_z = -k_M A \frac{dT}{dz}$  and  $Q_{z+dz} = -k_M A \left( \frac{dT}{dz} + \frac{d^2T}{dz^2} dz \right)$   
And energy balance for piezo layer (Fig. 3.8),

$$Q_z + Q_g = Q_{z+dz} + h\bar{P}_P dz(T - T_a)$$

where  $Q_g$  (heat generated)  $= \bar{q} A dz$ ,  $\bar{P}_P$  is the perimeter,  $Q_z = -k_P A \frac{dT}{dz}$  and  $Q_{z+dz} = -k_P A \left( \frac{dT}{dz} + \frac{d^2T}{dz^2} dz \right)$

Substituting for  $Q_z$  and  $Q_{z+dz}$  one obtains

$$\frac{d^2T}{dz^2} - \frac{h\bar{P}}{kA}(T - T_a) = 0$$

The layer-by-layer formulation is given as

#### 1. First metallic layer

The governing differential equation applicable to this case is given as

$$\frac{\partial^2 T}{\partial z^2} - \frac{h\bar{P}_M}{k_M A}(T - T_a) = 0$$

Let  $\theta = (T - T_a)$  and  $m_M^2 = \frac{h\bar{P}_M}{k_M A}$

Then it follows that

$$\frac{\partial^2 \theta}{\partial z^2} - m_M^2 \theta = 0 \quad (3.8)$$

The boundary conditions are given as

at  $z=0$ ,  $k_M \frac{d\theta}{dz} = h\theta$  and  $z = L_M$ ,  $\theta = \theta_2$  (Fig. 3.2)

Solving eq. 3.8 and using the above given boundary conditions, we obtain a temperature profile as follows

$$\theta(z) = \frac{\theta_2}{\cosh(m_M L_M) + \frac{h}{m_M k_M} \sinh(m_M L_M)} \left[ \cosh(m_M z) + \frac{h}{m_M k_M} \sinh(m_M z) \right]$$

2. n th metallic layer (Fig. 3.3)

For this element the boundary conditions are given as

at  $z=L_M$ ,  $-k_M \frac{d\theta}{dz} = h\theta$  and at  $z=0$ ,  $\theta = \theta_1$

The temperature profile for this case is given as

$$\theta(z) = \theta_1 \frac{\left[ \cosh(m_M(L_M - z)) + \frac{h}{m_M k_M} \sinh(m_M(L_M - z)) \right]}{\cosh(m_M L_M) + \frac{h}{m_M k_M} \sinh(m_M L_M)}$$

3. Metallic layer (between two piezo layers)

The boundary conditions in this case are

at  $z=0$ ,  $\theta = \theta_1$  and at  $z=L_M$ ,  $\theta = \theta_2$  (Fig. 3.4)

Then the temperature profile is

$$\theta(z) = \frac{\theta_2 \sinh(m_M z) + \theta_1 \sinh(m_M(L_M - z))}{\sinh(m_M L_M)}$$

4. Piezo layer

The differential equation in this case is slightly modified (as compared to the other two) to include the internal heat generation term and is given as

$$\frac{\partial^2 \theta}{\partial z^2} - m_P^2 \theta + \frac{\bar{q}}{k_P} = 0$$

where,  $m_P^2 = \frac{h P_P}{k_P A}$ .

The boundary conditions in this case are at  $z=0$ ,  $\theta = \theta_1$  and at  $z=L_P$ ,  $\theta = \theta_2$  (Fig. 3.5). Hence the temperature profile is given as

$$\theta(z) = \frac{(\theta_1 - \frac{\bar{q}}{k_P m_P^2}) \sinh(m_P(L_P - z)) + (\theta_2 - \frac{\bar{q}}{k_P m_P^2}) \sinh(m_P z)}{\sinh(m_P L_P)} + \frac{\bar{q}}{k_P m_P^2}$$

When a combination of these layers is taken (for example MPM block as shown in Fig. 3.6), then the temperature profile can be found out in terms of  $\theta_2$  ( $T_2 - T_a$ ) and  $\theta_3$  ( $T_3 - T_a$ ). These quantities are obtained by imposing the following heat continuity conditions

$$-k_M \frac{d\theta}{dz} (at\ z = L_M)_{i-1} = -k_P \frac{d\theta}{dz} (at\ z = 0)_i$$

$$-k_P \frac{d\theta}{dz} (at\ z = L_p)_i = -k_M \frac{d\theta}{dz} (at\ z = 0)_{i+1}$$

Similarly any number of alternate layers of metal and piezo materials can be analyzed. In the present formulation a bar of 25 layers (made up of alternate layers of metal and piezo i.e., MPM....PM) is analyzed.

### 3.3 Results and Discussion

Using the above heat transfer formulation, the temperature profile of a piezo stack actuator acted on by a harmonic electric field ( $E_0=10^6\text{V/m}$ ) is studied. In the present formulation a bar of 25 layers (made up of alternate layers of metal and piezo i.e., MPM....PM) is analyzed. The metallic layers are of length 0.5 mm and the piezo layers are 1.5 mm thick. The material and geometric data are given in Tables 3.1 and 3.2.

The temperature profile within the actuator for various cases is shown in Figs. 3.9 and 3.10. The results can be summarized as follows

1. The temperature profile obtained in all cases is symmetric about the center of the bar (Fig. 3.9).
2. For the case, where convection from the surface area of the bar is neglected, it is observed that for an increase in frequency by 10 Hz the maximum temperature reached by the bar goes up by  $\simeq 28^\circ\text{K}$  as shown in Fig. 3.9.
3. For the case, where convection is allowed to happen from the surface area of the bar, then it is observed that for an increase in frequency by 10 Hz the maximum temperature reached by the bar goes up by  $\simeq 2^\circ\text{K}$  as shown in Fig. 3.9. These results indicate that inclusion of convection (from the surface area of the bar) reduces the temperature increase substantially.

The same calculations were repeated for the case where steel is chosen as metallic layer. The temperature profiles obtained were found to be similar as in the earlier case (Fig. 3.10).

### 3.4 Summary

Heating of piezo actuators is a major problem in the industry. An attempt is made to formulate the heat transfer problem applicable for piezo actuators. Through this formulation we come to know the maximum temperature reached by the actuator. The effect of inclusion of convection mode of heat dissipation in addition to conduction is also brought out. It was observed that for the same frequency the maximum temperature reached was much higher in the former model (model excluding the convection from the surface area of the bar) as compared to that obtained by latter model (model including the convection from all faces of the bar). From the results it was found that the profile was symmetric about the centre of the bar.

Table 3.1: Material Properties for PZT-5H

GPa					
$c_{11}$	$c_{12}$	$c_{13}$	$c_{33}$	$c_{44}$	$c_{66}$
138.33	93.16	95.06	131.26	21.05	21.05

$C/m^2$		
$e_{31}$	$e_{33}$	$e_{15}$
-4.0329+0.1313i	16.5815-0.539i	12.29-0.4i

$F/m$	
$\epsilon_1$	$\epsilon_3$
(15293-510i)* $10^{-12}$	(15028-501i)* $10^{-12}$

Table 3.2: Data used for heat transfer analysis

Diameter of the bar = 1 mm
Length of the bar = 24.5 mm
Number of layers = 25 (alternate MP..M)
Thickness of the metal layer = 0.5 mm
Thickness of the piezo layer = 1.5 mm
Ambient temperature = 300 K
Thermal conductivity of Al = 237 W/mK
Thermal conductivity of Steel = 23 W/mK
Thermal conductivity of PZT-5H = 1.8 W/mK
Heat transfer coefficient for natural convection by air = 5 W/m <sup>2</sup> K



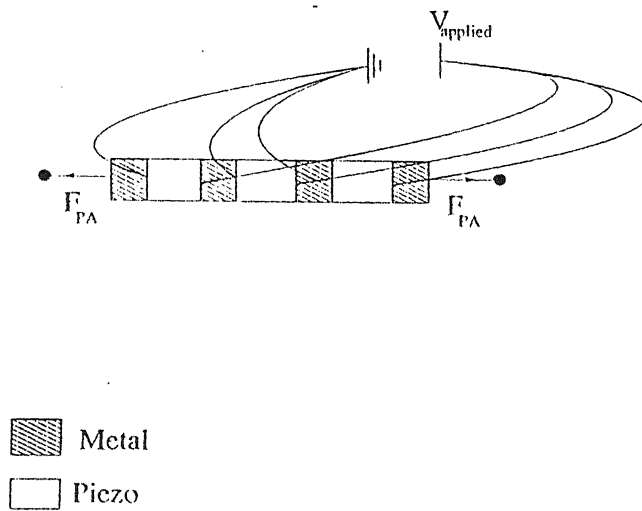


Figure 3.1: Piezo stack actuator

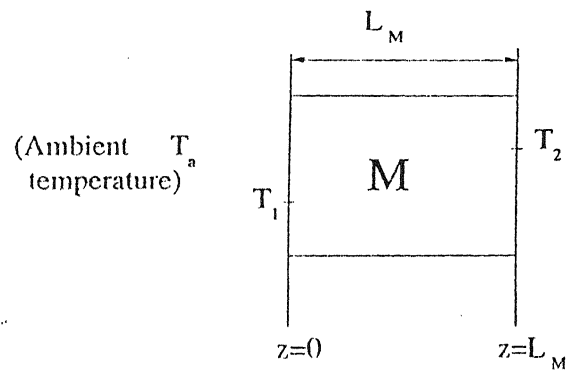


Figure 3.2: First metallic layer

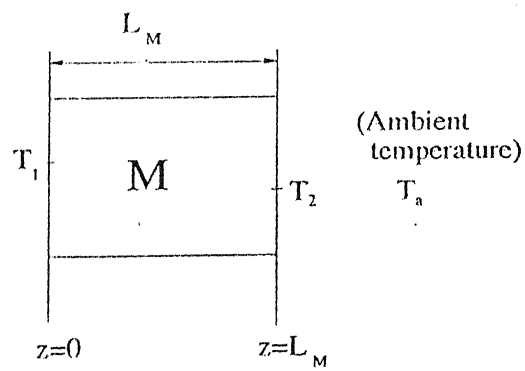


Figure 3.3:  $n$  th metallic layer

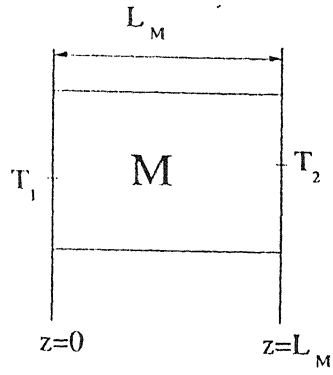


Figure 3.4: Metallic layer (between 2 piezo layers)

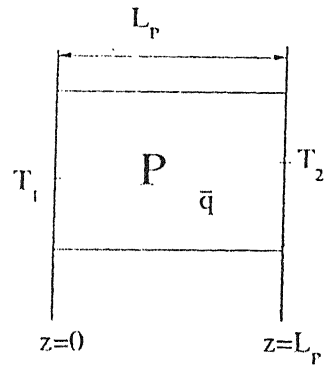


Figure 3.5: Piezo layer

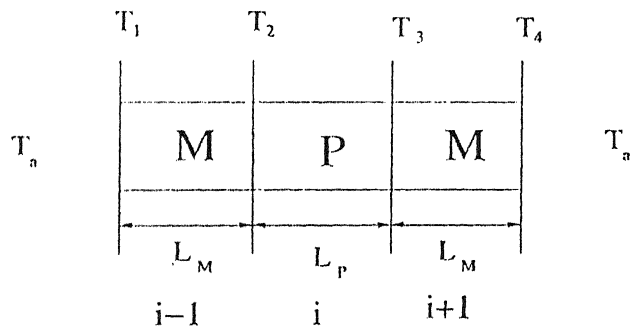


Figure 3.6: MPM block

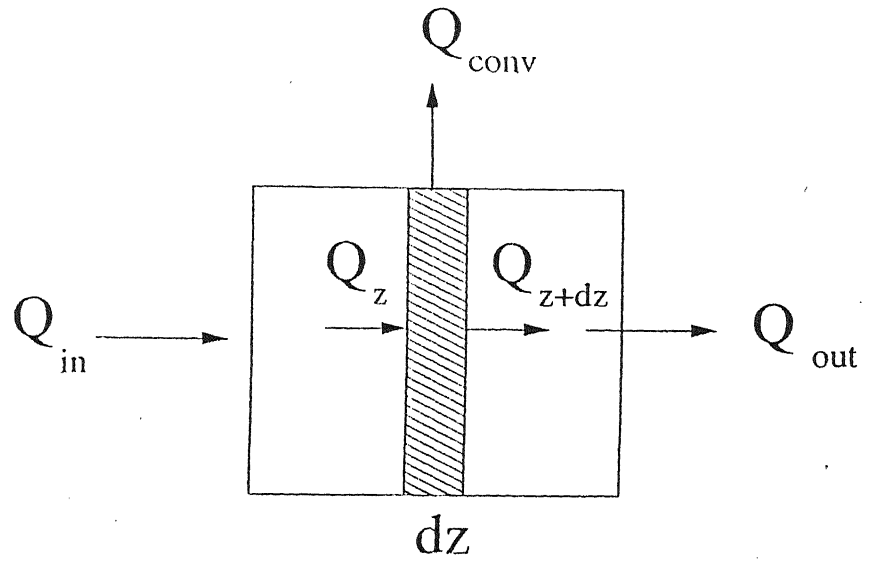


Figure 3.7: Energy balance for the metallic layer

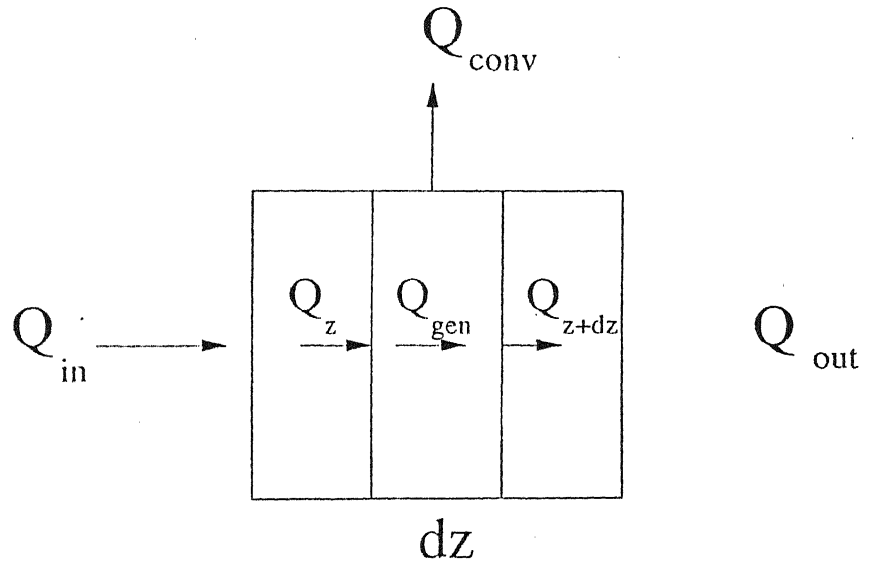
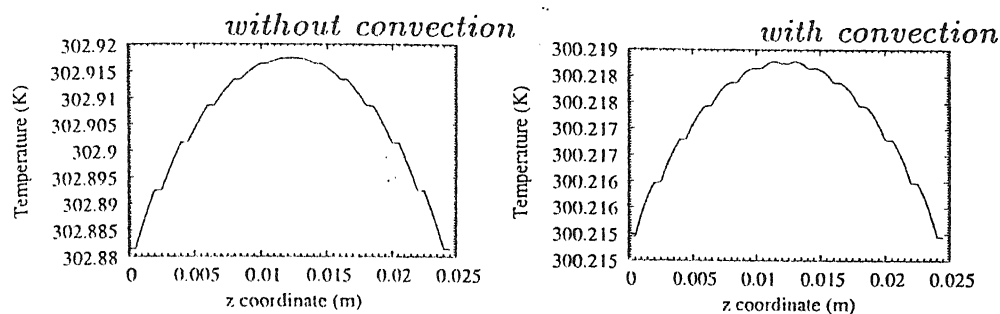
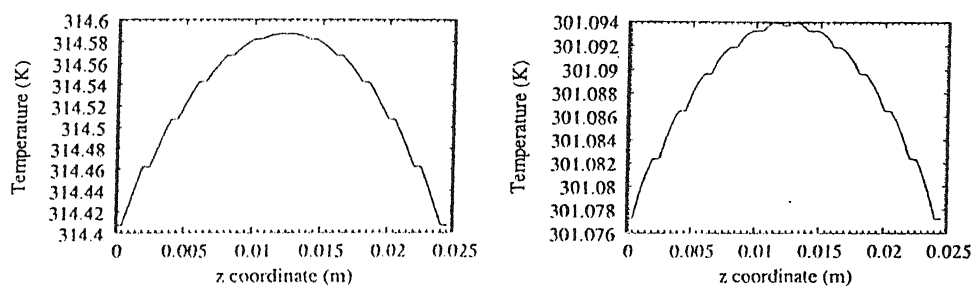


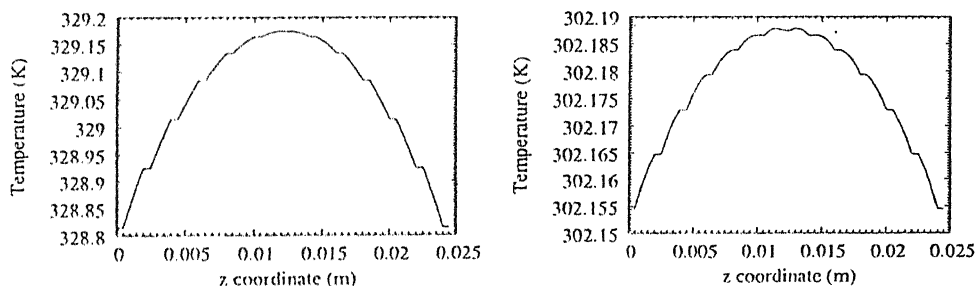
Figure 3.8: Energy balance for the piezo layer



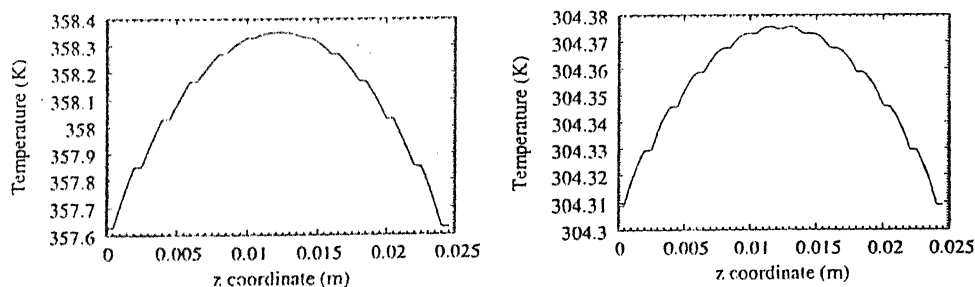
(a) frequency = 1 Hz



(b) frequency = 5 Hz



(c) frequency = 10 Hz



(d) frequency = 20 Hz

Figure 3.9: Plots of temperature profiles across the bar (when Al is the metallic layer)

## Chapter 4

# MODELING OF SMART ACTUATOR

In this chapter a *finite element formulation* is carried out to obtain a relation between deformation, potential and external load acting at the ends of the smart actuator. The smart actuator is a circular bar which consists of a stack of alternate layers of metal and piezoelectric material. The smart bar acts like a sensor (Fig. 4.1a) when induced potential is measured due to deformation caused by the external load. Similarly the bar can be used as an actuator (Fig. 4.1b) when external potential is applied across piezo patches to create deformation and force at the ends of the smart bar.

PZT-5H is the material chosen for the piezo layer in the present formulation. Bar model is shown in Fig. 4.2. The assumptions considered in this formulation are :

1. The planar surfaces of the disk are stress free and in view of the thinness of this disk we may assume that the stress  $\sigma_x$  and  $\sigma_y$  are zero throughout the specimen for all times.
2. We further restrict our considerations to isothermal conditions so that the absolute temperature is constant and need not be included.
3. Shear strains ( $\gamma_{yz} = \gamma_{xy} = \gamma_{zx} = 0$ ) and shear stresses are assumed to be zero.
4. Piezoelectric material is transversely isotropic.
5. Electric field acts only in z-direction i.e.  $E_x = E_y = 0$ .

### Finite Element Formulation:-

The finite element formulation is based on using the variational principle. The variational form of the linear electro-elastic problem is given as follows (Ref. [6])

$$\int_V \sigma_{ij}^L \delta \epsilon_{ij} dV - \int_V D_i \delta E_i dV = \int_S \bar{T}_i \delta u_i dS$$

For a piezo layer, in the absence of traction force, the variational formulation is given as

$$\int_V \sigma_z^L \delta \epsilon_z dV - \int_V D_z \delta E_z dV = 0 \quad (4.1)$$

In this study, we have not considered the nonlinearity due to P-E interaction. Therefore the reduced constitutive equations for a linear case are given by,

$$\sigma_z = -c^* E_z + c^* \epsilon_z \quad (4.2)$$

$$D_z = \epsilon^* E_z + c^* \epsilon_z \quad (4.3)$$

Where,

$$c^* = c_{33} - \frac{2c_{13}^2}{c_{11} + c_{12}}$$

$$c^* = \frac{2c_{13}c_{31}}{c_{11} + c_{12}} - c_{33}$$

$$\epsilon^* = \epsilon_3 + \frac{2c_{31}^2}{c_{11} + c_{12}}$$

Substituting the constitutive Eq 4.2 and 4.3 in the variational formulation (Eq. 4.1) implies

$$\int_V (c^* \epsilon_z - c^* E_z) \delta \epsilon_z dV - \int_V (\epsilon^* E_z - c^* \epsilon_z) \delta E_z dV = 0 \quad (4.4)$$

Substituting for  $\epsilon_z = \frac{\partial u}{\partial z}$  and  $E_z = -\frac{\partial \Phi}{\partial z}$ , Eq. 4.4 can be written as,

$$\int_V (c^* \frac{\partial u}{\partial z} + c^* \frac{\partial \Phi}{\partial z}) \frac{\partial \delta u}{\partial z} dV + \int_V (-\epsilon^* \frac{\partial \Phi}{\partial z} + c^* \frac{\partial u}{\partial z}) \frac{\partial \delta \Phi}{\partial z} dV = 0$$

Integrating over the cross-sectional area, we have

$$A \int_0^{L_p} (c^* \frac{\partial u}{\partial z} + e^* \frac{\partial \Phi}{\partial z}) \frac{\partial \delta u}{\partial z} dz + A \int_0^{L_p} (-\epsilon^* \frac{\partial \Phi}{\partial z} + e^* \frac{\partial u}{\partial z}) \frac{\partial \delta \Phi}{\partial z} dz = 0$$

A finite element formulation has been developed using a layer-by-layer model satisfying displacement continuity. Both axial displacement  $u$  and electric potential  $\Phi$  are assumed to be quadratic functions of  $z$ . The element used for modeling the piezo patch has three nodes. Each node has two degrees of freedom. These correspond to one extensional displacement in  $z$ -direction and one electric potential in poling direction. This results in a stiffness matrix of the order of  $6 \times 6$  for the piezo patch element. Whereas the element for the non-piezo material has three nodes, having one degree of freedom per node. These correspond to one extensional degree of freedom in the poling direction. This results in a stiffness matrix of the order of  $3 \times 3$  for the non piezo material (Fig. 4.3).

The axial displacement and electric potential are given in the discretized form as

$$\begin{aligned} u(z) &= \sum_{j=1}^3 u_j N_j & \delta u_i &= \delta u_i N_i \\ \Phi_z &= \sum_{j=1}^3 \Phi_j N_j & \delta \Phi_i &= \delta \Phi_i N_i \end{aligned}$$

where  $u_j$  and  $\Phi_j$  are nodal degrees of freedom (Lagrangian) and  $N_j$  are the shape functions.

$$N_1 = (1 - \frac{z}{L_p})(1 - \frac{2z}{L_p})$$

$$N_2 = (\frac{4z}{L_p})(1 - \frac{z}{L_p})$$

$$N_3 = (-\frac{z}{L_p})(1 - \frac{2z}{L_p})$$

Substituting  $u$  and  $\Phi$  in the virtual work formulation we get

$$\begin{aligned} & A \int_0^{L_p} (c^* u_j \frac{\partial N_j}{\partial z} + e^* \Phi_j \frac{\partial N_j}{\partial z}) \frac{\partial N_i}{\partial z} \delta u_i dz \\ & + A \int_0^{L_p} (-\epsilon^* \Phi_j \frac{\partial N_j}{\partial z} + e^* u_j \frac{\partial N_j}{\partial z}) \frac{\partial N_i}{\partial z} \delta \Phi_i dz = 0 \end{aligned} \quad (4.5)$$

On substitution of  $u$ ,  $\Phi$ ,  $\delta u$ ,  $\delta \Phi$ , we get the *local stiffness matrix for the piezo layer*, which is given as,

$$K_P = \frac{A}{L_P} \begin{bmatrix} \frac{7c^*}{3} & \frac{-8c^*}{3} & \frac{c^*}{3} & \frac{7c^*}{3} & \frac{-8c^*}{3} & \frac{c^*}{3} \\ \frac{-8c^*}{3} & \frac{16c^*}{3} & \frac{-8c^*}{3} & \frac{-8c^*}{3} & \frac{16c^*}{3} & \frac{-8c^*}{3} \\ \frac{c^*}{3} & \frac{-8c^*}{3} & \frac{7c^*}{3} & \frac{c^*}{3} & \frac{-8c^*}{3} & \frac{7c^*}{3} \\ \frac{7c^*}{3} & \frac{-8c^*}{3} & \frac{c^*}{3} & \frac{-7c^*}{3} & \frac{8c^*}{3} & \frac{-c^*}{3} \\ \frac{-8c^*}{3} & \frac{16c^*}{3} & \frac{-8c^*}{3} & \frac{8c^*}{3} & \frac{-16c^*}{3} & \frac{8c^*}{3} \\ \frac{c^*}{3} & \frac{-8c^*}{3} & \frac{7c^*}{3} & \frac{-c^*}{3} & \frac{8c^*}{3} & \frac{-7c^*}{3} \end{bmatrix}$$

The nodal displacement vector is

$$\begin{bmatrix} u_1 \\ u_2 \\ u_3 \\ \Phi_1 \\ \Phi_2 \\ \Phi_3 \end{bmatrix}$$

These are also called as *Primary Variables*

*Element stiffness matrix for a metallic layer* (Ref. [24])

$$K_M = \frac{\tilde{E}A}{3L_M} \begin{bmatrix} 7 & -8 & 1 \\ -8 & 16 & -8 \\ 1 & -8 & 7 \end{bmatrix}$$

where  $\tilde{E}$  is the Young's Modulus of Elasticity.

The nodal displacement vector in this case is given as

$$\begin{bmatrix} u_1 \\ u_2 \\ u_3 \end{bmatrix}$$

In deriving the element equations, we isolated a typical element from the mesh and formulated the variational problem and developed its finite element model. To solve the total problem, we put the element back into their original position. In doing this before discretization, we impose continuity of the primary variables at the connecting nodes between elements. Continuity of the primary variables refer here to the single valued nature of the solution. Thus the assembly of elements is carried out by imposing continuity of primary variables at connecting nodes i.e.,  $u_n^e = u_1^{e+1}$  (the last nodal value of the element  $e$  is same as the first nodal value of the adjacent element  $e+1$ ). After imposing these conditions we get a discretized linear electro-elastic equilibrium equation



for the entire smart piezo actuator which is given as

$$[K] \{a\} = \{F\}$$

where  $[K]$  is the global stiffness matrix,  $\{a\}$  is vector of global degrees of freedom, and  $\{F\}$  is the global load vector.

A finite element code is written to carry out the formulation and the required results are generated for sensing and actuation cases.

## 4.1 Results and Discussion

### 4.1.1 Sensing mode

The results generated from finite element formulation show that in *sensing* case the tip deflection and potential induced can be expressed by the linear relations as

$$u_{tip} = a_1 F_{PS} \quad (4.6)$$

and

$$\Phi_{induced} = b_1 F_{PS} \quad (4.7)$$

where  $a_1$  and  $b_1$  are constants. The external mechanical load  $F_{PS}$  is taken to be positive when tensile and negative when it is compressive. Since both  $u_{tip}$  and  $\Phi$  are linear functions of the *sensing force*, the constants  $a_1$  and  $b_1$  are found out by applying a unit force at the ends of the bar i.e.,  $F_{PS} = 1N$ . For a given set of data (Table 4.1 and 4.2) the values of  $a_1$  and  $b_1$  are found to be

$a_1 = 4.08286 \times 10^{-7}$  and  $b_1 = 31.582$  (when Aluminium is chosen as the metallic layer).

### 4.1.2 Actuation mode

In actuation mode, the actuator is acted upon by external mechanical load  $F_{PA}$  ( $F_{PA}$  is taken to be positive when tensile and negative when it is compressive) and an external potential as shown in Fig. 4.1b. The tip deflection of the actuator can be expressed as

$$u_{tip} = c_1 F_{PA} + c_2 V_{PA} \quad (4.8)$$

where  $c_1$  and  $c_2$  are constants. The constant  $c_1$  is obtained by applying a unit force and zero voltage ( $F_{PA} = 1N$  and  $V_{PA} = 0V$ ) and while obtaining the constant  $c_2$  it is assumed that  $F_{PA} = 0N$  and  $V_{PA} = 1V$ . For the given set of data (Table 4.1 and 4.2) the values of  $c_1$  and  $c_2$  are

$c_1 = 5.5 * 10^{-7}$  and  $c_2 = -4.488 * 10^{-9}$  (when Aluminium is chosen as the metallic layer)

In this case, piezoelectric ceramic actuators exhibit a decrease in their displacement for a given excitation voltage as they are loaded. This relationship can be seen in the above equation, for the case where  $F_{PA} \neq 0$ . As the load is increased, the displacement eventually reaches zero, for a given applied potential  $V_{PA}$ . This load, where the net tip deflection of the piezo stack actuator is zero, is termed as the *block force*.

The results obtained from the finite element analysis are plotted as shown in Figs. 4.4-4.10. The results can be summarised as follows:

1. Plots 4.4 a,b, and c show the variation in deflection and induced electric potential with change in sensing force applied at the ends of the bar. The deflection varies linearly along the span of the piezo stack sensor and potential induced varies linearly within the piezo layer.
2. In the case of actuation Plots 4.5 a, b, and c shows the variation of deflection along the bar for different applied potentials. Deflection (elongation) varies linearly within the piezo layer and remains constant within the metallic layer.
3. Plot 4.6 represents the linear relationship between the applied potential and required block force. It is observed that a potential of -200 V requires a block force of -1.62 N so as to get zero deflection at the tip.
4. Plot 4.7 gives the nodal deflection when a potential of -123 V and the corresponding block force of -1 N is applied. It is clearly seen that the piezo nodes (denoted by the upper points) experience elongation and the metallic nodes (denoted by all the lower points), experience compression. The net deflection at the tip is observed to be zero.

of the deflection in the piezo and metallic layers are found to be different. Figure 4.9 shows the variation of deflection along the bar when a voltage of -500 V is applied across the piezo patches. Deflection varies linearly within the piezo layer and remains constant in the metallic layer. Figure 4.10 shows the relation between the potential applied and the required block force.

## 4.2 Summary

A smart actuator/sensor consisting of alternate layers of metal and piezo material is modeled. A finite element formulation is undertaken to obtain a relation between deflection, potentials and external mechanical loading for both sensing and actuation cases.

Table 4.1: Material Properties for PZT-5H

GPa					
$c_{11}$	$c_{12}$	$c_{13}$	$c_{33}$	$c_{44}$	$c_{66}$
138.33	93.16	95.06	131.26	21.05	21.05

$C/m^2$		
$e_{31}$	$e_{33}$	$e_{15}$
-4.0329	16.5815	12.29

$F/m$	
$\epsilon_1$	$\epsilon_3$
$15293 \cdot 10^{-12}$	$15028 \cdot 10^{-12}$

Table 4.2: Data for modeling the actuator

Diameter of the bar = 1 mm
Length of the bar = 24.5 mm
Number of layers used = 25 (alternate MP..M)
Thickness of the metal layer = 0.5 mm
Thickness of the piezo layer = 1.5 mm
Young's modulus for metal layer
For steel $\tilde{E} = 208$ GPa
For Aluminium $\tilde{E} = 70$ GPa

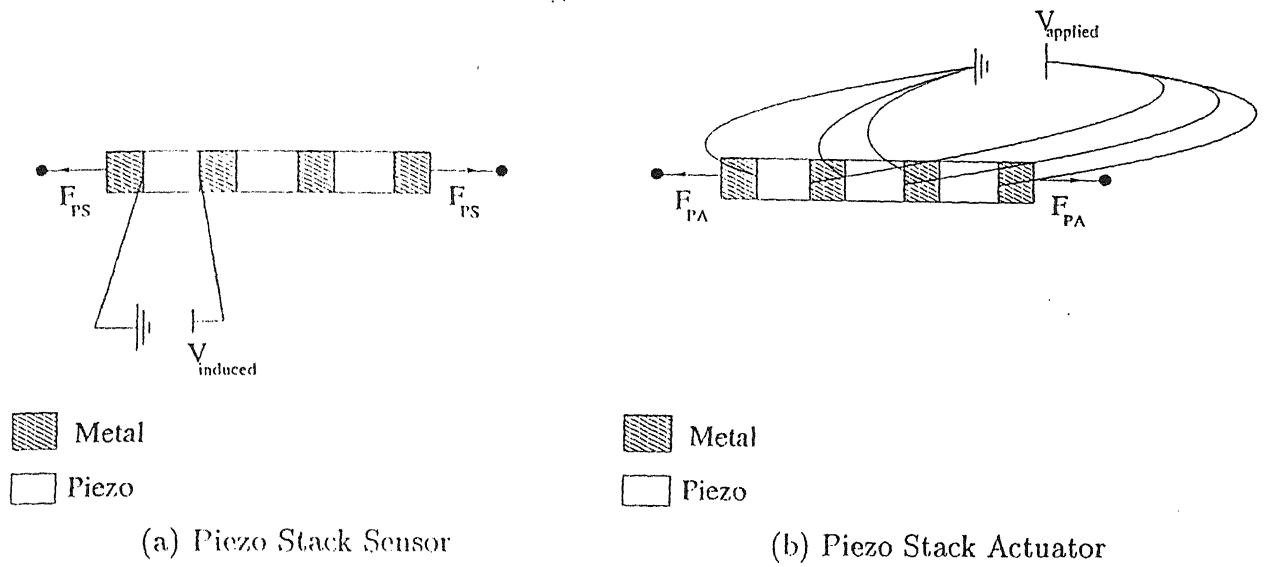


Figure 4.1: Piezo Stack Sensor and Actuator

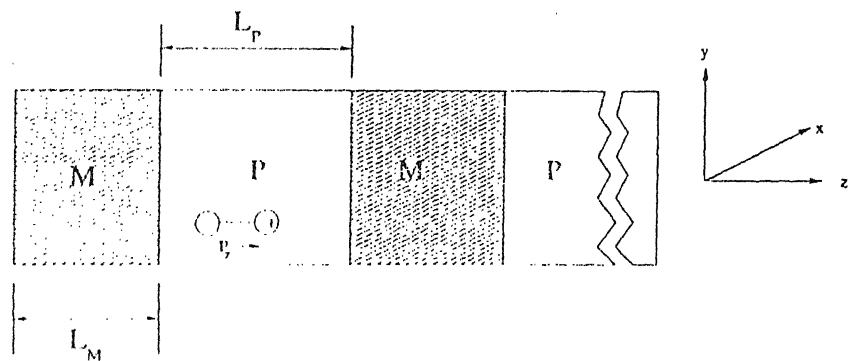


Figure 4.2: Bar model

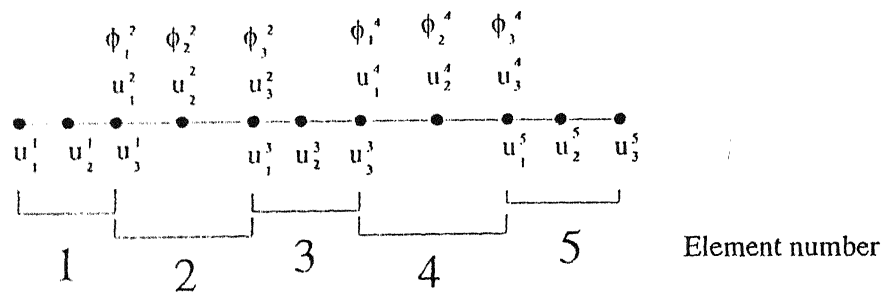
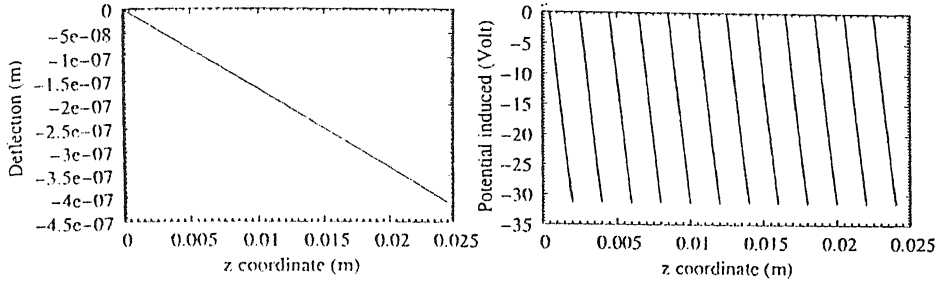
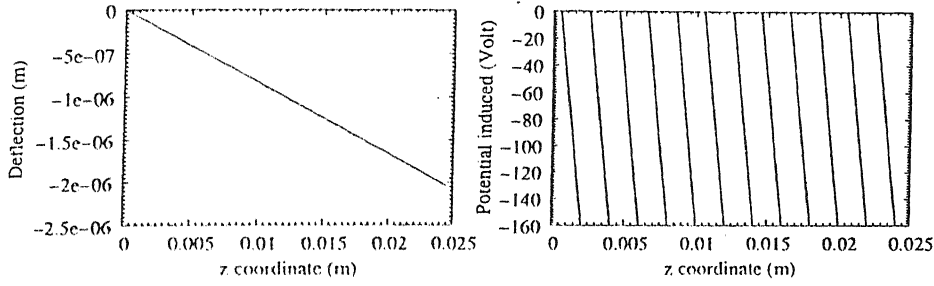


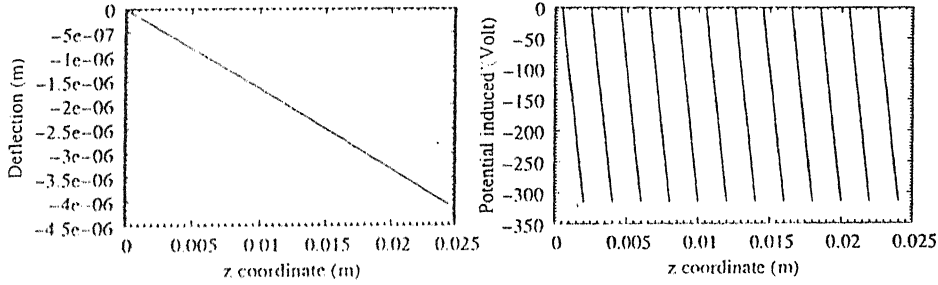
Figure 4.3: Finite element model of smart actuator



(a)  $F_{PS} = -1 \text{ N}$

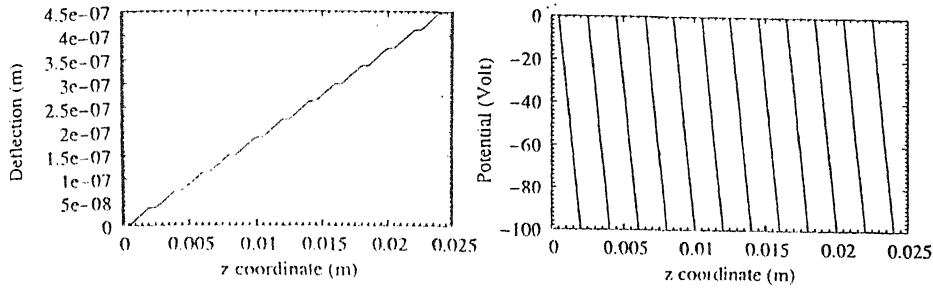


(b)  $F_{PS} = -5 \text{ N}$



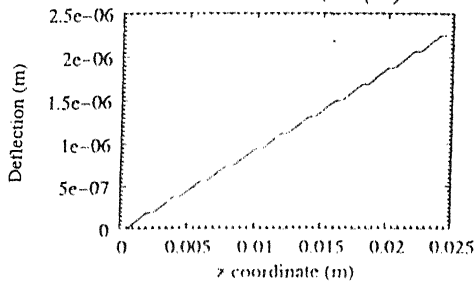
(c)  $F_{PS} = -10 \text{ N}$

Figure 4.4: Variation of deflection and induced potential for different external mechanical load (Sensing case metallic layer-aluminium)



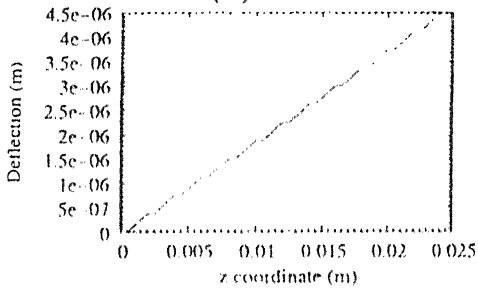
$\Lambda I$

(a)  $\Phi = -100 \text{ V}$



$\Lambda I$

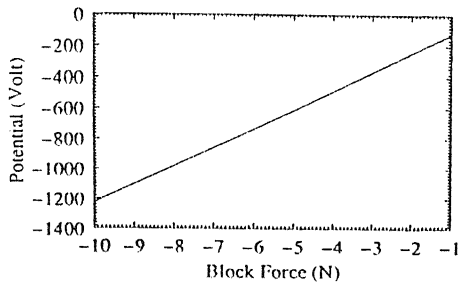
(b)  $\Phi = -500 \text{ V}$



$\Lambda I$

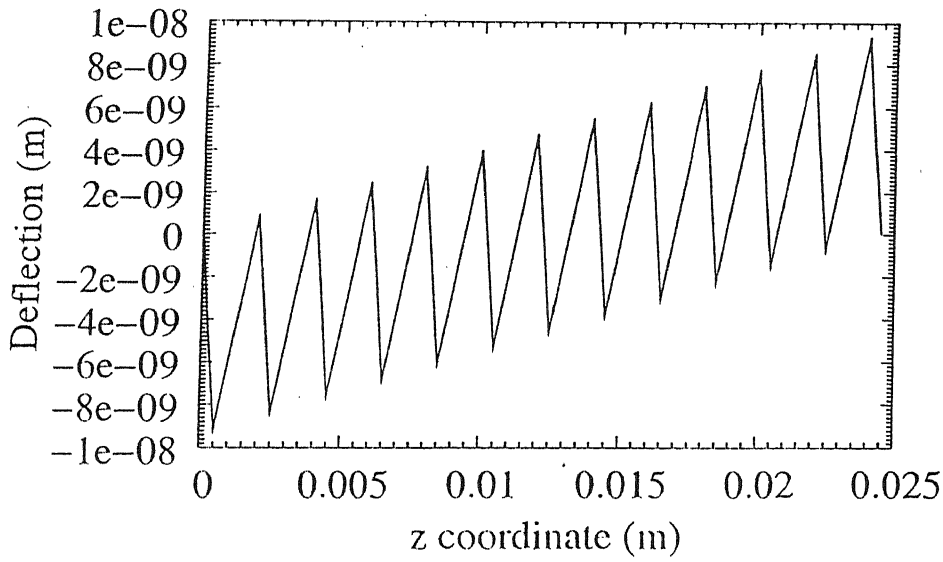
(c)  $\Phi = -1000 \text{ V}$

Figure 4.5: Variation of deflection along the span for different applied potentials (Actuator case)



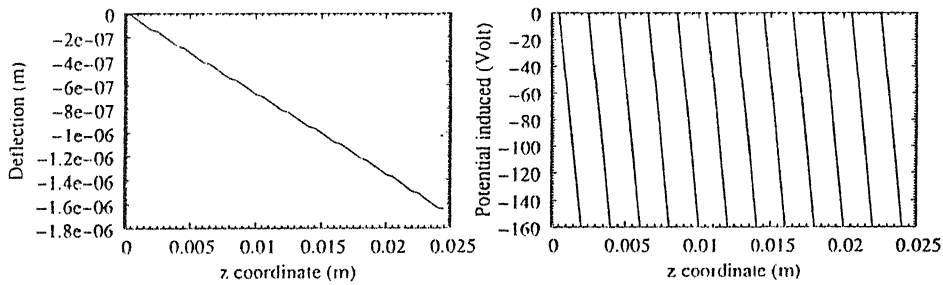
Al

Figure 4.6: Plot of potential Vs block force



Al

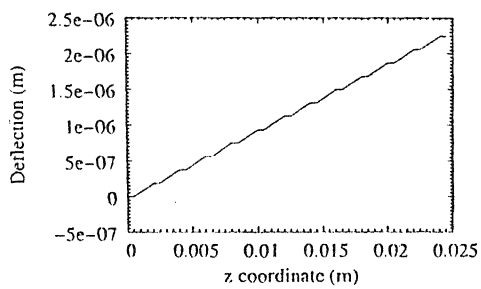
Figure 4.7: Plot of deflection along the bar when block force is applied



$$F_{PS} = -5 \text{ N}$$

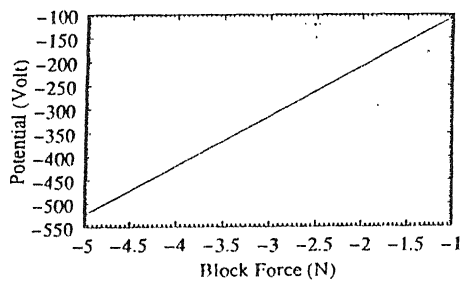
Figure 4.8: Sensing mode (metallic layer-steel)





$$\Phi = -500 \text{ V}$$

Figure 4.9: Plot for actuation case (metallic layer-steel)



Steel

Figure 4.10: Plot of potential Vs block force

## Chapter 5

# VIBRATION CONTROL IN HELICOPTERS USING ACTIVE VIBRATION CONTROL (CLOSED LOOP POSITION FEEDBACK)

The various sources of vibration in helicopters are the rotors, engine, and transmission system. Of these, the primary source of excitation is the main rotor system, which operates in a complex aerodynamic environment. The rotor blade loads are generated by an interaction of the physical quantities associated with the aerodynamic, inertial, and structural properties of the blade. These vibratory loads are transmitted to different parts of the fuselage through a complicated load path and cause discomfort to the pilot and crew, equipment deterioration, fatigue damage to the structure, and increased maintenance. The adverse effects of these vibratory loads increases with increase in forward speed of the helicopter and also the cumulative fatigue damage to the structure increases with higher utilization of the vehicle. As a result, these vibratory loads restrict the operation and efficiency of the vehicle. the demand for increasing helicopter usage for passenger transportation and the demand for high-speed maneuverability helicopters for defense have underlined the need for vibration reduction. Vibration reduction can be achieved in a number of ways. Vibration reduction schemes adopted in helicopters can be classified as either *passive or active control methodologies*. The passive control scheme includes hub or blade-mounted pendulum absorbers, anti resonant vibration isolation devices like dy-

dynamic anti resonant vibration isolator (DAVI), anti resonant isolation system (ARIS), and liquid inertia vibration eliminator (LIVE); structural modifications; and structural optimization. Active control methodologies include higher harmonic control (HHC), individual blade control (IBC), active flap control (AFC), and active control of structural response (ACSR). It may be noted that while HHC, IBC, and AFC control schemes are aimed at reducing the blade loads in the rotating frame, ACSR is employed in the non rotating frame to nullify the effect of vibratory hub loads on the fuselage.

Control engineering is based on the foundation of feedback theory and linear system analysis. Accordingly, control engineering is not limited to any engineering discipline but is applicable to Aeronautical, Chemical, Mechanical, Environmental, Civil and Electrical Engineering. A control system is an interconnection of components forming a system configuration that will provide a desired system response. The basis for analysis of a system is the foundation provided by linear system, which assumes a cause-effect relationship for the components of a system. A component or process to be controlled can be represented by a block as shown in Fig 5.1.

An open loop control system utilizes a controller or control actuator to obtain the desired response as shown in Fig 5.2. The open loop control system utilizes an actuating device to control the process directly without using sensors.

A closed loop control system (Fig 5.3) utilizes an additional measure of the actual output to compare it with the desired output response. The measure of the output is called the feedback signal. A feedback control system is a control system that tends to maintain a relationship of one system variable to another by comparing functions of these variables and using the difference as a means of control. As the system is becoming more complex, the interrelation of many controlled variables may be considered in the control scheme.

Here, in this study we formulate a closed-loop (position feedback) control scheme (Fig 5.4) for vibration minimization using the ACSR scheme. The concept of an ACSR scheme is based on the principle of superposition of two independent responses of a linear system, such that the total response is zero. In the case of helicopters, the fuselage is excited by the application of controlled external actuators at selected locations, such that the total response of the fuselage caused by the rotor loads and the external actuator forces is a minimum. The rotor loads are transmitted to the fuselage through the gearbox support structure. In this section, active vibration control of a highly idealised 2-D

system (Fig 5.5) of a helicopter is considered.  $M_F$  and  $M_H$  are the fuselage and hub masses respectively connected by a spring-damper-sensor-actuator system. The sensor and actuators are made of piezoelectric stack system, as shown in Figs. 5.6a and b.

The actuator is attached between the hub and the fuselage through a mechanism as in Fig. 5.7. The relation between the horizontal and vertical deflection, force at the actuator to force transmitted to hub and fuselage structure is derived as follows.

## 5.1 Formulation of relation between horizontal and vertical deflection

The gearbox support mechanism before and after deformation is shown in Fig. 5.7 we have

$$AO = \sqrt{\tilde{a}^2 - \frac{\tilde{b}^2}{4}} \quad (5.1)$$

From Fig. 5.7 it follows that

$$\bar{AO} = AO + \frac{(X_1 - X_2)}{2}$$

$$\bar{AO}^2 = \left(AO + \frac{(X_1 - X_2)}{2}\right)^2$$

$$\tilde{a}^2 - \left(\tilde{b} + \frac{u_{tip}}{2}\right)^2 = \left(\tilde{a}^2 - \frac{\tilde{b}^2}{4}\right) + \left(\frac{(X_1 - X_2)}{2}\right)^2 + AO(X_1 - X_2)$$

$$\Rightarrow \tilde{a}^2 - \frac{\tilde{b}^2}{4} - \frac{u_{tip}^2}{4} - \frac{\tilde{b}u_{tip}}{2} = \tilde{a}^2 - \frac{\tilde{b}^2}{4} + \frac{(X_1 - X_2)^2}{4} + AO(X_1 - X_2)$$

Neglecting higher powers of  $u$  and  $(X_1 - X_2)$  we get,

$$AO(X_1 - X_2) = -\frac{\tilde{b}u_{tip}}{2}$$

But from Eq. 5.1 it follows that,

$$u_{tip} = -\frac{\sqrt{4\tilde{a}^2 - \tilde{b}^2}}{\tilde{b}}(X_1 - X_2) \quad (5.2)$$

Where,  $u_{tip}$  corresponds to the axial tip deflection and  $(X_1 - X_2)$  to the vertical deflection (Fig. 5.7). Thus the above relation 5.2 helps transform the deflection from sensor/actuator to that transmitted to the hub and fuselage.

## 5.2 Formulation of relation between force at sensor/actuator and the force at hub/fuselage

Let the force at sensor be tensile. The deformation is considered to be very small such that the angle  $\Psi$  remains same for the deformed and undeformed configuration. Then, the following equations are written considering each of the truss members to be axial bars.

$$(F_{\overline{AB}} + F_{\overline{BC}}) \cos \Psi = F_{PS} \quad (5.3)$$

$$(F_{\overline{AB}} + F_{\overline{AD}}) \sin \Psi = F_S \quad (5.4)$$

where the subscripts (on LHS) denote the respective truss members and  $F_{PS}$  denotes the force at sensor, whereas the force  $F_S$  denotes the force transmitted to hub/fuselage.

Similarly,

$$(F_{\overline{AD}} + F_{\overline{CD}}) \cos \Psi = F_{PS} \quad (5.5)$$

$$(F_{\overline{CD}} + F_{\overline{BC}}) \sin \Psi = F_S \quad (5.6)$$

Considering Eqs. 5.3 and 5.5,

$$F_{\overline{AB}} + F_{\overline{BC}} = F_{\overline{AD}} + F_{\overline{CD}} \quad (5.7)$$

From Eqs. 5.4 and 5.6,

$$F_{\overline{AB}} + F_{\overline{AD}} = F_{\overline{CD}} + F_{\overline{BC}} \quad (5.8)$$

Adding up Eqs. 5.7 and 5.8 we obtain,

$$F_{\overline{AB}} = F_{\overline{CD}} = F_1, \text{ and similarly } F_{\overline{BC}} = F_{\overline{AD}} = F_2$$

Therefore,  $(F_1 + F_2) \cos \Psi = F_{PS}$  and  $(F_1 + F_2) \sin \Psi = F_S$

$$\text{i.e., } \tan \Psi = \frac{F_S}{F_{PS}}$$

$$F_S = F_{PS} \tan \Psi \quad (5.9)$$

where from geometry  $\tan \Psi$  is given as

$$\tan \Psi = \frac{\sqrt{4\tilde{a}^2 - \tilde{b}^2}}{\tilde{b}}$$

The same formulation is carried out for actuation case, wherein  $F_{PS}$  is substituted as  $F_{PA}$  and  $F_S$  is substituted as  $F_A$ .

## 5.3 Analysis of Vibration Problem

This study has been carried out in two sections, one in which only a sensor is provided between hub and fuselage and the other includes both sensor and actuator. The former study enables us to find out the frequency response of the system. This frequency is then used as the excitation frequency in the formulation of latter part of the study wherein the actual vibration reduction problem using closed loop active vibration control scheme is solved.

### 5.3.1 Sensing Mode

The relation between sensing force, deflection, and potential induced (Fig. 5.6a) is given as (See Chap. 4)

$$u_{tip} = a_1 F_{PS} \quad (5.10)$$

$$\text{i.e., } F_{PS} = \tilde{a}_1 u_{tip} \quad (5.11)$$

and

$$\Phi_{induced} = b_1 F_{PS} \quad (5.12)$$

using Eqs. 5.2, 5.9, and 5.11 we get a relation between  $F_S$  and  $(X_1 - X_2)$  in the form of

$$F_S = -F^*(X_1 - X_2) \quad (5.13)$$

For given data as in Table 5.1  $a_1 = 4.18031 * 10^{-7}$ ,  $\bar{a}_1 = \frac{1}{a_1} = 2.392 * 10^6$ ,  $b_1 = 7.8955$ , and  $F^* = 8.44 * 10^5$

### ***Formulation of equations of motion***

The equation of motion of the system in Fig. 5.5 can be written as

$$M_H \ddot{X}_1 + C(\dot{X}_1 - \dot{X}_2) + K(X_1 - X_2) = F_S + F_0 e^{i\omega t}$$

Substituting for  $F_S$ , from Eq. 5.13

$$M_H \ddot{X}_1 + C(\dot{X}_1 - \dot{X}_2) + K(X_1 - X_2) + F^*(X_1 - X_2) = F_0 e^{i\omega t}$$

This equation corresponds to hub/gear box motion.

The equation corresponding to the fuselage motion can be written as,

$$M_F \ddot{X}_2 + C(\dot{X}_2 - \dot{X}_1) + K(X_2 - X_1) + F^*(X_2 - X_1) = 0$$

Assuming a solution of the form  $X_1 = \bar{X}_1 e^{i\omega t}$  and  $X_2 = \bar{X}_2 e^{i\omega t}$ . Then we have

$$\frac{\bar{X}_1}{F_0/K} = \frac{1 + \frac{F^*}{K} - (\frac{\omega}{\omega_{ref}})^2 + i \frac{2\xi\omega}{\omega_{ref}}}{\mu(\frac{\omega}{\omega_{ref}})^4 - (1 + \frac{F^*}{K})(1 + \mu)(\frac{\omega}{\omega_{ref}})^2 - i2\xi(\frac{\omega}{\omega_{ref}})^3(1 + \mu)} \quad (5.14)$$

and

$$\frac{\bar{X}_2}{F_0/K} = \frac{1 + \frac{F^*}{K} + i \frac{2\xi\omega}{\omega_{ref}}}{\mu(\frac{\omega}{\omega_{ref}})^4 - (1 + \frac{F^*}{K})(1 + \mu)(\frac{\omega}{\omega_{ref}})^2 - i2\xi(\frac{\omega}{\omega_{ref}})^3(1 + \mu)} \quad (5.15)$$

where,

$$\mu = \frac{M_H}{M_F} = \text{Mass Ratio}$$

$$\omega_{ref}^2 = \frac{K}{M_F} = \text{Reference Frequency}$$

$C_{ref} = 2M_F\omega_{ref}$  = Critical Damping Coefficient

$\xi = \frac{C}{C_{ref}}$  = Damping Ratio

The magnitudes of Eqs. 5.14 and 5.15 are plotted against the frequency ratio and the resonance/natural frequency can be identified from frequency response.

### 5.3.2 Actuation mode

Figure 5.6b represents an actuator. It is acted upon, by an external mechanical loading and voltage. The relation between the actuation force, applied voltage and deflection is given by equation (See Chap. 4),

$$u_{tip} = c_1 F_{PA} + c_2 V_{PA}$$

$$F_{PA} = \bar{c}_1 u_{tip} + \bar{c}_2 V_{PA} \quad (5.16)$$

$$V_{PA} = G\Phi_{induced} \quad (5.17)$$

where  $G$  is the gain,  $\bar{c}_1$  and  $\bar{c}_2$  are constants.

The gain is given as

$$G = \bar{G}e^{in}$$

Using Eqs. 5.2, 5.10, 5.12, 5.16, and 5.17 we get a relation between  $F_A$  and  $(X_1 - X_2)$  in the form of

$$F_A = -\bar{F}(X_1 - X_2) \quad (5.18)$$

and when both sensor and actuator are included as two units in the system (Fig. 5.5) i.e., incorporating eq. 5.13

$$F = -\tilde{F}(X_1 - X_2)$$



where  $\tilde{F}$  is a linear function of gain and is given as

$$\tilde{F} = d_1 + d_2 G$$

where  $d_1 = \bar{F} + F^*$

For given data as in Table 5.1 ,  $c_1 = 5.65686 * 10^{-7}$ ,  $c_2 = -1.87 * 10^{-8}$ ,  $\bar{F} = 6.238 * 10^5$ ,  $d_2 = 2.2 * 10^5 G$  and hence  $\tilde{F} = 14.678 * 10^5 + 2.2 * 10^5 G$ .

### *Formulation of equations of motion*

The equations of motion are given as

$$M_H \ddot{X}_1 + C(\dot{X}_1 - \dot{X}_2) + K(X_1 - X_2) = F_A + F_S + F_0 e^{i\omega t}$$

This corresponds to equation for hub/gear box, which can be written as

$$M_H \ddot{X}_1 + C(\dot{X}_1 - \dot{X}_2) + K(X_1 - X_2) + \tilde{F}(X_1 - X_2) = F_0 e^{i\omega t}$$

and the equation corresponding to the fuselage

$$M_F \ddot{X}_2 + C(\dot{X}_2 - \dot{X}_1) + K(X_2 - X_1) + \tilde{F}(X_2 - X_1) = 0$$

Let  $X_1 = \bar{X}_1 e^{i\omega t}$  and  $X_2 = \bar{X}_2 e^{i\omega t}$ . Then we have

$$\frac{\bar{X}_1}{F_0/K} = \frac{1 + \frac{\tilde{F}}{K} - (\frac{\omega}{\omega_{ref}})^2 + i \frac{2\xi\omega}{\omega_{ref}}}{\mu(\frac{\omega}{\omega_{ref}})^4 - (1 + \frac{\tilde{F}}{K})(1 + \mu)(\frac{\omega}{\omega_{ref}})^2 - i2\xi(\frac{\omega}{\omega_{ref}})^3(1 + \mu)} \quad (5.19)$$

$$\frac{\bar{X}_2}{F_0/K} = \frac{1 + \frac{\tilde{F}}{K} + i \frac{2\xi\omega}{\omega_{ref}}}{\mu(\frac{\omega}{\omega_{ref}})^4 - (1 + \frac{\tilde{F}}{K})(1 + \mu)(\frac{\omega}{\omega_{ref}})^2 - i2\xi(\frac{\omega}{\omega_{ref}})^3(1 + \mu)} \quad (5.20)$$

The magnitudes of Eqs. 5.19 and 5.20 can be obtained for various values of gain  $\bar{G}$  and phase  $\eta$ .

The response of a passive control system (Ref. [22]) are given as follows:

$$\frac{R_H}{P_Z/K} = (\frac{\omega_{ref}}{\omega})^2 \left[ \frac{1 - (\frac{\omega}{\omega_{ref}})^2(1 + \mu_2(1 + L)^2) + i \frac{2\xi\omega}{\omega_{ref}}}{(\frac{\omega}{\omega_{ref}})^2(\mu_1 + \mu_2 L^2 + \mu_1 \mu_2(1 + L)^2) - (1 + \mu_1 + \mu_2) - i2\xi(\frac{\omega}{\omega_{ref}})(1 + \mu_1 + \mu_2)} \right]$$

$$\frac{R_F}{P_Z/K} = \left(\frac{\omega_{ref}}{\omega}\right)^2 \left[ \frac{1 - \left(\frac{\omega}{\omega_{ref}}\right)^2 (\mu_2 L (1 + L)) + i \frac{2\xi\omega}{\omega_{ref}}}{\left(\frac{\omega}{\omega_{ref}}\right)^2 (\mu_1 + \mu_2 L^2 + \mu_1 \mu_2 (1 + L)^2) - (1 + \mu_1 + \mu_2) - i 2\xi \left(\frac{\omega}{\omega_{ref}}\right) (1 + \mu_1 + \mu_2)} \right]$$

where,

$R_H, R_F$ - Hub and Fuselage motions (Fig. 5.8)

$P_Z$  -External force

$M_H, M_F, M_I$  - Hub, Fuselage and Isolator mass respectively

$$\mu_1 = \frac{M_H}{M_F}$$

$$\mu_2 = \frac{M_I}{M_F}$$

$$L = \frac{L_2}{L_1}$$

## 5.4 Results and Discussions

The frequency response of different systems is shown in Figs. 5.9. The Figs. 5.9 (a), (b), and (c) clearly depict the shift in the natural frequency of different systems (systems without sensor and actuator, effect of inclusion of sensor, and systems with both sensor and actuator). The reference frequency chosen was 6.78 Hz. It is observed that the natural frequency shifts from 19.5776 Hz (for a system without sensor and actuator), to 21.5466 Hz for a system with sensor only and then to 22.8935 Hz for a system with both sensor and actuator. Figures 5.10 (a) and (b) show the phase and potential induced as a function of the frequency ratio, when the system is in sensing mode. Figures 5.11 depict the response of the system (in actuation mode) with respect to gain for different phase angles (of gain). It is observed from Figs. 5.11 (a)-(e) that a better vibration reduction can be obtained with increase in phase (from 0 to 180). Figure 5.11 (f) shows the response of the system when the damping of the system is increased to 0.04% (from the original value of 0.004%). It is observed that minimum fuselage vibratory response is observed at a gain value of 24.8 and phase of 180 deg. Figure 5.12 (a)-(c) show the frequency response of the actuator at various values of gain. Figure 5.13 shows the response of the system (Ref. [22]; Fig. 5.8) as a function of mass ratio. It is observed that minimum fuselage vibratory response is obtained when mass of the isolator is taken to be 1.3 kg. Using this value of mass of isolator the plots 5.14 are drawn. Figure 5.14 depicts the response of the system given in Ref. [22] when isolator mass is fixed at a value of 1.3 kg. Figures 5.15

and 5.16 give the response of the sensor and actuator when steel is chosen as the metallic layer.

## 5.5 Summary

A closed-loop active vibration control problem using position feedback is solved in this chapter. The results that were obtained from chapter 4 are used while writing the equations of motion. Firstly the frequency response of the system is found out and then that utilized for solving the actual vibration problem. The results of this formulation were compared with the results given in Ref.[22] and in latter case it was shown that the inclusion of an isolator between the hub and the fuselage reduces the fuselage vibratory loads and increases the hub loads significantly, whereas our model simultaneously reduces both the fuselage and hub vibratory loads. This observation is of great importance in the industry.

Table 5.1: Data for vibration control

Diameter of the bar = 2 mm
Length of the bar = 100 mm
Number of layers of alternate MP...M = 101
Thickness of metal layer = 0.5 mm
Thickness of piezo layer = 1.5 mm
Young's modulus for steel = 208 GPa
Young's modulus for Al = 70 GPa
$M_b = 65$ kg
$R = 6$ m
$\Omega = 32$ rad/s
$K = M_b * \Omega^2$
$\omega_{ref} = \sqrt{\frac{K}{M_F}}$
$C_{ref} = 2 * M_F * \omega_{ref}$
$C = 0.033 * M_b * \Omega$
Mass of fuselage = 2200 kg
Mass of hub = 300 kg
$L = 12.5$

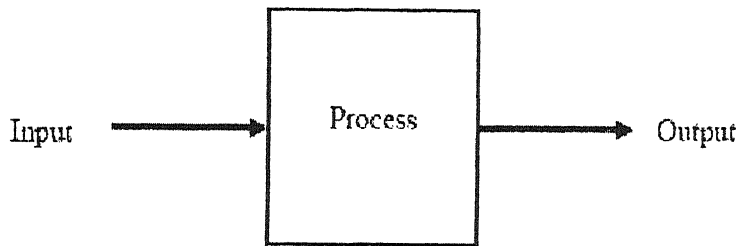


Figure 5.1: Process under Control

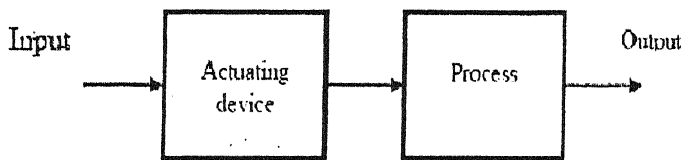


Figure 5.2: Open Loop Control System (No Feedback)

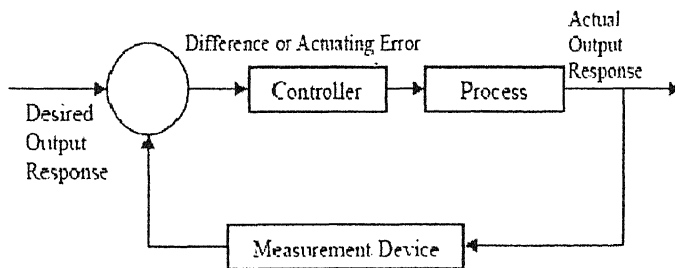


Figure 5.3: Closed-Loop Feedback System

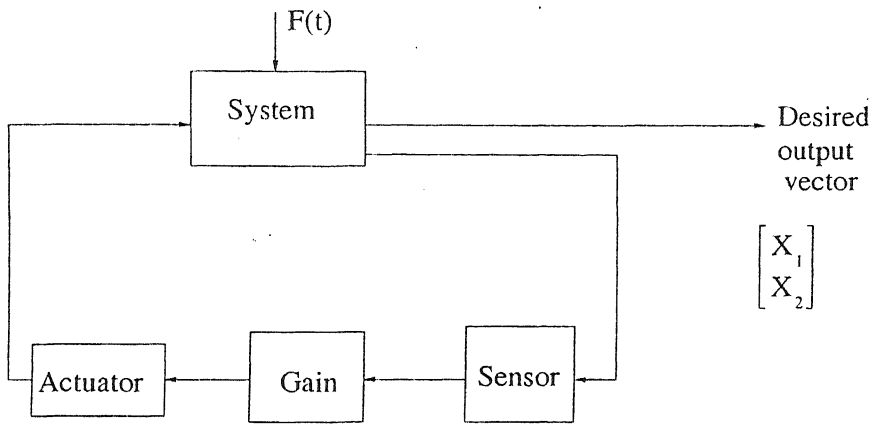
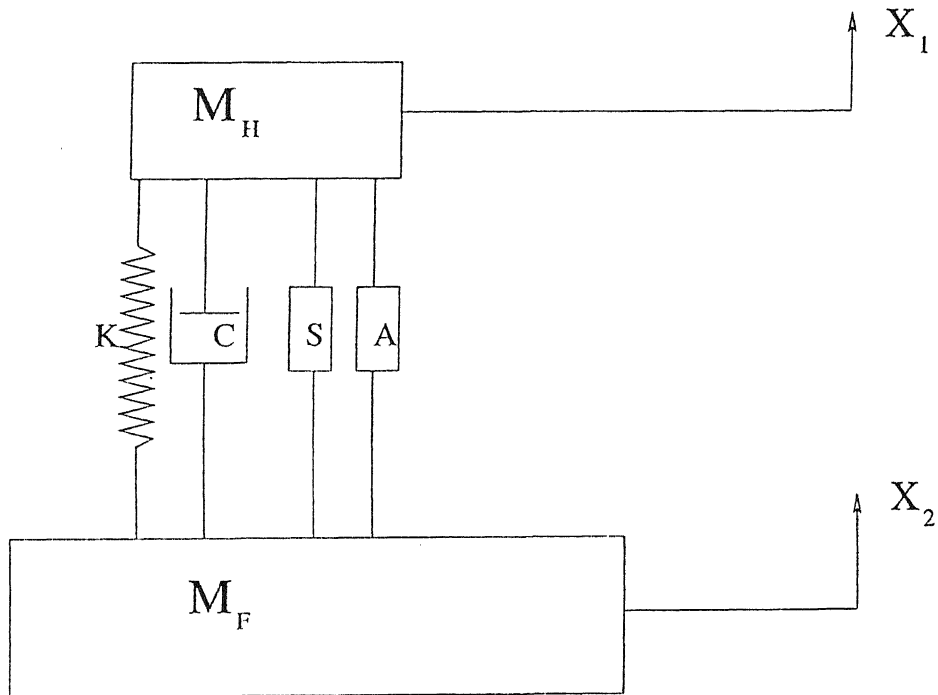


Figure 5.4: A Schematic Diagram of Position Feedback Control System



S – Sensor  
A – Actuator

Figure 5.5: Schematic of gear box support structure

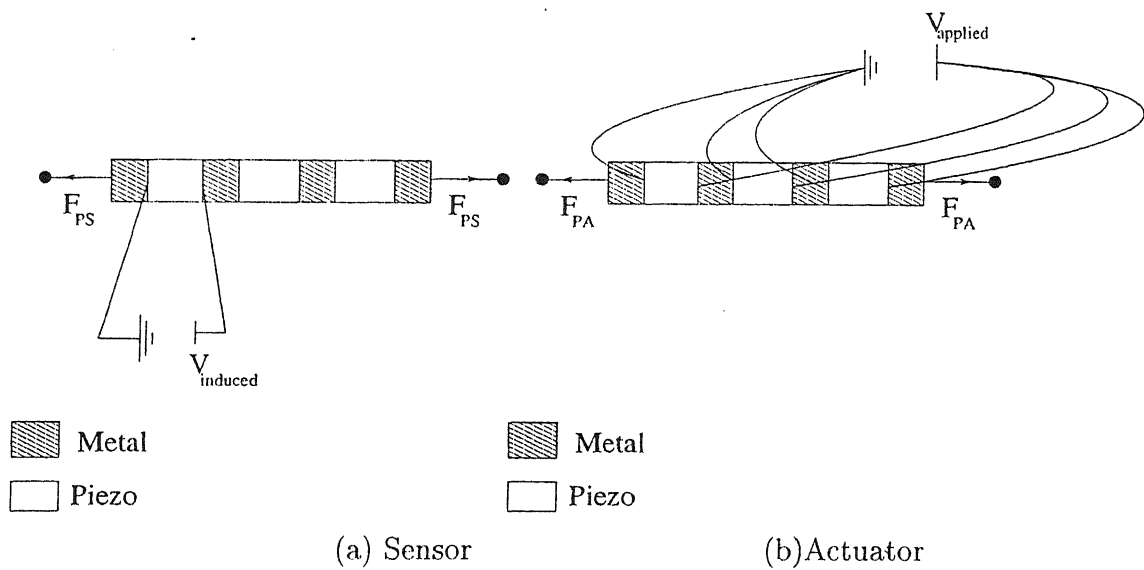


Figure 5.6: Piezo stack sensor and actuator

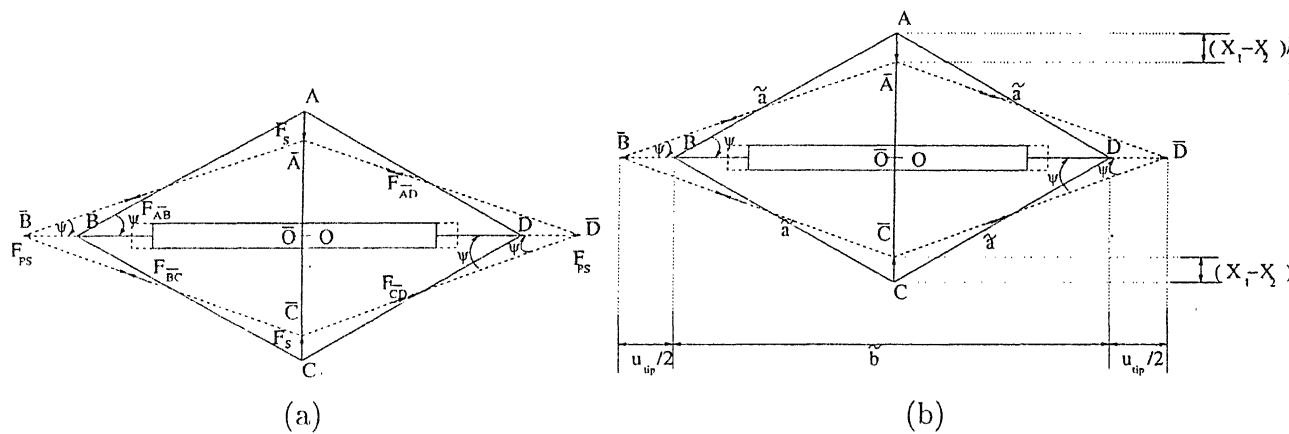


Figure 5.7: Actuator model before and after deformation

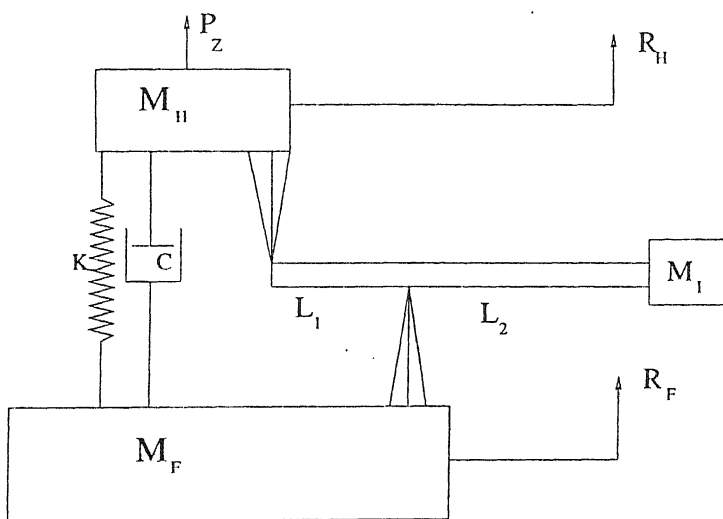
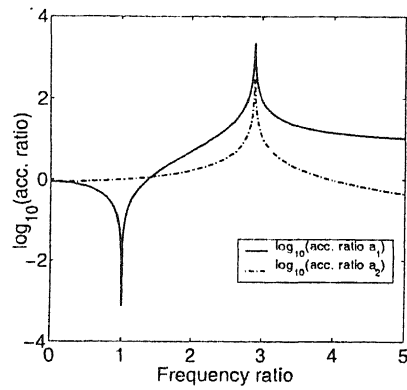
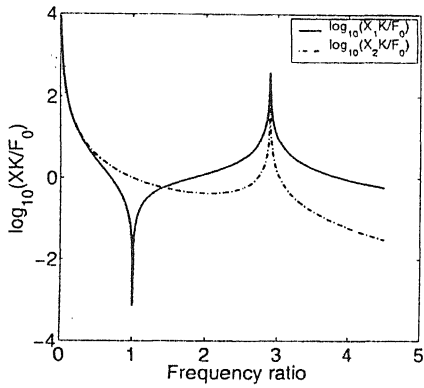
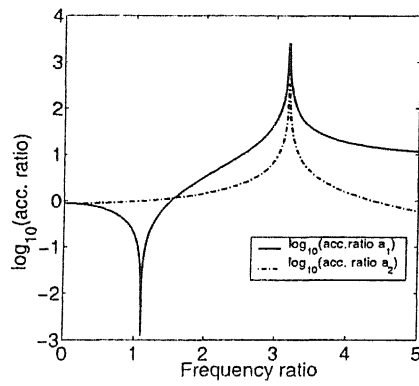
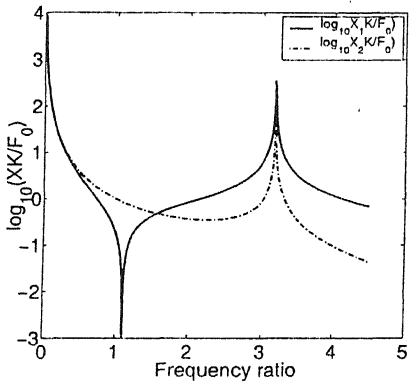


Figure 5.8: Rotor hub/isolator/fuselage dynamical model (Ref. [22])

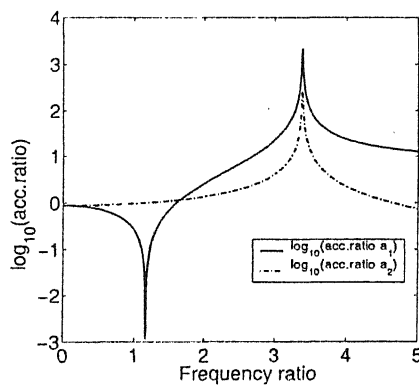
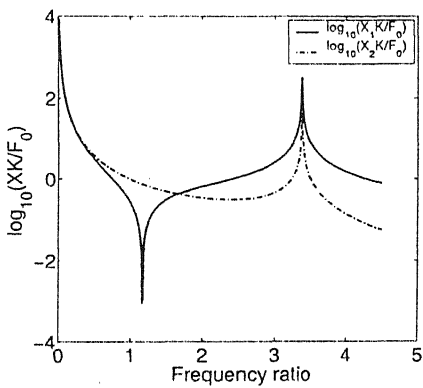




(a) without sensor and actuator

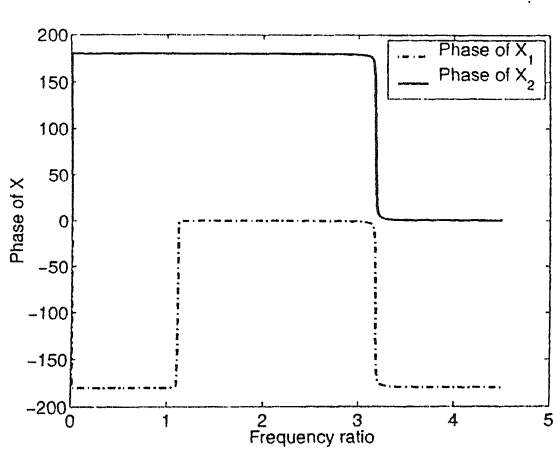


(b) with sensor only

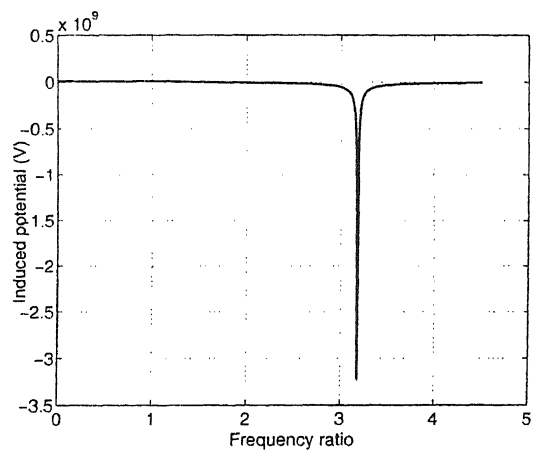


(c) with both sensor & actuator

Figure 5.9: Variation of displacement and acceleration of different systs with frequency (metallic layer-Aluminium)



(a)



(b)

Figure 5.10: Variation of phase and potential induced with frequency (sensing mode; metallic layer- Aluminium)

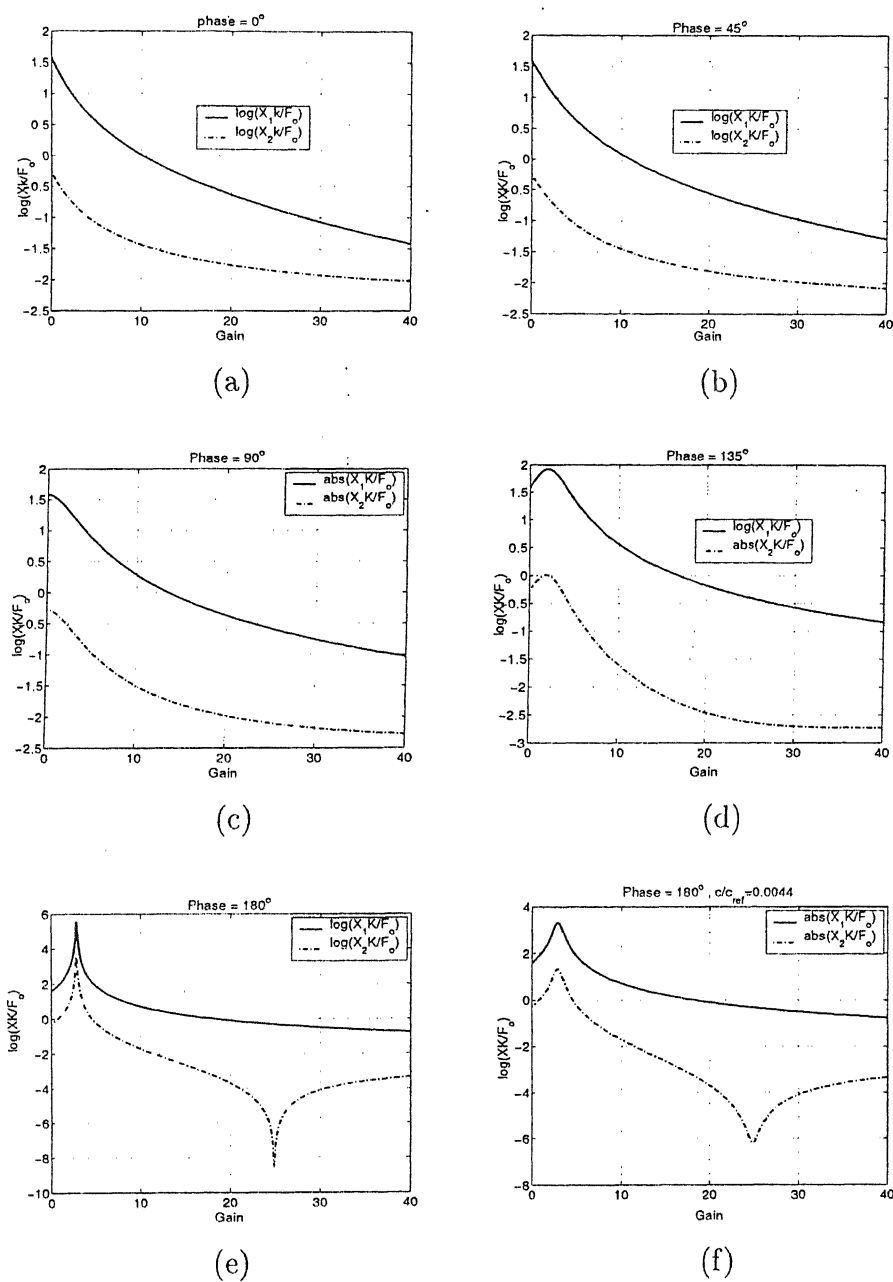
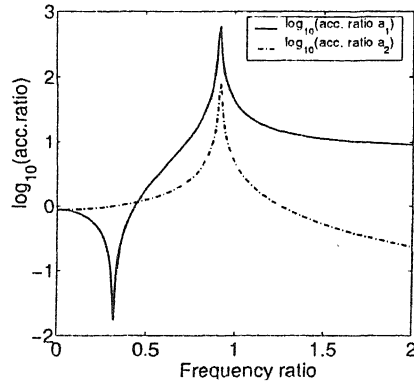
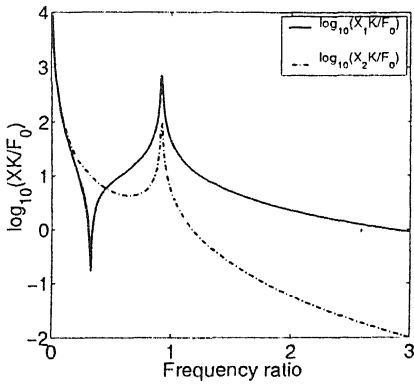
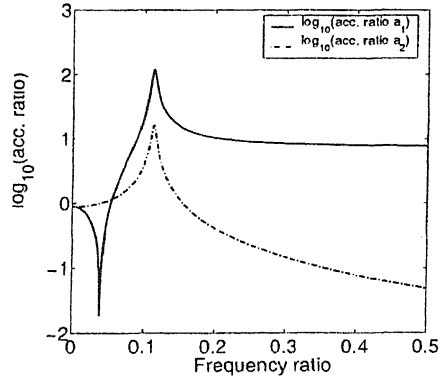
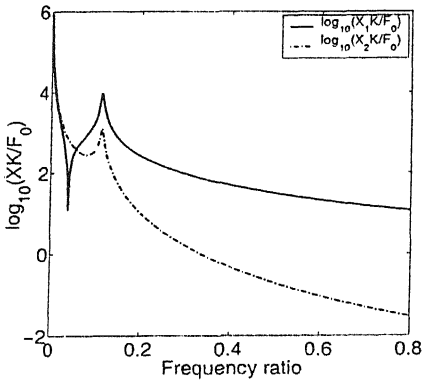


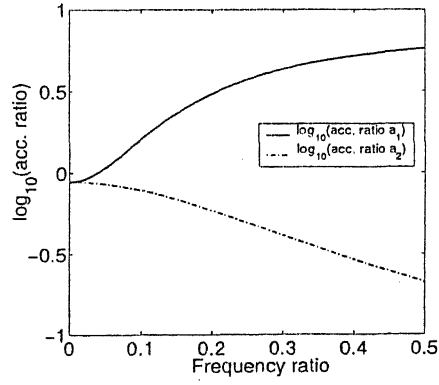
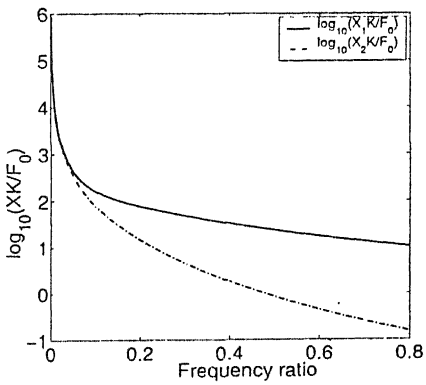
Figure 5.11: Variation of displacement with gain (actuation mode; metallic layer-Aluminium)



(a) Gain = -23 (i.e.,  $\eta=180^\circ$ )



(b) Gain = -24.8 (i.e.,  $\eta=180^\circ$ )



(c) Gain = -25 (i.e.,  $\eta=180^\circ$ )

Figure 5.12: Frequency response of the actuator at various values of gain (metalli layer-Aluminium)

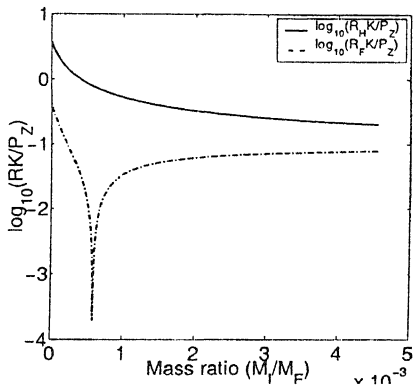


Figure 5.13: Response of the system (Ref. [22])

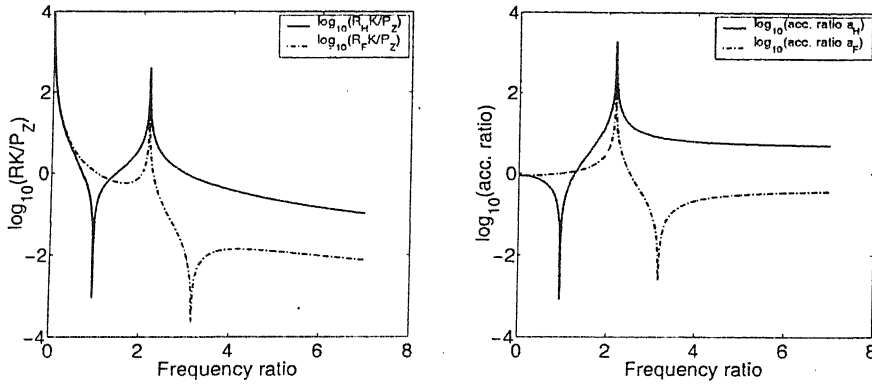


Figure 5.14: Response of the system (Fig. 5.8) when  $M_I = 1.3$  kg

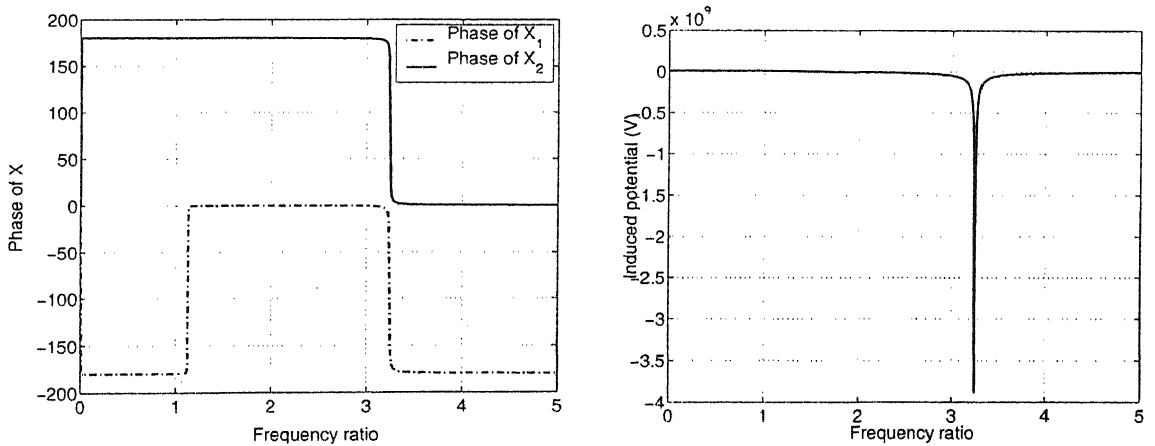
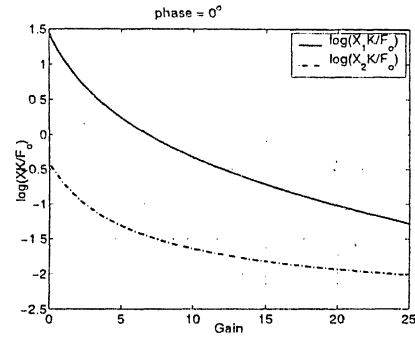
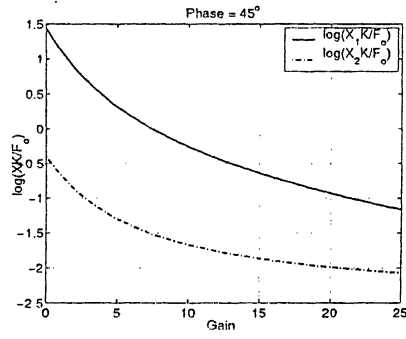


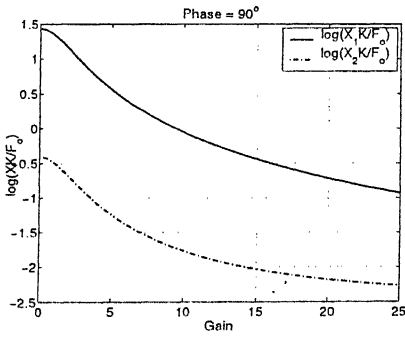
Figure 5.15: Variation of phase and potential induced with frequency (sensing mode; metallic layer-steel)



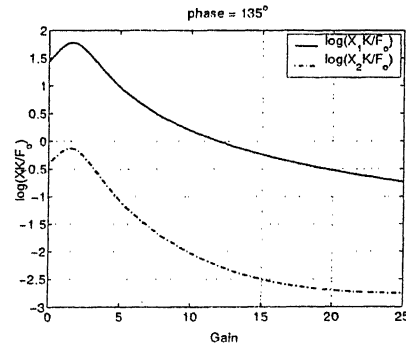
(a)



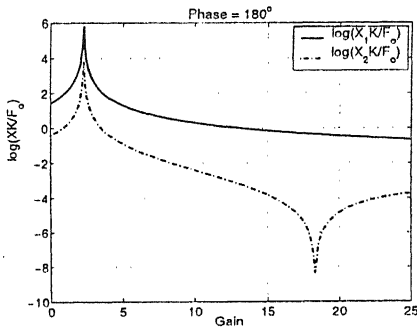
(b)



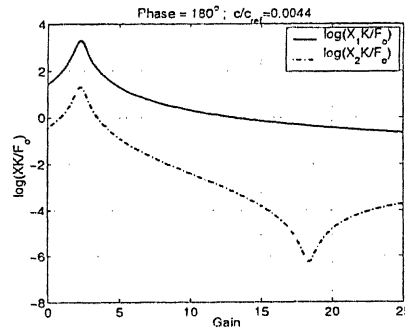
(c)



(d)



(e)



(f)

Figure 5.16: Variation of displacement with gain (actuation mode; metallic layer-steel)

## Chapter 6

# CONCLUDING REMARKS

There has been a lot of research being undertaken to study the behavior of smart actuators, their modeling and how they can be useful in real life applications. One such attempt is made in this thesis. We present electromechanical and thermal modeling of the piezo stack actuator. This includes modeling of hysteresis and butterfly loops, modeling of the actuator to obtain deflections and induced potentials, heat transfer analysis, and last but not the least is the analysis of the vibration problem. The important conclusions of this study are as follows:-

1. The domain switching model for hysteresis and butterfly loops is a much preferred model as compared to the complex stiffness model as it generates both the loops even at small values of electric field.
2. The inclusion of convection has a significant influence on the temperature profile of the piezo stack actuator. The temperature profile obtained in all cases is symmetric about the center of the bar.
3. A linear relation is obtained between tip deflection and applied force in sensing; tip deflection, applied force, and applied voltage in actuation . It was observed that there exists a linear relation between potential or voltage applied and the block force (force applied to negate the tip deflection obtained through applying voltage).
4. Using a piezo stack actuator as both sensor and actuator, a closed loop vibration control problem of a highly simplified 2-D model of a helicopter has been studied.

The results show that it is possible to reduce the vibratory response in both the hub and fuselage contrary to a passive vibration control system.



## Chapter 7

# SCOPE FOR FUTURE WORK

The present formulation can be considered as an initial step in the development of overall modeling of the smart actuators. It can lead a way to a more focused research in this area. A complete theoretical analysis has been presented over here. So as to validate this analysis an experimental setup can be established. Coming up to the vibration control part, this work can be extended to incorporate it in a real life helicopter vibration problem.

- [8] Sirohi, J., and Chopra, I., "*Fundamental behavior of piezoceramic sheet actuators*", Proceedings of SPIE Conference on Smart Structures and Integrated systems, California, USA, March, 1998.
- [9] Robert M. McMeeking, Chad M. L., "*A Phenomenological Multi-axial Constitutive Law for Switching in Polycrystalline Ferroelectric Ceramics*", International Journal of Engineering Science 40 (2002), 30 January 2002, pp. 1553-1577.
- [10] Gyan S. Jha, Venkatesan, C., and Upadhyay, C. S., "*Analytical Modeling of Hysteresis Effects in Piezoelectric Materials*", Technical Report Respond Project, VSSC, July 2000.
- [11] Bassiouny, E., Ghaleb, A. F., Maugin, G. A., "*Thermodynamical Formulation for Coupled Electromechanical Hysteresis Effects*", International Journal of Engineering Science, Vol. 26, No. 12, pp. 1279-1295, 1988.
- [12] Sues, R. H., Mau, T. S., and Wen, Y. K., "*Systems Identification of Degrading Hysteretic Restoring Forces*", ASCE, Vol 114, No. 5, 1998, pp. 833.
- [13] Fertis, D. G., "*Nonlinear Mechanics*", CRC Press, 1998, pp. 407-436.
- [14] Peter J. Chen and Stephen T. Montgomery, "*A Macroscopic Theory for the Existence of the Hysteresis and Butterfly Loops in Ferro-electricity*", Ferro-electrics, 1980, Vol. 23, pp. 199-208.
- [15] Zhang, X. D., and Rogers, C.A., "*A Macroscopic Phenomenological Formulation for Coupled Electromechanical Effects in Piezoelectricity*", Journal of Intelligent Material Systems and Structures, Vol. 4, July 1993.
- [16] Narayan, V., Lu, X., and Hanagud, S., "*A Domain Evolution Model for the Ferroelectric Hysteresis of Piezoceramic Materials*", 44th AIAA/ASME/ASCE/AHS Structures, Structural Dynamics, and Materials Conference, 7-10 April 2003, AIAA 2003-1439, Norfolk, Virginia, pp. 1-8.
- [17] Venkatesan, C., and Udayasankar, A., "*Selection of Sensor Locations for Active Vibration Control of Helicopter Fuselages*", Journal of Aircraft, Vol. 36, No. 2, March-April 1999, pp. 434-442.

- [18] Kubrusly, C. S., and Malebranche, H., " *Sensors and Controllers Location in Distributed Systems- A Survey*", Automatica, Vol. 21, No. 2, 1985, pp. 117-128.
- [19] Penny, J. E. T., Friswell, M. I., and Garvey, S. D., " *Automatic Choice of Measurement Locations for Dynamic Testing*", AIAA Journal, Vol. 32, No. 2, 1994, pp. 407-414.
- [20] Kammer, D. C., " *Sensor Placement for an On-Orbit Modal Identification and Correlation of Large Space Structures*", Journal of Guidance, Control, and Dynamics, Vol. 14, No. 2, 1991, pp. 251-259.
- [21] Lim, T. W., " *Actuator/Sensor Placement for Modal Parameter Identification of Flexible Structures*", Modal Analysis: The International Journal of Analytical and Experimental Modal Analysis, Vol. 8, No. 1, 1993, pp. 1-13.
- [22] Sivaramakrishnan, R., and Venkatesan, C., " *Rotor/ Fuselage Vibration Isolation Studies by a Floquet-Harmonic Iteration Technique*", Journal of Aircraft, Vol. 27, No. 1, January 1990, pp. 81-89.
- [23] Anita Mathews, Sule, V. R., and Venkatesan, C., " *Order Reduction and Closed-Loop Vibration Control in Helicopter Fuselages*", Journal of Guidance, Control, and Dynamics, Vol. 25, No. 2, March-April 2002, pp. 316-323.
- [24] Reddy, J. N., " *An Introduction to the Finite Element Methods*", Tata Mc. Graw Hill Publishing Company Limited.
- [25] Holman, J. P., 7th ed, " *Heat Transfer*", 1992.
- [26] Sachdeva, R. C., " *Fundamentals of Engineering Heat and Mass Transfer* ", New Age International limited, Publishers, 1995.
- [27] Vijay Gupta, " *Elements of Heat and Mass Transfer*", New Age International limited, Publishers, 1995.
- [28] Thomson, W. T., 4th ed, " *Theory of Vibrations with Applications*", Prentice-Hall of India, 1993.
- [29] Meirovitch, L., 2nd ed, " *Elements of Vibration Analysis*", McGraw-Hill Kogakusha, 1986.

A 148452

**A** 148452  
Date Ship

This book is to be returned on the date last stamped.

[illegible]